

**ORDERING KINETICS, STEADY STATE AND PHASE  
TRANSITION IN ACTIVE PARTICLE SYSTEMS: ROLE OF  
NOISE AND BOUNDARY**

A THESIS SUBMITTED FOR THE DEGREE OF  
DOCTOR OF PHILOSOPHY (SCIENCE)  
IN PHYSICS (THEORETICAL)

by  
**SUDIPTA PATTANAYAK**

Department of Physics  
University of Calcutta

2019

Dedicated to

*Sancharan*

---

## ACKNOWLEDGEMENTS

---

Firstly, I would like to express my sincere gratitude to my supervisors Dr. Shradha Mishra and Dr. Manoranjan Kumar for the continuous support of my Ph.D. study and related research, and their patience, motivation, and immense knowledge. Initially, I was interested to pursue my Ph.D. in quantum systems. After my selection in S.N.B.N.C.B.S., I had an interesting conversation with madam about her area of research, statistical mechanics, more specifically active matter systems where I will get an opportunity to explore different striking features of the natural systems. After almost one and a half years of my Ph.D., I got an opportunity to work with my other supervisor Dr. Manoranjan Kumar. One thing always wonders me is the patience and dedication of Sir and Madam towards their work and it helps me to get motivated. Other than research, I also like both of them as a human being. The successful completion of my research work and thesis was possible due to their excellent guidance and encouragement and I would always remain grateful to them. I would also like to express my sincere thanks to our collaborator Prof. Sanjay Puri from Jawaharlal Nehru University, New Delhi. During the last six months of my Ph.D., I had many fruitful conversations with him, and his immense knowledge in Physics helped me to understand many things. We used to have Stat-physics journal club every week. There we had the opportunity to discuss and understand different topics in a very informal and friendly manner. The presence of Shradha Madam, Manoranjan Sir, Punyabrata Sir, Sakuntala Madam and Manna Sir made the discussions worthwhile. I acknowledge S.N.B.N.C.B.S. for providing me funding, a good research atmosphere, and such a beautiful and green campus. I would like to thank the Physics department of I.I.T. (BHU) Varanasi for their kind hospitality and support whenever I have visited there during my Ph.D. I would also like to thank Dr. M. Sanjay Kumar for his kind support during my Ph.D.

I would like to thank my group-mates Aslam da, Rakesh, Debasmita, Monalisa (senior), Sudip, Daya da, Koushik, Saniur, Jyotirmoy, Monalisa (junior), Sameer, Jay Prakash, Vivek,

Pranay for academic and non-academic discussions, and for all the fun that we had in the last five years. I feel fortunate to have Aslam Da and Rakesh as senior group members. I feel lucky to have Ananda as my cubical mate, and I love to irritate him and vice versa. I also thank Sankar, Subhajit Da, Biplab Da, Arghya da, Poulami Di, Debasish, Lalu, Subrata da, Kartik da, Keshab, Rajkumar, Shauri, Sumanta, Tukun, Snehasish, Sourav and the entire SNB family for the quality time I have spent with them.

I must acknowledge my lifetime friends Shamik, Kamal, Suvayan, Pingal, Arnab, Swagnik. I always cherish my old memories with them, and wherever we go we will miss our M.Sc days. I would also like to thank Sanchari and Bijit.

Last but not the least, without the unconditional love and support of my Ma, Baba, and Bhai I could not have come so far. My thankfulness would fall short for them. I also want to acknowledge my in-laws and all my relatives. Finally, I want to express my heartiest love to Sumana (my friend, philosopher, guide, frustration absorber and life partner) and without her support everything will remain incomplete. I always remember her words when she first came to my life "I want to be your inspiration". Till now, my mother, father, and Sumana ask me whether I do my study regularly or I am wasting my time.

---

## PUBLICATIONS

---

### PAPERS TO BE INCLUDED IN THE PH.D. THESIS

- *Boundary induced convection in a collection of polar self-propelled particles,*  
Shradha Mishra and Sudipta Pattanayak,  
Physica A: Statistical Mechanics and its Applications **477**, 128 (2017).
- *Collection of polar self-propelled particles with a modified alignment interaction,*  
Sudipta Pattanayak and Shradha Mishra,  
Journal of Physics Communications **2**, 4 (2018).
- *Enhanced dynamics of active Brownian particles in periodic obstacle arrays and corrugated channels,*  
Sudipta Pattanayak, Rakesh Das, Manoranjan Kumar and Shradha Mishra,  
The European Physical Journal E **42**, 62 (2019).
- *Self-propelled particles with inhomogeneous quenched speed,*  
Sudipta Pattanayak, Rakesh Das, Manoranjan Kumar and Shradha Mishra (Manuscript under preparation)
- *A comparative study of ordering kinetics in active and passive model B,*  
Sudipta Pattanayak, Shradha Mishra and Sanjay Puri (Manuscript under preparation)

---

## CONTENTS

---

1	INTRODUCTION	1
1.1	Active matter systems: out-of-equilibrium	2
1.2	Categories of active matter systems	4
1.2.1	Dry and wet systems	4
1.2.2	Polar and apolar systems	5
1.3	Inhomogeneity and confinement	7
1.4	Methodology	9
1.4.1	Microscopic rule based study or agent based simulation	9
1.4.2	Phenomenology : hydrodynamic equations of motion	13
1.5	Coarsening	17
1.5.1	Coarsening in non-conserved systems (model A)	17
1.5.2	Coarsening in conserved systems (model B)	19
1.5.3	Correlation function and structure factor	20
1.5.4	Coarsening in active systems	21
1.6	objective and organisation of this thesis	22
2	BOUNDARY INDUCED CONVECTION IN A COLLECTION OF POLAR SELF-PROPELLED PARTICLES	24
2.1	Introduction	24
2.2	Model	25
2.2.1	Hydrodynamic equations of motion	26
2.3	Numerical Study	29
2.4	Results	31
2.4.1	Zero activity $R_A = 0$ or SPS $v_0 = 0.0$	31
2.4.2	Non-zero activity or SPS $v_0 \neq 0.0$	31

2.5	Discussion	35
3	ENHANCED DYNAMICS OF ACTIVE BROWNIAN PARTICLES IN PERIODIC OB- STACLE ARRAYS AND CORRUGATED CHANNELS	38
3.1	Introduction	38
3.2	Model	40
3.3	Results	42
3.3.1	Substrate with periodic array of obstacles	42
3.3.2	Corrugated channel	47
3.4	Discussion	49
4	COLLECTION OF POLAR SELF-PROPELLED PARTICLES WITH A MODIFIED ALIGN- MENT INTERACTION	51
4.1	Introduction	51
4.2	Model	52
4.3	Numerical Study	54
4.3.1	Disorder-to-order transition	55
4.3.2	Density phase separation	59
4.4	Hydrodynamic equations of motion	61
4.5	Linearised study of the broken symmetry state	63
4.6	Discussion	66
5	SELF-PROPELLED PARTICLES WITH INHOMOGENEOUS QUENCHED SPEED	68
5.1	Introduction	68
5.2	Model	69
5.3	Results	71
5.3.1	Long range ordering	71
5.3.2	Ordering to steady state	71
5.3.3	Steady state features	72
5.4	Discussion	76

6	A COMPARATIVE STUDY OF ORDERING KINETICS IN ACTIVE AND PASSIVE MODEL B	77
6.1	Introduction	77
6.2	Model	78
6.3	Results	80
6.3.1	Critical active model B	80
6.3.2	Off-critical model B	83
6.3.3	Effect of noise	85
6.4	Discussion	86
7	CONCLUSION	87

---

## LIST OF FIGURES

---

Figure 1.1 Schematic of the various types of active particles and their orientationally ordered states. Polar active particles (top left image), such as bacteria or birds, have a head and a tail and are generally self-propelled along their long axis. They can order in polar states (bottom left) or nematic states (bottom center). The polar state is also a moving state with a nonzero mean velocity. Apolar active particles (top right image) are head-tail symmetric and can order in nematic states (bottom right). 6

Figure 2.1 (left) Vector plot of local polarisation and (right) density inside the channel for activity  $R_A = 0.67$ . Different plots are snapshot of polarisation and density at different times. (left) local polarisation shows vortex type periodic pattern (*rolls*) along the long axis of the channel. Different color dots on periodic *rolls* represent distinct vortex. Density also shows periodic pattern. Bright regions are high density and dark regions are low density. Top to bottom figures are from small to large time. With time periodic *rolls* for both density and local polarisation moves from one end to other end of the channel. Arrow on the top of the figure represent direction of motion of periodic pattern. This direction is spontaneously chosen from two equally possible direction in the system. 25

Figure 2.2 Geometry of confined channel and orientation of particle at the two confined boundaries.  $x$ -direction is chosen along the long axis of the channel and  $z$ -direction is the confinement direction. Periodic boundary condition is used along the long axis of the channel. Orientation is parallel to  $+x$ -direction at bottom boundary ( $z=1$ ) and parallel to  $-x$ -direction at top boundary ( $z=d$ ). Magnitude of polarisation  $|P| = 1$  is fixed at two boundaries and density is maintained to mean value  $\rho_0 = 0.1$ . 26

Figure 2.3 For zero activity  $R_A = 0$  or SPS  $v_0 = 0.0$ : (a) vector plot of orientation field, which shown periodic vortex type pattern *rolls*. (b)  $x$ -component of polarisation  $P_x$  (c)  $z$ -component of polarisation  $P_z$  and (d) density  $\rho(x)$ : along the long axis of the channel, averaged over the  $z$ -direction. 27

Figure 2.4 Plot of percentage density fluctuation  $\% \Delta N$  vs. activity  $R_A$  for different width  $d$  of the channel.  $\Delta N$  shows non monotonic behaviour as we increase activity  $R_A$ . Density inhomogeneity increases as we increase width of the channel. 28

Figure 2.5 Plot of one dimensional density along the long axis of the channel for different self-propelled speeds (a) For small  $R_A = 0.13$ , density shows inhomogeneous structure but with time this inhomogeneous structure does not move much from its position. (b)-(c) For  $R_A = 0.53$  and  $1.13$ , pattern of high and low density move along the long axis of the channel. Patterns move with different speeds at different self-propelled speeds. (d) Again for large  $R_A = 1.87$ , pattern does not move much with time. Density inhomogeneity is small compared to that at intermediate  $R_A$ . Length of the arrow denotes the shift in the density pattern with time. 30

- Figure 2.6 Cartoon of periodic pattern of density for finite self-propelled speed  $v_0$  or activity  $R_A$ .  $r_{max}[i]$  shows the position of  $i^{th}$  maxima and  $r_{min}[i]$  the position of the  $i^{th}$  minima of density. The two arrows denote the direction of alignment at the two boundaries. We record the position of maxima and minima at different times. 33
- Figure 2.7 Plot of (a) mean square displacement (MSD)  $\Delta(t)$  and (b) corresponding diffusion coefficient  $D(t) = \Delta(t)/(2t)$  vs. time  $t$ , of position of high and low density peak position average over many realisation. Different curves are for different activity ranging from  $R_A = 0.0$ , large values  $R_A = 1.67$ . For small  $R_A \leq 0.13$ ,  $\Delta(t) \simeq t$  (a) and density shows diffusive behaviour hence  $D(t)$  approaches constant value (b) at large time. For intermediate  $0.67 \leq R_A < 1.33$ ,  $\Delta(t) \simeq t^2$  and travelling periodic pattern (a) and hence  $D(t) \simeq t$  (b), and for large  $R_A \geq 1.67$ , again diffusive and hence  $\Delta(t) \simeq t$  (a) and  $D(t)$  approaches constant value (b). Two Straight lines in (a) are line of slope 1 and 2. and in (b) straight line is of slope 1. 36
- Figure 3.1 (a) The schematic picture of a square lattice with obstacles at its vertices. Centre to centre distance between obstacles  $a = 1.0$ . The packing fraction of the lattice is varied from  $\Phi = 0.125$  (obstacle free substrate) to  $\Phi = 0.39$ . (b) The schematic picture of a quasi-one-dimensional corrugated channel comprised periodically arrayed circular / elliptical obstacles. The periodicity  $a$ , and width of the channel  $d$  are shown.  $r_{eff}$  (defined in the text) is shown. The  $\Phi$  of the channel is varied from  $\Phi = 0.10$  to  $0.60$  by changing  $d$  or  $a$ . Boxes show unit cell for both cases.  $x$  and  $y$  directions for both model are shown. 41

Figure 3.2 Plot of ballistic trajectory of four ABPs at the beginning and when they follow the obstacle boundary are shown in (a) and (b) respectively. Initial coordinate for all ABPs is  $(49.5, 49.5)$ , and their directions are different. Four different colors used for four ABPs. The intersection points of the dotted lines in (b) represent centre of an obstacle. The boxes in (a) represent the end point of the trajectories, and boxes in (b) represent the starting of the trajectories.  $\Phi = 0.39$ . Plot of late time diffusive trajectory of an ABP on the two dimensional periodic obstacle substrate of  $\Phi = 0.39$ , and  $\Phi = 0.125$  (free substrate) are shown in (c) and (d) respectively. The time interval is same (100) in (c) and (d). We consider  $Pe = 50$ . 43

Figure 3.3 Plot of the mean square displacement of the ABP  $\langle \Delta r^2 \rangle$  vs. time  $t$  in the periodic square lattice of  $\Phi = 0.39$  (a) and  $\Phi = 0.125$  (obstacle free substrate)(b). Region I and III are ballistic and diffusive regions of the ABP respectively. Line of slope 2 (magenta) and 1 (indigo) are shown. The approximate cross-over point from super-diffusive to diffusive dynamics for different  $Pe$  for both cases are shown by an blue arrow. In inset of (a),  $\langle \Delta r^2 \rangle$  with time  $t$  for different  $Pe$  in region II (when ABP moves along obstacle boundary) is shown. 44

Figure 3.4 Plot of scaled mean square displacement  $\langle \Delta r^2 \rangle / 4D_{eff}t_c$  vs. scaled time  $t/t_c$  of the ABP in the square lattice of  $\Phi = 0.39$  (a) and  $\Phi = 0.125$  (obstacle free substrate) (b) are shown. (c) The cross-over time  $t_c$  with  $Pe$  for  $\Phi = 0.39$  and  $\Phi = 0.125$ (obstacle free substrate) are shown by red squares and black circles respectively. 45

Figure 3.5 (a) Variation of the  $\langle \Delta r^2 \rangle / 4t$  with time  $t$  for  $Pe = 50$  is shown. The black and green line is for  $\Phi = 0.125$ (obstacle free substrate) and  $\Phi = 0.39$ , respectively. (b) Plot of the effective translational diffusion constant  $D_{eff}$  of the ABP for different  $Pe$ . The black circles and red squares and blue triangles are for the periodic  $\Phi = 0.125$  (obstacle free substrate),  $\Phi = 0.25$  and  $\Phi = 0.39$  respectively. Linear slope for  $\Phi = 0.125, 0.25$  and  $0.39$  are  $0.0018, 0.0011, 0.0009$ , respectively. Plot of  $P(\Theta)$  of the ABP for  $\Phi = 0.39$  and  $\Phi = 0.125$  (obstacle free substrate) are shown in (c) and (d) respectively. For (c) and (d) we consider  $Pe = 50$ . 46

Figure 3.6 Plot of the mean square displacement  $\langle \Delta r^2 \rangle$ , the exponent  $\beta$  at early and late time of the ABP in the corrugated channel for different  $\Phi$  are shown in (a-c), respectively. We consider  $Pe = 100$  and  $\Phi$  changes as we vary channel width  $d$ .  $\langle \Delta r^2 \rangle$ , the exponent  $\beta$  at early and late time of the ABP in a flat repulsive channel of width  $d = 0.42$  are shown in (d-f), respectively. For flat channel the radius of the ABP  $r_p = 0.2$ , and  $Pe = 50$ . 48

Figure 3.7 (a) Plot of the transport speed  $V_T$  of the ABP in the corrugated channel with packing fraction  $\Phi$ . We varied  $\Phi$  from  $0.10$  to  $0.60$ . For circles, we change channel width  $d$  to vary  $\Phi$ , and for squares,  $\Phi$  is changed by varying periodicity  $a$  of the obstacles along the boundary of the channel. (b) Plot of  $V_T$  of the ABP in the corrugated channel comprised periodically arrayed elliptical obstacles vs.  $b'$ . We fixed the  $\Phi = 0.52$  and  $a' = 0.29$ . For (a) and (b)  $Pe = 100$ . Error bar of  $V_T$  is shown for all cases. 48

Figure 4.1 Plot of the global velocity  $V$  vs. the noise strength  $\eta$  for four different distance dependent parameters  $a$ . Fig. (a-d) are for  $a = 1.0, 0.5, 0.4, 0.01$  respectively. In Fig. (d), the variation of  $V$  is clearly continuous for all system sizes, and there is no crossover. The variation of  $V$  changes as we increase  $a$ , and there is a crossover for  $a = 1.0$ . Plot of the  $V$  for four different system sizes ( $N = 1000, 2000, 5000, 10000$ ) are shown by black  $\bullet$ , red  $\blacklozenge$ , green  $\blacktriangle$  and blue  $\blacksquare$  respectively. 53

Figure 4.2 *Upper panel* : Plot of the time series of the global velocity  $V$  for four different  $a = (0.01, 0.4, 0.5, 1.0)$ , from top to bottom. The time series of the  $V$  are plotted for three different noise strengths  $\eta_1(a)$ (black)  $< \eta_2(a)$ (red)  $< \eta_3(a)$ (blue) close to the critical noise strength  $\eta_c$  for each  $a$ . For  $a = 0.01$  the time-series of the  $V(t)$  is shown for  $\eta_1 = 0.099$ (black),  $\eta_2 = 0.100$ (red) and  $\eta_3 = 0.101$ (blue). Similarly  $\eta_1 < \eta_2 < \eta_3$  for  $a = 0.4, 0.5$  and  $1.0$  are  $(0.358, 0.359, 0.360)$ ,  $(0.409, 0.410, 0.411)$  and  $(0.627, 0.628, 0.629)$  respectively. There is a clear switching behavior in the global velocity variation for  $a = 1.0$ , and it vanishes as we decrease  $a$ . Time-series are shifted on the vertical axis for clarity. *Lower panel* : We plot the probability distribution function (PDF) of the global velocity  $P(V)$  for four different  $a = (1.0, 0.5, 0.4, 0.01)$  in Fig. (a - d) respectively. We consider three different  $\eta$  for each  $a$ , same as in upper panel. In Fig. (a) plot of  $P(V)$  is clearly bimodal, and as we decrease  $a$  it becomes to uni-modal in Fig. (d). All the plots are for  $N = 5000$ . 54

Figure 4.3 Plot of the Binder cumulant  $U$  vs. the noise strength  $\eta$  for four different distance dependent parameter  $a$ . Fig. (a-d) are for  $a = 1.0, 0.5, 0.4, 0.01$  respectively.  $U$  varies discontinuously from  $1/3$  (disordered state) to  $2/3$  (ordered state) in Fig. (a), and it goes continuously from  $1/3$  to  $2/3$  in Fig. (d). Discontinuity in the variation of  $U$  increases with system size for  $a \gtrsim 0.4$ , and it decreases for  $a \lesssim 0.4$ . Symbols have the same meaning as in Fig. 4.1. 55

Figure 4.4 *Main* : Schematic phase diagram of the disorder-to-order transition in noise strength  $\eta$  and distance dependent parameter  $a$  ( $\eta, a$ ) plane. For all  $a > 0$  there is a phase transition from a disordered to an ordered phase with decreasing  $\eta$  across the critical noise strength line. Dashed line indicates the nature of the transition is continuous, whereas solid line indicates the discontinuous transition. The nature of transition changes from discontinuous to continuous at a tri-critical point  $a_{TCP}$ (square). *Lower inset*: we compare with the mean-field calculation of the critical noise strength  $\eta_c$  for different  $a$  with our numerical data. Mean field results fit well with numerical data for small values of  $a$ . In upper inset : plot of  $1 - a_{TCP}$  vs.  $1/N$  shows the variation of TCP with system size. We find  $a_{TCP}$  converges to  $a \approx 0.39$  for  $N \rightarrow \infty$ (thermodynamic limit). 56

Figure 4.5 [Color online] Plot of real space snapshots of the particle density distribution for four different  $a$ (1.0,0.5,0.4,0.01). *Upper panel*: Plot of the particle density distribution for  $a = 1.0$  and  $a = 0.5$  from left to right respectively. *Lower panel*: Plot of the particle density distribution for  $a = 0.4$  and  $a = 0.01$  in the same order. Color bar shows the number of particles in a unit sized sub-cell. 57

Figure 4.6 Plot of the average density phase separation order parameter  $\langle Q \rangle$  vs.  $a$ , and the average standard deviation in particle number in a unit cell  $\langle \Delta\phi \rangle$  vs.  $a$  are shown in Fig. (a) and (b) respectively in log-log scale.  $\langle Q \rangle$  and  $\langle \Delta\phi \rangle$  decay exponentially from  $a = 1.0$  to  $a \approx 0.2$ . Both show similar power law decay with the exponent 0.13, for small values of  $a$ . In the insets of Fig (a) and (b), we show the exponential decay of the  $\langle Q \rangle$  ( $\sim e^{0.46a}$ ) and  $\langle \Delta\phi \rangle$  ( $\sim e^{0.33a}$ ) in semi-log scale. 58

- Figure 4.7 Plot of  $F(q, a) = \frac{(a \ln(a) + 1 - a)}{(\ln(a))^2} - \frac{D_v q^2}{2} \left[ \left( \frac{\lambda}{v_0} - 1 \right) + \sqrt{\left( \frac{\lambda}{v_0} - 1 \right)^2 + \frac{1}{2v_0}} \right]$  vs. wave vector  $q$ . For  $v_0 = 0.5$ ,  $D_v = 1.0$ ,  $\lambda = 1.0$ ,  $\alpha_0 = 1.0$ .  $F(q, a)$  becomes +ve for small  $q$ , which suggests that hydrodynamic mode becomes unstable at smaller wave vector. Region of instability continuously increases with increasing  $a$ . 59
- Figure 5.1 Plot of the global order parameter  $V$  with different system sizes  $N$  for four different values of  $\sigma$  (0.0, 0.0005, 0.005 and 0.05) are shown in (a-d), respectively. Black circles are numerical data and red line is exponential fitting of the numerical data points. We consider density of the system  $\rho = 1$ . 72
- Figure 5.2 Plot of the global order parameter  $V$  time series for five different values of  $\sigma = 0, 0.005, 0.01, 0.03$  and 0.05. We have considered  $224 \times 224$  system, and the mean density of the system  $\rho = 1$ . 72
- Figure 5.3 Snapshots of the system at steady state for different values of  $\sigma$ . We have considered  $224 \times 224$  system and density  $\rho = 1$ . 73
- Figure 5.4 Plot of the probability distribution of the number of neighbors  $P(N)$  vs. number of neighbors  $N$  for different values of  $\sigma = (0, 0.0005, 0.001, 0.01)$  and 0.05. Inset: Plot of  $P(N)$  vs. scaled number of neighbors  $N/N_c$ . We consider  $318 \times 318$  system size and density  $\rho = 1$ . 73
- Figure 5.5 Plot of  $\langle \Delta \phi \rangle$  vs.  $\sigma$  for two different system sizes  $142 \times 142$  and  $224 \times 224$ . The dashed line represents slope of  $-0.20$ . We have considered density  $\rho = 1$ . 74
- Figure 5.6 Plot of  $\langle C \rangle$  vs.  $t$  for different  $\sigma = 0, 0.001, 0.005$  and 0.05 of the Gaussian distribution. We have considered  $142 \times 142$  system size and the auto correlation is averaged over 20 ensembles. Density of the system  $\rho = 1$ . 74
- Figure 5.7 Plot of  $t_c$  vs.  $\sigma$  for different densities of the external agents  $\rho_a$ . We have considered three different external agent density ( $\rho_a = 0.005, 0.01$  and 0.05). We have consider  $142 \times 142$  system size and the  $t_c$  is averaged over 20 ensembles. 75

- Figure 6.1 Upper panel: (a) Plot of the correlation length  $L_c$  vs. time  $t$  for different activity  $\lambda$ . Lower panel: (b) Plot of scaled  $L_c/t^{0.25}$  vs.  $t$  for different activity  $\lambda$ . The dashed line in the lower panel represents the slope of the  $L_c/t^{0.25}$  vs.  $t$  plot. We have considered  $512 \times 512$  system size, and  $L_c$  is averaged over 20 ensembles. 79
- Figure 6.2 Plot of snapshots of the system at time  $t = 2000$  for the activity  $\lambda = 0$  (passive), 0.5, 1.0, 4.0 from (a-d), respectively. We have considered critical mixture  $\psi(\mathbf{r}, t)$  is 0.0, and system size is  $256 \times 256$ . 80
- Figure 6.3 Plot of  $C(\mathbf{r}, t)$  vs.  $\mathbf{r}/t^\gamma$  at different times for  $\lambda = 1$ .  $\gamma = 1/3$  for  $t < 50000$  and  $\gamma = 1/4$  for  $t \geq 50000$ . We have considered  $256 \times 256$  system size, and  $C(\mathbf{r}, t)$  is averaged over 20 ensembles. 81
- Figure 6.4 Upper panel: Plot of  $C(\mathbf{r}, t)$  vs.  $\mathbf{r}$ , and  $C(\mathbf{r}, t)$  vs.  $\mathbf{r}/L_c$  for  $\lambda = 0$  are shown in (a) and (b), respectively. Lower panel: Plot of  $C(\mathbf{r}, t)$  vs.  $\mathbf{r}$ , and  $C(\mathbf{r}, t)$  vs.  $\mathbf{r}/L_c$  for  $\lambda = 1.0$  are shown in (a) and (b), respectively. We have considered  $256 \times 256$  system size and number of realizations is 20. 82
- Figure 6.5 Plot of  $C(\mathbf{r}, t)$  vs.  $\mathbf{r}$  at  $t = 10^5$  for different  $\lambda$  is shown in (a). Plot of  $C(\mathbf{r}, t)$  vs.  $\mathbf{r}/L_c$  at  $t = 10^5$  for different  $\lambda$  is shown in (b). We have considered  $256 \times 256$  system size and number of realizations is 20. 82
- Figure 6.6 Upper panel: (a) Plot of the correlation length  $L_c$  vs. time  $t$  for different activity  $\lambda$ . Lower panel: (b) Plot of scaled  $L_c/t^{0.25}$  vs.  $t$  for different activity  $\lambda$ . The dashed line in the lower panel represents the slope of the  $L_c/t^{0.25}$  vs.  $t$  plot. We have considered  $256 \times 256$  system size, and  $L_c$  is averaged over 20 ensembles. 83
- Figure 6.7 Plot of  $C(\mathbf{r}, t)$  vs.  $\mathbf{r}$  for  $\lambda = 0$  and 1 are shown in (a) and (c), respectively. Plot of  $C(\mathbf{r}, t)$  vs.  $\mathbf{r}/L_c$  for  $\lambda = 0$  and 1 are shown in (b) and (d), respectively, where  $L_c$  is average correlation length. We have considered  $256 \times 256$  system size and number of realizations is 20. The order parameter value is -0.2, which gives 40:60 off-critical mixture. 84

Figure 6.8 Plot of  $C(\mathbf{r}, t)$  vs.  $\mathbf{r}$  at  $t = 10^5$  for different  $\lambda$  is shown in (a). Plot of  $C(\mathbf{r}, t)$  vs.  $\mathbf{r}/L_c$  at  $t = 10^5$  for different  $\lambda$  is shown in (b), where  $L_c$  is average correlation length. We have considered  $256 \times 256$  system size and number of realizations is 20. The order parameter  $\psi(\mathbf{r}, t)$  is -0.2. 84

Figure 6.9 Plot of  $\ln(L_c)$  vs.  $\ln(t)$  and  $\alpha$  vs.  $\ln(t)$  for noise free  $\eta(p) = 0.0$ , additive  $\eta_a(p) = 0.1$  and multiplicative  $\eta_m(p) = 0.1$  noise in passive modelB are shown in (a) and (b) respectively. Plot of  $\ln(L_c)$  vs.  $\ln(t)$  and  $\alpha$  vs.  $\ln(t)$  for noise free  $\eta(a) = 0.0$ , additive  $\eta_a(a) = 0.1$  and multiplicative  $\eta_m(a) = 0.1$  noise in active modelB are shown in (c) and (d) respectively. Here for active model B we consider the  $\lambda = 1.0$ . For all cases correlation length  $L_c$  is averaged over five ensembles, and system size is  $256 \times 256$ . 85

---

## INTRODUCTION

---

Statistical mechanics is a branch of physics that started at the end of eighteenth century with the novel works of James Clerk Maxwell, Ludwig Boltzmann, Josiah Willard Gibbs and Albert Einstein, and it introduces the reader to a general framework and viewpoint of different systems with a large number of degrees of freedom. It also aims to bridge the macroscopic thermodynamic properties to the microscopic properties of the matter which helps to predict the statistical properties of fluctuations on different length and time scales. Let us first introduce the connection between thermodynamics and statistical mechanics. Let us consider a physical system comprised of  $N$  identical particles confined in a space of volume  $V$ , and have total energy  $E$ . The macrostate of the system is defined by variables  $(N, V, E)$ . On the other hand, there will be a large number of possible arrangements in which the total energy  $E$  of the system can be distributed among the  $N$  particles. Each of these possible arrangements specifies a microstate of the system [1-4]. Therefore, the number of variables that are required to describe the microscopic state in 3-dimensions (3D) is  $6N$  ( $3N$  for position and  $3N$  for momentum), where  $N$  is the number of molecules. This  $6N$  dimensional space constructs the *phase space* of the system, and each point in this phase space is a microstate of the system. Whereas a macrostate consists of a large number of microstates, and it represents a volume in the phase space. In microscopic approach it is difficult to keep track of each degrees of freedom, but we can specify the probability  $dP$  of the system in an elemental volume  $dV$  of the phase space using statistical description. This probability can be defined as  $dP = \lim_{T \rightarrow \infty} dt/T$ , where  $dt$  is the time spent by the system in the volume  $dV$  and  $T$  is the total time over which the system is tracked. Average of any statistical quantity

$f(t)$  along the trajectory is defined  $\bar{f} = \lim_{T \rightarrow \infty} \frac{1}{T} \int_0^T f(t) dt$ . In this approach the *time average* of the statistical quantity is calculated. Alternative method to calculate the average of any statistical quantity called *ensemble average*. In this method each point in the phase space volume corresponds to different copies of the same system, and called as an ensemble. If  $\bar{N}$  is the number of copies corresponding to the volume  $V$ , and  $d\bar{N}$  is the number of copies corresponding to  $dV$ , then the probability of the system lying in  $V$  is defined as  $d\bar{P} = \lim_{\bar{N} \rightarrow \infty} \frac{d\bar{N}}{\bar{N}} = \rho(q_i, p_i) dV$ , where  $q_i$  and  $p_i$  represent  $3N$  position and momentum coordinates.  $\rho(q_i, p_i)$  is the density in the ensemble space. Average of any quantity  $f$  can be obtained as  $\langle f \rangle = \int f \rho dV$ , where  $\rho$  is the probability density. Equilibrium statistical mechanics is mainly based on the following hypothesis: (i) the ergodic hypothesis - both the descriptions of averaging discussed above are completely equivalent, (ii) the Boltzmann's hypothesis - if the volume filled by a trajectory in phase space is  $V$ , then the entropy  $S$  of the system is  $S = k \ln V$ , where  $k$  is the Boltzmann's constant, and (iii) principle of a priori - all the microstates which are compatible to a macrostate are equally probable. The Boltzmann's hypothesis bridges the thermodynamics and the statistical mechanics, and the ergodic hypothesis ensures the system is internally consistent [1-3, 5].

Most of the natural systems violate the general hypothesis of the equilibrium statistical mechanics. In last three decades, there has been significant progress in understanding of different phenomena of natural systems like collective behavior in different biological and cellular systems [6-8]. As these systems do not follow the usual formalisms of the equilibrium statistical mechanics are known as nonequilibrium systems. Understanding the broad range of nonequilibrium phenomena in terms of the statistical mechanics as well as the thermodynamic framework is an emerging area of current research. In this thesis our works mainly focus on active systems, a special class of nonequilibrium systems, and their statistical properties.

## 1.1 ACTIVE MATTER SYSTEMS: OUT-OF-EQUILIBRIUM

Active matter is a nonequilibrium system and it is abundant in nature. In this section we introduce various examples of the *Active Matter* systems [9-16]. As we go along, we will

discuss about the origin of this subfield and different fascinating features of it where physics enters biology in two wide and overlapping areas: (i) information and (ii) mechanics [17, 18]. We will emphasize on the mechanics, statistics of living matter in this thesis. The unifying characteristic of these systems (active matter) is that they are composed of large numbers of Self-propelled particles (SPPs) and have the ability to transduce ambient free energy into systematic movement [19–25]. The interaction among these SPPs and with the medium give rise to highly correlated collective motion. In addition to these real systems there are ample varieties of artificially designed systems, *e. g.*, active colloids [26–28], active polar disks [29], vibrated granular media [30–33], chemically boosted wire-cuts [34]. The active systems do not follow the general framework of the equilibrium thermodynamics and statistical mechanics [1, 3, 4, 35, 36]. The inherent property of these systems is that they show collective and coherent motion in wide range. In vitro mixtures of cell extracts of biofilaments and associated motor proteins as shown in a study by Surrey *et al.* [9], bacterial suspensions [12], and human melanocytes cells [37] are some of the examples which show collective behavior in micrometer range. On the other hand, bird flock, fish school [38, 39], collection of robots [40], *etc.* show flocking behavior in meter or some fraction of kilometer range.

In the above mentioned systems, each SPP moves forward at the cost of its internal energy which is transduced to mechanical energy. Here the dissipated energy is not correlated with the input, like equilibrium systems, *viz.*, Brownian motion. Due to energy injection at the individual particle level the active systems are not similar to the other out-of-equilibrium systems like a bulk fluid sheared from the top [41, 42] or driven diffusive systems [43]. However, a nonequilibrium steady-state (NESS) can be defined similar to other out-of-equilibrium systems [43]. Unlike the true equilibrium system where the macroscopic properties statistically remain unchanged with time, *i. e.*, a *steady-state* prevails, here a NESS is defined when relevant macroscopic observables statistically remain the same with time. We can understand NESS by taking an example of a bird flock where all the agents of the flock move coherently.

Let us consider  $P(C, t)$  is the probability of finding the system in a microscopic configuration  $C$  at time  $t$ . The time evolution of  $P(C, t)$  is defined by the master equation

$$\frac{dP(C, t)}{dt} = \sum_{C' \neq C} [W(C' \rightarrow C)P(C', t) - W(C \rightarrow C')P(C, t)], \quad (1.1)$$

where  $W(C' \rightarrow C)$  is the transition rate from configuration  $C'$  to  $C$ . At the steady state,  $P(C, t)$  is no longer function of time hence L.H.S. of the Eq. 1.1 will vanish. Therefore, the probability of the system going from configuration  $C$  to  $C'$  is same as to the probability of the system going from  $C'$  to  $C$ . Hence, the detailed balance is satisfied, which sets the temperature of the system. But, active system does not satisfy the hypothesis of detailed balance because there exists some non-zero current (*e.g.*, energy current) in the steady state. In some cases of active matter, an *effective temperature* can be defined in certain limit of associated parameters. Hence, an effective fluctuation-dissipation-relation (FDR) can be defined [44–49].

Another important feature of the active systems is that density fluctuations is much larger than usual equilibrium systems in the steady state. In real space, if a region of volume  $V$  contains  $N$  number of particles on average, the system generally shows fluctuations with standard deviation  $\Delta N \propto \sqrt{N}$  provided that the system is not close to critical point. In active matter systems the density fluctuations grow faster than  $\sqrt{N}$ , and in two dimensions it also grows as fast as  $N$  in some cases [20, 50].

## 1.2 CATEGORIES OF ACTIVE MATTER SYSTEMS

### 1.2.1 *Dry and wet systems*

In this thesis we will focus on various generic aspects of the large-scale behavior of the active matter systems and characterize their properties. We will also discuss different universality classes based on symmetry and conservation laws with a well-defined macroscopic behavior. These systems are in contact with a substrate during their motion. They can be described *with* or *without* momentum conservation depends on the system parameters, and the length scale of interest. The systems where the substrate provides only friction, can be modeled as a system with overdamped dynamics and no-momentum conservation. These systems without momentum conservation can be described as *dry* active matter systems. Examples of these systems are like bacteria gliding on a rigid surface [51], animal herds on land [52], and in artificial domain vibrated granular particles on a plate [29, 31, 50, 53, 54]. In the same category, it is possible to model some systems like collections of swimming bacteria

[55] and motor-filament suspensions [56] without an explicit ambient fluid. In these models, steric plus stochastic effects could put underground the hydrodynamic interactions. In minimal flocking models we observe areal displays by a large group of birds, and the interaction among them is short range [57]. In all of these above mentioned systems momentum is damped by friction with the substrate. On the other hand, for solvent-mediated hydrodynamic interactions the dynamics of the suspending fluid must be considered. The systems (fluid+particles) with momentum conservation are referred as *wet* active matter systems. Examples of these systems are suspensions of catalytic colloidal rods [34], cell cytoskeleton and cytoskeletal extracts in bulk suspensions [13], swimming bacteria in bulk [12] and Pt. catalytic colloids [58]. The system of interest can be *dry* or *wet* depending on interaction with the medium. But we can also consider the length scale of interest and select models (momentum conserved / momentum non-conserved) accordingly.

In this thesis we will discuss about some key features of the *dry* polar active matter systems. The number of particle is the only conserved quantity of the system (birth and death are neglected). Individual active particles of the systems can be of different kind depending on their shape and symmetry. In the next section we will introduce different types of active particles.

### 1.2.2 Polar and apolar systems

Depending on the symmetry of the active particles we can classify them as (i) polar particles - head and tail can be distinguished [38, 59, 60], and (ii) apolar particles - head and tail can not be distinguished [61, 62]. Polar particles can align parallel or anti-parallel to each other. Therefore, they will form either a polar ordered state with net flow velocity or an apolar ordered state with zero flow velocity, as shown in Fig. 1.1. On the other hand, apolar particles don't have polarity and form nematic ordered state, as shown in Fig. 1.1. Ordered state of polar particles is defined either by vector or by nematic order parameter, and ordered state of the apolar particles is defined by nematic order parameter. Now, we will briefly describe the characteristics of the polar active particles or (self-propelled particles (SPPs)). These SPPs show remarkable features during their motion, like, they show coherent motion

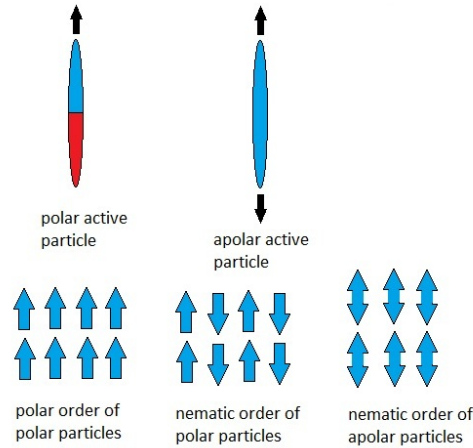


Figure 1.1: Schematic of the various types of active particles and their orientationally ordered states. Polar active particles (top left image), such as bacteria or birds, have a head and a tail and are generally self-propelled along their long axis. They can order in polar states (bottom left) or nematic states (bottom center). The polar state is also a moving state with a nonzero mean velocity. Apolar active particles (top right image) are head-tail symmetric and can order in nematic states (bottom right).

when they are put in a collection. This fascinating feature was explained in 1995 by Vicsek *et al.* using a simple rule based model [57], renowned as *Vicsek Model* (VM). In the same year Toner *et al.* predict the existence of a long-range *ordered phase* of flocks, in which all the SPPs of a large flock move together with a non-zero mean velocity in two dimensions (2D) [52, 63]. In Vicsek model the SPPs interact with their neighbors through a short range alignment interaction. The mean density of the system controls the number of interacting neighbors and the randomness in alignment interaction is represented as noise in the system. The density and noise are the two main control parameters of these systems. The system shows a nonequilibrium phase transition from a disordered state at low density or high noise to an ordered (coherently moving) state at high density or low noise strength. Using hydrodynamical equations of motion for density and polarization field, Toner *et al.* find that the flocks exhibit a true long-range ordered spontaneously broken rotational symmetry state in 2D, whereas there exist no broken symmetry state in 2D in equilibrium system with continuous symmetry (*Mermin-Wagner* theorem). Recently, the Toner and Tu model is derived by coarse graining the microscopic Vicsek model using the Boltzmann-equation and

fluctuating hydrodynamic approach [64–66]. These descriptions provide microscopic basis for the hydrodynamic theory.

On the other hand, systems consist of apolar particles show large number fluctuations in comparison to their equilibrium counterparts. In a study, Ramaswamy *et al.* predicted that the number fluctuation  $\Delta N$  is proportional to the mean number of SPPs  $\langle N \rangle$  in the system in 2D [50]. This large number fluctuations in apolar systems is called as *Giant number fluctuation* (GNF). Later on experimental studies confirm the existence of GNF in apolar systems [31, 67]. Chaté *et al.* also find the existence of Kosterlitz-Thouless-like transition to quasi-long-range orientational order for apolar systems [67].

In Vicsek like systems, the alignment interaction plays crucial role in the formation of "ordered state". In these systems the SPPs are generally elongated and can order in states with either polar or apolar (nematic) orientational order. Another interesting class of SPPs which can be distinguished from their head and tail during their motion, but they are symmetric in shape [68–72]. These types of particles are called as *Active Brownian particles* (ABP). Hence, simple volume exclusion will not lead to a polar/apolar ordered state. There is no alignment interaction as proposed in the Vicsek model and these particles do not show large-scale alignment. However, above a packing fraction  $\Phi_c \approx 0.4$  (much smaller than  $\Phi_c$  for random close packing in 2D) this minimal system phase separates into solid like and gas phases. Hence, they also exhibit large number fluctuations like polar and nematic systems above the critical packing fraction  $\Phi_c$  [68]. There is another variety of polar SPPs, run-and-tumble particles, which perform self-propulsion by a sequence of *runs*. During these runs they move with almost constant speed and change their direction by sudden and rapid randomizations in direction or *tumbles* [47, 73, 74]. In a recent study, Tailleur *et al.* discuss about the domain formation and other collective phenomena of these systems [47]. Our studies mainly focus on polar SPPs and ABPs only.

### 1.3 INHOMOGENEITY AND CONFINEMENT

In addition to the extensive study of active systems in clean environments [19, 21, 57, 75, 76], recently people have started to look for their bulk properties in heterogeneous medium [77–

86]. The motion of flocks, herds, and swarms through different kind of disordered environment and confined medium is an emerging field of research in the last five years, and these studies are crucial not only to animal groups in the wild, but also to effective applications of collective robotics and active materials composed of synthetic motile units. In this section we will briefly discuss about some of the important studies of active particles in heterogeneous medium. In a recent study, Morin *et al.* examine the motion of motile colloids in a randomly positioned microfabricated obstacles [78], and they find that for a sufficient disorder density the collective motion is suppressed in the form of a first-order phase transition generic to all polar active materials. In recent studies, the effect of heterogeneity is discussed on the long-range ordering behavior of a collection of SPPs moving on a 2D substrate [79, 84, 86]. It is observed that long-range ordering is destroyed in the presence of quenched heterogeneity and system shows a quasi long range ordered state.

Besides the studies about active particles in the presence of different kinds of inhomogeneity, there are numerous studies about SPPs in confined geometries. In equilibrium physical systems the diffusive transport of particles is a ubiquitous feature. In a recent article, Burada *et al.* investigated the stochastic transport of Brownian particles in microsized geometries of varying cross sections and in narrow channels wherein the diffusing particles are hindered from passing each other (single-file diffusion) [87]. Authors find that for particles undergoing biased diffusion in static suspension media enclosed by confining geometries, transport exhibits intriguing features such as 1) a decrease in nonlinear mobility with increasing temperature also 2) a broad peak of the effective diffusion above the free diffusion limit. They also report that the rectification or segregation of the diffusing Brownian particles becomes possible if the suspension medium is subjected to external and time-dependent forcing. Furthermore, in very narrow spatially modulated channels the particle-particle interactions can induce anomalous sub-diffusion. As the confinement gives rise to many fascinating features like rectification and segregation in passive (equilibrium) systems which motivates people to study the active systems in different confined geometries. Recent study of Dey *et al.* show that the confinement can enhance the average rate of binding of the motor-cargo complexes to the microtubule, which leads to an enhancement in the average velocity [88]. In another work, Stark *et al.* report that the asymmetric channel corrugation induces a netflux in the

motion of microswimmers along the channel, the strength and direction of which strongly depends on the swimmer type [89]. Furthermore, a non-zero average drift can be induced in ABP using potential modulation between two directions in a 2D periodic corrugated channel [90]. In this thesis in chapters 2 and 3 we will discuss some key features of SPPs in confined geometries.

## 1.4 METHODOLOGY

Active systems are non-equilibrium systems, hence the framework of characterizing or understanding the different complex and fascinating behaviors of these systems are not similar to their equilibrium counter part. Since there is no conservation of energy, it is not possible to write an effective Hamiltonian to describe such system. In last three decades, there are enormous number of studies about active systems based on following three approaches: (i) microscopic rule-based study like Vicsek model (VM) [57, 91], and also the derivation of coarse-grained equations for slow variables from the rule based models [64, 65], (ii) phenomenological approach, writing different terms in the hydrodynamic equations of motion based on symmetry of the system, (iii) and obviously the experiments are always encouraging and give more insight about these systems [32, 34, 53, 92]. In the next section we discuss about the different techniques which we have used in our studies.

### 1.4.1 *Microscopic rule based study or agent based simulation*

Agent based or direct rule based simulation is commonly used technique to study active matter systems. In this technique one consider a collection of pseudo-particles, and update their positions and velocities according to fixed dynamical rules. In this method, the microscopic update rules are adopted looking at the phenomenology of the concerned active system. Active shape asymmetric agents move along their long body axis. For finite size particles volume exclusion or steric effects can guide them to align with their neighbors in contact [68, 75, 93, 94]. For polar agents the interactions can be thought of like "ferromagnetic" interaction in spin systems. On the other hand, for apolar agents both parallel and anti-parallel

interactions are possible. Many studies are done considering the agents as point particles, but alignment interactions (polar/apolar) are kept by hand to mimic the alignment due to the finite size of the agents [57, 91]. The interactions are always not exact, *i.e.*, the SPPs make errors following their neighbors. These errors are accounted by appropriate noise term in the update rule [57, 91].

#### 1.4.1.1 Vicsek Model (VM)

Vicsek model (VM) is a rule based model, which is the first insightful study about the collective behavior of a two-dimensional polar SPPs [57]. The work find the clustering, transport, and phase transition in the active systems. In this model, each particle interacts with its neighbors through a short range alignment interaction, and they (SPPs) move in the average direction of all the neighbouring particles within an interaction radius. However, the particles make errors during their motion in the average direction which is taken care by considering a random noise in the system. The update rule governs the position  $r_i(t)$  and orientation  $\theta_i(t)$  update.

$$\mathbf{r}_i(t+1) = \mathbf{r}_i(t) + \mathbf{v}_i \Delta t, \quad (1.2)$$

where  $\mathbf{v}_i$  is the self-propulsion speed of the  $i^{\text{th}}$  particle.

$$\theta(t+1) = \langle \theta(t) \rangle_r + \eta \Delta \theta, \quad (1.3)$$

where  $\langle \theta(t) \rangle_r$  is the average direction of the  $i^{\text{th}}$  particle (including the particle itself) being within a radius  $r$  surrounding the given particle.  $\Delta \theta$  is the noise which takes care of the error and it varies between  $-\pi$  to  $\pi$ .  $\eta$  is the noise strength which varies in the range  $[0, 1]$ . Noise introduced here is such that it rotates the mean alignment of the particle due to its neighbors by a small angle. Hence, it is called as "angular" noise. The density  $\rho$  of the particles and noise strength  $\eta$  are the two control parameters of the system. Authors characterized the collective motion of the particles at different limit of density and noise strength: (i) for small densities and noise the particles tend to form groups moving coherently in random directions, (ii) at higher densities and noise the particles move randomly with some correlation, and (iii)

for higher density and small noise the motion becomes ordered [57]. Furthermore, they also studied the order-disorder phase transition of the system and find that the transition is continuous. Also different critical exponents are estimated as they are usually present in equilibrium systems undergoing a phase transition.

**NOISE: ANGULAR AND VECTOR:** After about a decade of Vicsek's study, a debate started about the nature of the order-disorder transition of the polar SPPs. In 2004, Chaté and his collaborators introduced another type of noise which add a small vector to the resultant vector of all the direction vectors of the neighbors (including the particle itself). This noise is called as "vector" noise [75, 76, 91]. The position update rule for the SPPs is same as in VM, but the orientation update is modified as following,

$$\theta_j(t+1) = \arg \left[ \sum_{k \in r} \exp(i\theta_k(t)) + \eta n_j(t) \exp(i\psi_j(t)) \right], \quad (1.4)$$

$\arg(\mathbf{x} = (x_1, x_2)) = \text{atan}\left(\frac{x_2}{x_1}\right)$ ,  $n_j(t)$  is the number of neighbours of the  $j^{\text{th}}$  particle within its interaction range  $r$  at time  $t$ . The advantage of using vector noise is that the influence of it decreases with increasing local order, whereas the intensity of the angular noise is independent of local alignment. They also note that for angular noise the nature of the order-disorder transition becomes discontinuous provided one considers large enough system size because the finite size effect is much more dominant for angular noise [57] as compared to the vectorial choice [91]. The nature of the phase transition in these systems is still topic of debate. In various studies the nature of the transition depends on the update mechanism of the system [95]. Now, it is believed that the density phase separation is the key to make the transition first order [72, 96]. But there is still lack of experiments to settle the debate about the nature of the phase transition.

#### 1.4.1.2 Langevin dynamics for active particle

The passive or Brownian particle suffers collisions from its surrounding medium and their dynamics is determined by stochastic collisions. In equilibrium, there is a balance between

dissipation and fluctuations in the system, and both of them are related by fluctuation-dissipation relation (FDR) [2, 3]. Dynamics of passive particles can be described by Newtonian dynamics including friction and stochastic force [97]. Hence, motion of Brownian particle with Stokes friction coefficient  $\gamma$  in a space dependent potential  $U(\mathbf{r})$  can be written by Langevin dynamics.

$$m \frac{d\mathbf{v}}{dt} = -\gamma\mathbf{v} - \nabla U(\mathbf{r}) + \mathbf{F}(t), \quad (1.5)$$

where  $\mathbf{F}(t)$  is the temporally short correlated random force and  $\langle \mathbf{F}(t) \rangle = 0$ .  $\langle F_i(t)F_j(t') \rangle = 2D_p\delta_{i,j}\delta(t-t')$ , where the components  $F_i(t)$  are referred to as Gaussian white noise with intensity  $D_p$ , and  $i, j$  are correspond to the Cartesian coordinates. In equilibrium  $D_p$  and  $\gamma$  are related by FDR,  $D_p = \gamma k_B T$  where  $k_B$  and  $T$  are the Boltzmann constant and temperature of the system, respectively.

ABPs are in general symmetrical in shape, hence there is no alignment interactions. But the active nature of these particles induces motility induced phase separation (MIPS) [68] at much lower density than passive particles. In different systems like granular materials and living organisms, the particles move in dense fluid or high frictional substrate. Therefore, the first term of Eq. 1.5 can be neglected in the overdamped limit. Now the dynamics of the ABP is given by following equations

$$\partial_t \mathbf{r}_i = v_0 \mathbf{n}_i + \mu \sum_{j \neq i} \mathbf{F}_{ij} + \boldsymbol{\eta}_i^T(t) \quad (1.6)$$

$$\partial_t \theta_i = \eta_i(t), \quad (1.7)$$

where ABPs are considered as soft repulsive disk of radius  $r$  to take care of the steric effect. The direction of motion of the particle defined by unit vector  $\mathbf{n}_i = (\cos(\theta_i), \sin(\theta_i))$ , where  $\theta_i$  is the orientation of the  $i^{\text{th}}$  particle. The first term in the R.H.S of Eq. 1.6 is due to self-propelled nature of the ABP, and  $v_0$  is the self-propulsion speed of the particle.  $\boldsymbol{\eta}_i^T(t)$  is a translational Gaussian white noise with zero mean and correlations  $\langle \eta_{i\alpha}^T(t) \eta_{i\beta}^T(t') \rangle =$

$2D\delta_{ij}\delta_{\alpha\beta}\delta(t-t')$ , where  $\alpha, \beta$  denotes Cartesian coordinates and diffusion constant  $D = k_B T \mu$ .  $\eta_i(t)$  is a rotational Gaussian white noise with zero mean and correlations  $\langle \eta_i(t)\eta_j(t') \rangle = 2v_r\delta_{ij}\delta(t-t')$ ,  $v_r$  is the rotational diffusion rate and  $\mu$  is the mobility.  $\mathbf{F}_{ij}$  is short range repulsive force between  $i^{\text{th}}$  and  $j^{\text{th}}$  particle. In the study of Fily *et al.* [68],  $\mathbf{F}_{ij} = -k(2a - r_{ij})\mathbf{n}_{ij}$  if  $r_{ij} < 2a$  and  $\mathbf{F}_{ij} = 0$  otherwise. In another study of ABP, Stark *et al.* consider the Weeks-Chandler-Andersen (WCA) potential as a soft repulsive potential between the ABP [98]. General properties of the ABPs should be independent of the specific form of the repulsive potential. In our study in chapter 3, we have considered WCA potential to study the dynamics of ABP in a periodic arrays of obstacles and confined channels.

#### 1.4.2 Phenomenology : hydrodynamic equations of motion

In this section we will discuss about the effective continuum theory of the flocking model as introduced in sec. 1.4.1.1. The effective continuum theory for flocking was first introduced by Toner and Tu in 1995 [52, 63]. The fundamental axioms of hydrodynamic theory are the conservation laws like conservation of mass, conservation of momentum and conservation of energy, *etc.* or terms are written based on underlying symmetries of the system. Toner and Tu also formulated the effective continuum model on the basis of symmetry considerations. Since for the dry active matter system the particles move on a frictional substrate and the particles constantly transform their internal energy into systematic motion, the only conserved field in the system is the density of active particles  $\rho(\mathbf{r}, t)$  (there is no death and birth of SPPs). Also these systems show coherent motion which leads to an ordered state which is defined by polarization vector field  $\mathbf{P}(\mathbf{r}, t)$ . The coarse grained fields  $\rho(\mathbf{r}, t)$  and  $\mathbf{P}(\mathbf{r}, t)$  are defined by,

$$\rho(\mathbf{r}, t) = \sum_i^N \delta(\mathbf{r} - \mathbf{r}_i(t)) \quad (1.8)$$

$$\mathbf{P}(\mathbf{r}, t) = \frac{1}{\rho(\mathbf{r}, t)} \sum_i^N \mathbf{n}_i(t) \delta(\mathbf{r} - \mathbf{r}_i(t)), \quad (1.9)$$

where the summation is over all the particles,  $\mathbf{r}_i(t)$  and  $\mathbf{n}_i(t)$  is the position and the unit orientation vector of  $i^{\text{th}}$  particle at time  $t$ .

Although, the active systems are non-equilibrium system, it is conventional to write the dynamical equations of motion for these systems as a combination of a free energy functional  $F_p$  which emerges due to the interaction among the particles plus terms due to activity.

$$\partial_t \rho(\mathbf{r}, t) + v_0 \nabla \cdot (\rho \mathbf{P}) = -\nabla \cdot \left( -\frac{1}{\gamma_\rho} \nabla \frac{\delta F_p}{\delta \rho} + \mathbf{f}_\rho \right), \quad (1.10)$$

$$\partial_t \mathbf{P} + \lambda_1 (\mathbf{P} \cdot \nabla) \mathbf{P} = -\frac{1}{\gamma} \frac{\delta F_p}{\delta \mathbf{P}} + \mathbf{f}, \quad (1.11)$$

where  $\gamma_\rho, \gamma$  are kinetic coefficients, and  $v_0$  is the self-propulsion speed of the active particles. First term in the R.H.S. of Eq. 1.10 represents diffusive density current, and the second term denotes conservative noise. The second term in the L.H.S of the Eq. 1.10 represents the active current which is proportional to the self-propulsion speed  $v_0$ .  $\lambda_1$  is the strength of the advective term in Eq. 1.11. This advective term resembles to the advective term of famous Navier-Stokes equation [36] for fluids. In active systems, the motion of the particles are *not constrained* by the *Galilean invariance* that would need  $\lambda_1 = 1$ . But in active flocks, the strength of the advective term  $\lambda_1$  is a non-universal phenomenological parameter which can be determined from microscopic model. In the Toner and Tu model,  $\mathbf{P}$  acts as both a velocity field and a local orientation order parameter of the system. Therefore,  $\mathbf{P}$  introduces a term for advection and flow alignment in Eq. 1.11, whereas  $\mathbf{P}$  acts as only velocity field in Eq. 1.10. The last term on the R.H.S in Eq. 1.11 captures the fluctuations in the system, and it is a Gaussian white noise with zero mean and correlations

$$\langle f_l(\mathbf{r}, t) f_m(\mathbf{r}', t') \rangle = 2\Delta \delta_{lm} \delta(\mathbf{r} - \mathbf{r}') \delta(t - t'), \quad (1.12)$$

where  $\Delta$  is a constant and dummy indices  $l, m$  represents Cartesian components.

In Eqs. 1.10, 1.11 the noise is considered as purely additive, and its dependency on order parameter  $\mathbf{P}$  and local density  $\rho$  is neglected. As we discussed in the continuum model for

active systems  $\mathbf{P}$  plays dual role, (i)  $\mathbf{P}$  is the orientational order parameter of the system and (ii)  $v_0\mathbf{P}$  represents the velocity field. This dual behavior of  $\mathbf{P}$  is important for determining the large scale characteristics of these systems. Now, the free energy functional in Eqs. 1.10 and 1.11 is given by,

$$F_P = \int_r \left[ \frac{\tilde{\alpha}(\rho)}{2} |\mathbf{P}|^2 + \frac{\tilde{\beta}}{4} |\mathbf{P}|^4 + \frac{\tilde{K}}{2} (\partial_i P_m)(\partial_i P_m) + \frac{w}{2} |\mathbf{P}|^2 \nabla \cdot \mathbf{P} - w_1 \nabla \cdot \mathbf{P} \frac{\delta \rho}{\rho_0} + \frac{A}{2} \frac{\delta \rho^2}{\rho_0} \right], \quad (1.13)$$

where  $\rho_0$  is the mean density of the system, and  $\delta \rho = \rho - \rho_0$  is fluctuation in density about its mean value  $\rho_0$ . The first two terms in Eq. 1.13 describe the order-disorder transition of the system.  $\tilde{\alpha}(\rho)$  is a microscopic model dependent parameter, like it depends on local density  $\rho$  and noise strength [64].  $\tilde{\alpha}$  goes to zero around critical point, and it becomes negative in the ordered state. Now to describe the physics near to transition one can write  $\tilde{\alpha}$  phenomenologically in the following manner,  $\tilde{\alpha}(\rho) = a_0(1 - \frac{\rho}{\rho_c})$ , where  $a_0$  is a positive constant and  $\tilde{\alpha}$  changes sign at  $\rho = \rho_c$ .  $\tilde{\beta}$  is positive to stabilise the system. The third term in Eq. 1.13 is due to energy cost of spatially inhomogeneous deformations of the coarse grained order parameter, and the Frank constant  $\tilde{K}$  is positive. These order-parameter deformation can arise from splay or bend deformations in 2D, and these deformations play important role in the active systems [99].  $w$  terms can be considered as correction to  $\tilde{\alpha}$  due to splay. The last term suppresses the density fluctuation of the system, and  $A$  is the compression modulus.

Now by using the free energy functional  $F_P$  of Eq. 1.13 we can write the hydrodynamic equation of motion of  $\mathbf{P}$  as,

$$\partial_t \mathbf{P} + \lambda_1 (\mathbf{P} \cdot \nabla) \mathbf{P} = -[\tilde{\alpha}(\rho) + \tilde{\beta} |\mathbf{P}|^2] \mathbf{P} + K \nabla^2 \mathbf{P} - v_1 \nabla \frac{\rho}{\rho_0} + \frac{\lambda}{2} \nabla |\mathbf{P}|^2 - \lambda \mathbf{P} (\nabla \cdot \mathbf{P}) + \mathbf{f}, \quad (1.14)$$

where  $v_1 = w_1/\gamma$  and  $\lambda = w/\gamma$  both have dimensions of velocity. All the parameters with tilde in Eq. 1.13 are divided by  $\gamma$  and are written without tilde in Eq. 1.14. Polarization  $\mathbf{P}$  equation of polar flock as in Eq. 1.14 has a fluid character, and in general  $\mathbf{P}$  is proportional to the flock velocity. Eq. 1.14 can be compared to Navier-Stokes equation for a fluid. The second term of the R.H.S of Eq. 1.14 represents the viscous force. The third and fourth term can be simplified as an approximate form of pressure gradient  $-(1/\rho_0)\nabla P$ , where considering to the leading order  $P(\rho) \approx v_1 \rho$ . This term highlights the similarity and contrast with the

Navier-Stokes equation. Writing the hydrodynamic equation for  $\mathbf{P}$  from general symmetry argument allows two more terms,  $(\lambda_3/2)\nabla|\mathbf{P}|^2 + \lambda_2\mathbf{P}(\nabla \cdot \mathbf{P})$  [63, 100]. The derivation based on free energy (Eq.1.13) using Eq. 1.11 produces  $\lambda_3 = -\lambda_2 = \lambda$ . Later on, using microscopic description Bertin *et al.* [64, 101] also find that  $\lambda_3 = -\lambda_2$ , and  $\lambda_i \sim v_0^2$ ,  $v_1 = v_0/2$ .

#### 1.4.2.1 Homogeneous steady states

Polar system undergoes order-disorder phase transition depending on system parameters like density and noise strength. The order-disorder transition is studied using mean field description in Toner and Tu model [52, 63]. For  $\alpha > 0$ , corresponding to  $\rho_0 < \rho_c$ , the homogeneous steady state of the system is disordered and isotropic state where order parameter of the system  $\mathbf{P} = 0$ . For  $\alpha < 0$  corresponding to  $\rho_0 > \rho_c$  the system is in the ordered state which gives a non-zero value of the order parameter  $\mathbf{P}$ ,  $|\mathbf{P}_0| = \sqrt{\frac{\alpha_0}{\beta}}$ , where  $\alpha_0 = \alpha(\rho_0)$ . The continuous rotational symmetry of the system is spontaneously broken in the ordered state and the flock moves with a velocity  $\mathbf{v} = v_0\mathbf{P}_0$ . The advective non-linearities in the hydrodynamic equation of motion of order parameter  $\mathbf{P}$  in Eq. 1.11 establishes long-range ordering in the system even in 2D. In the deep ordered state, the linearized hydrodynamics of Eqs. 1.10 and 1.14 suggests two sound modes. The presence of propagating sound modes suggest the existence of the symmetry broken state in the system in 2D.

#### 1.4.2.2 Two point correlations and giant number fluctuations

Using linearized calculation of hydrodynamic equations of motion one can calculate correlation functions and static structure factor  $S(\mathbf{q})$ .

$$S(\mathbf{q}) = \frac{1}{\rho_0 V} \langle \delta\rho_{\mathbf{q}}(t)\delta\rho_{-\mathbf{q}}(t) \rangle = \int_{-\infty}^{\infty} \frac{d\omega}{2\pi} S(\mathbf{q}, \omega), \quad (1.15)$$

where  $\delta\rho_{\mathbf{q}}$  is Fourier transform of the density fluctuations,  $S(\mathbf{q}, \omega)$  is the dynamical structure factor, and  $S(\mathbf{q}, \omega) = \frac{1}{\rho_0 V} \int_0^{\infty} dt \exp(i\omega t) \langle \delta\rho_{\mathbf{q}}(0)\delta\rho_{-\mathbf{q}}(t) \rangle$ , where  $V$  is the volume of the system and  $\mathbf{q}$  and  $\omega$  are wave vector and angular frequency of the hydrodynamic mode, respectively.  $\langle \delta\rho_{\mathbf{q}}(0)\delta\rho_{-\mathbf{q}}(t) \rangle$  gives the density auto-correlation of the system. Toner and Tu show that  $S(\mathbf{q}) \sim \frac{1}{q^2}$ . The  $\frac{1}{q^2}$  divergence at  $q \rightarrow 0$  reflects enormous long-wave length fluctuations in the system. The static structure factor  $S(\mathbf{q})$  is related to the number fluctuation

by  $\Delta N = \sqrt{S(\mathbf{q} \rightarrow 0)V}$ . The smallest accessible wave vector  $q \sim V^{-1/d}$ , where  $d$  is the dimension of space. Therefore,  $S(q \rightarrow 0) \sim V^{2/d} \sim \langle N \rangle^{2/d}$ , where  $\langle N \rangle$  is average number of particles in a region of size  $V$ . Hence, the number fluctuations  $\Delta N \sim \langle N \rangle^a$ , where  $a = \frac{1}{2} + \frac{1}{d}$ . Recent experiments find that the large number fluctuations for polar [29] and apolar [31] system is  $2a = 1.45 \pm 0.05$  and  $a = 1$ , respectively. Hence number fluctuation in these systems is large and also called as *Giant number fluctuation*.

## 1.5 COARSENING

In previous sections, we have discussed different features of a collection of SPPs or a single particle in the steady state. We also mention the role of noise, boundary and inhomogeneities in these systems. In this section, we will discuss about a class of fascinating studies about the kinetics of a system towards a steady state due to a rapid quench (changing the system parameters). A thermodynamically stable state or equilibrium state is determined by the global minimum of the associated free energy for a given set of parameter values. Also depending on the value of the different parameters, a system can exist in different phases, *e.g.*, water which can exist in three phases – liquid, solid and gas. Consider a fluid is in its solid state, and we rapidly heat it to a temperature where its preferred equilibrium phase is liquid. The system will take some time to convert from solid to liquid. The initial and the final states are understood by the properties of the corresponding equilibrium state, but understanding of the dynamical process is crucial. Over the years, there are many studies about the kinetics of phase transition for different systems, which help us about the basic understanding of different dynamical processes [102, 103]. We will first discuss about kinetics or coarsening of systems which approaches an equilibrium state, and then we will discuss about the coarsening in the active matter systems.

### 1.5.1 Coarsening in non-conserved systems (model A)

We shall discuss coarsening in the Ising model [104] as it is a simplest model with immense utilization. The Ising model was introduced to study phase transitions in magnetic systems.

In the Ising model spins can have either up ( $S_i = +1$ ) or down ( $S_i = -1$ ) orientation. Now to study the kinetics of the Ising model, one can consider that the system is connected to a heat bath that generates stochastic spin flips ( $S_i \rightarrow -S_i$ ). This random spin flip model is known as Glauber dynamics [105] where the corresponding order parameter of the system is non-conserved. Now we will discuss the dynamics of paramagnetic to ferromagnetic phase transition in the Ising model. We consider the system is in the paramagnetic state at  $T > T_c$ , and there is no external magnetic field ( $h = 0$ ). If we rapidly quench the system to  $T < T_c$  then the system will reach to its preferred equilibrium state with finite spontaneous magnetization. Also there will be domain formation and domains will coarsen with time. The coarsening of the domains is characterized by a characteristic domain length  $L(t)$ , and a finite system will order either with all up or down state at  $t \rightarrow \infty$ .

Now for the microscopic description of the Glauber kinetics we need an appropriate order parameter at the coarse-grained level to describe the system. We can consider the local magnetization  $\psi(\mathbf{r}, t)$  as a coarse-grained variable. The local magnetization in the Ising model is a scalar order parameter but the order parameter in Glauber dynamics can also be a vector, as in the XY model. The time dependent Ginzburg Landau (TDGL) theory governs the dynamics of the order parameter.

$$\frac{\partial}{\partial t} \psi(\mathbf{r}, t) = -\Gamma \frac{\delta G(\psi)}{\delta \psi} + \theta(\mathbf{r}, t), \quad (1.16)$$

where  $\Gamma$  is inverse damping coefficient, and  $G$  is the free energy functional which is defined as

$$G(\psi) = \int d\mathbf{r} [g(\psi) + \frac{1}{2} K (\nabla \psi)^2], \quad (1.17)$$

where  $g(\psi)$  is the local free energy, the second term in R.H.S is surface tension due to inhomogeneity in  $\psi$ , and  $K$  is the strength of the surface tension. In our study we have used the general form of the  $\psi^4$  free energy:

$$G(\psi) = \int d\mathbf{r} \left[ -\frac{a(T_c - T)}{2} \psi^2 + \frac{b}{4} \psi^4 - h\psi + \frac{K}{2} (\nabla \psi)^2 \right], \quad (1.18)$$

where  $a, b > 0$ , and  $T_c$  is the critical temperature of the system.

Using the expression for  $\psi^4$  free energy in Eq. 1.18 and without magnetic field the TDGL equation in Eq. 1.16 reduces to

$$\frac{\partial}{\partial t}\psi(\mathbf{r}, t) = \Gamma[a(T_c - T)\psi - b\psi^3 + K\nabla^2\psi] + \theta(\mathbf{r}, t). \quad (1.19)$$

Also by introducing rescaled variables one can obtain the dimensionless TDGL equation.

$$\frac{\partial}{\partial t}\psi(\mathbf{r}, t) = \psi - \psi^3 + \nabla^2\psi + \theta(\mathbf{r}, t), \quad (1.20)$$

where  $\langle\theta(\mathbf{r}, t)\rangle = 0$ ,  $\langle\theta(\mathbf{r}', t')\theta(\mathbf{r}'', t'')\rangle = 2\epsilon\delta(\mathbf{r}' - \mathbf{r}'')\delta(t' - t'')$ ,  $\epsilon = \frac{k_B T b [a(T_c - T)]^{(d-4)/2}}{K^{d/2}}$ .

### 1.5.2 Coarsening in conserved systems (model B)

In this section we will discuss the kinetics of conserved orderparameter systems like phase separation of a binary mixture. If we quench a binary mixture from homogeneous phase to segregated phase. Initially homogeneous state starts to phase separate as A rich and B rich domains. At the late time both species (A and B) will be completely phase separated. In this case the dynamics is different from the non-conserved one. The microscopic kinetics involves the diffusion of atoms, like atoms jump to the vacant site of the lattice or two species interchange in a binary mixture. In this mechanism there is spin exchange rather than spin flips. Therefore, if one spin  $S_i$  jumps from  $+1$  to  $-1$  then a neighboring spin  $S_j$  simultaneously jumps from  $-1$  to  $+1$ . This dynamics is known as Kawasaki dynamics [106].

The microscopic model for conserved model is defined by Cahn-Hilliard-Cook (CHC) equation. The order parameter of the system is defined by the relative density of the system  $\psi(\mathbf{r}, t) = n_A - n_B$ , where  $n_i$  is local density of the  $i^{\text{th}}$  species.

$$\frac{\partial}{\partial t}\psi(\mathbf{r}, t) = \nabla \cdot [D\nabla \frac{\delta G(\psi)}{\delta \psi} + \theta(\mathbf{r}, t)], \quad (1.21)$$

where  $D$  is the diffusion constant, and  $G$  refers to the free energy and as in Eq. 1.18. The noise is defined by  $\langle\theta(\mathbf{r}, t)\rangle = 0$  and  $\langle\theta_i(\mathbf{r}', t')\theta_i(\mathbf{r}'', t'')\rangle = 2Dk_B T\delta_{ij}\delta(\mathbf{r}' - \mathbf{r}'')\delta(t' - t'')$ . Using

the expression for  $\psi^4$  free energy in Eq. 1.18, and without magnetic field the CHC equation reduces to,

$$\frac{\partial}{\partial t} \psi(\mathbf{r}, t) = \nabla \cdot [D \nabla (-a(T_c - T)\psi + b\psi^3 - K \nabla^2 \psi) + \boldsymbol{\theta}(\mathbf{r}, t)]. \quad (1.22)$$

Also one can rescale the variables and obtain the dimensionless CHC equation

$$\frac{\partial}{\partial t} \psi(\mathbf{r}, t) = \nabla \cdot [\nabla (-\psi + \psi^3 - \nabla^2 \psi) + \boldsymbol{\theta}(\mathbf{r}, t)], \quad (1.23)$$

where  $\langle \boldsymbol{\theta}(\mathbf{r}, t) \rangle = 0$ ,  $\langle \theta_i(\mathbf{r}', t') \theta_j(\mathbf{r}'', t'') \rangle = 2\epsilon \delta_{ij} \delta(\mathbf{r}' - \mathbf{r}'') \delta(t' - t'')$  and  $\epsilon = \frac{k_B T b [a(T_c - T)]^{(d-4)/2}}{K^{d/2}}$ .

### 1.5.3 Correlation function and structure factor

During dynamical process domains form, and the system is characterized by a length scale. If the morphology of the domains statistically does not change with time, the correlation function  $C(\mathbf{r}, t)$  of the order parameter shows dynamical scaling, as expressed in the following

$$C(\mathbf{r}, t) = \frac{1}{V} \int d\mathbf{R} [\langle \psi(\mathbf{R}, t) \psi(\mathbf{R} + \mathbf{r}, t) \rangle - \langle \psi(\mathbf{R}, t) \rangle \langle \psi(\mathbf{R} + \mathbf{r}, t) \rangle] = g\left(\frac{r}{L(t)}\right), \quad (1.24)$$

where  $V$  is the volume of the system. Here the correlation function is averaged over different initial conditions and thermal fluctuations. This correlation function is a time dependent quantity, whereas  $g(r/L(t))$  is a time independent scaling function, where  $L(t)$  is the typical characteristic length of the domain at time  $t$ .

For non-conserved scalar order parameter, effective velocity of the domain wall should be equal to its curvature. For a domain of characteristic length  $L$ , the velocity of domain wall is  $v \sim \frac{dL(t)}{dt}$ , and the curvature of the domain  $K \sim 1/L(t)$ . Hence, the diffusive growth law for non-conserved scalar order parameter is  $L \sim t^{1/z}$ , where  $z = 2$  (called dynamical exponent). So far we have discussed non-conserved scalar order parameter. However, we may need n-components vector order parameter in many systems, like nematic liquid crystals [102].

For two components ( $n=2$ ) vector order parameter in 2D there is logarithmic correction in growth law  $L(t) \sim (t/\ln(t))^{1/2}$ .

For the conservative order parameter, the chemical potential  $\mu$  on the surface of a domain of size  $L(t)$  is defined by,  $\mu \sim \sigma/L(t)$ , where  $\sigma$  represents surface tension. Now, one can get the variation of the concentration current  $D|\nabla\mu| \sim D\sigma/L(t)^2$ , where  $D$  is diffusion constant. Hence, the growth of domain is obtained as  $dL(t)/dt \sim D\sigma/L(t)^2$  or  $L(t) \sim (D\sigma t)^{1/z}$  ( $z = 3$ ) [107].

We have discussed about the real-space correlation function for both non-conserved and conserved order-parameter, but in experiments, like neutron or light scattering experiments the measured quantity is the structure factor. The structure factor is defined by the Fourier transform of real space correlation function,  $S(\mathbf{k}, t) = \int d\mathbf{r} \exp(i\mathbf{k}\cdot\mathbf{r})C(\mathbf{r}, t)$ , where  $\mathbf{k}$  is the wave-vector of the scattered wave. Hence, the corresponding scaled dynamical structure factor is defined as,  $S(\mathbf{k}, t) = L(t)^d f(kL(t))$ , where the scaling function is obtained as,  $f(q) = \int d\mathbf{r} \exp(i\mathbf{q}\cdot\mathbf{r})g(r)$ . Therefore, to understand the morphology of the dynamical system one has to obtain the scaling functions  $g(r)$  or  $f(q)$ . Also near the interface, *i.e.*,  $kL(t) \rightarrow \infty$  the scaled structure factor follows power law  $f(kL(t)) \sim (kL(t))^{-(d+n)}$  for  $n$ -components order parameter in  $d$ -dimensions. This is known as generalized Porod's law.

#### 1.5.4 Coarsening in active systems

The general features of the active systems are different from their equilibrium counterpart because the systems are settling towards a non-equilibrium steady state. Dey *et al.* [108] studied the coarsening for polar particles for microscopic Vicsek like models [57, 67, 75, 91, 109]. They find that these active models show non-Porod behavior. Similar results also predicted for active nematic [110] and active polar [100] systems. Toner and Tu predicted the growth law for coarse-grained density  $L_\rho(\mathbf{r}, t) \sim t^{5/6}$  in polar systems [20, 111].

The ordering kinetics of phase separation of the ABPs is governed by conserved growth model called as active model B [112]. Wittkowski *et al.* find that the activity has modest effect on the kinetics [112]. In spite of all these studies, the detail understanding about growth

phenomenon of active system is still lacking. In this thesis we have studied the phase ordering kinetics of ABPs and effect of different kinds of noises.

## 1.6 OBJECTIVE AND ORGANISATION OF THIS THESIS

In the previous sections, we have discussed about different classes of the active matter systems depending on the conservation laws in the system and symmetry. We have discussed the general framework to study these active systems and compared with their equilibrium counterparts. We have mentioned about the collective behavior and bulk properties, like order-disorder phase transition, long-range ordering, *etc.*, of the clean systems [19, 21, 57, 75, 76]. We have mentioned the bulk properties of these systems in the presence of different kinds of heterogeneity which is an inevitable fact in real systems [77–86]. We have also discussed about the ordering kinetics in the polar active systems. With these basic understanding about active matter systems, we have unveiled some further aspects of the polar SPPs and ABPs that have been arranged in the following chapters. In chapter 2, we consider a collection of polar SPPs confined in a narrow channel and find that there is formation of moving rolls. Next, in chapter 3, we have studied the dynamics of an ABP on a substrate with periodic array of obstacles and in corrugated channels. We find induced directionality in the ABP motion on the substrate with periodic obstacle arrays, and a super-diffusive dynamics of ABP in a corrugated channel. However, the dynamics of the ABP is diffusive in a channel with flat boundary. Nature of the order-disorder phase transition in the polar systems is still an area of debate. In chapter 4, we have studied the nature of the order-disorder transition of a collection of polar SPPs. We find that nature of the transition can be tuned by changing the system parameters. We also note that large density phase separation is responsible for discontinuous transition in polar SPPs.

The polar SPPs moving with same self-propulsion speed is a key assumption in the Vicsek model, but in real systems there is a fluctuation in the self-propulsion speed in a collection of SPPs. In chapter 5, we have studied the role of speed inhomogeneity in a collection of polar SPPs. As we discussed in Sec. 1.2.2, the ABPs show a motility induced phase separation

without any alignment interaction. We can compare the kinetics of ABPs to a binary mixture with an activity term. In chapter 6, we have studied the ordering kinetics of a collection of ABPs and role of different types of noises in coarse-grained equations. At last, the thesis is concluded with significant remarks in chapter 7.

---

## BOUNDARY INDUCED CONVECTION IN A COLLECTION OF POLAR SELF-PROPELLED PARTICLES

---

### 2.1 INTRODUCTION

Collective behaviour of active particles are extensively studied in [19–22], *but* most biological systems are confined to thin geometry [113]. Confinement and boundary plays an important role in variety of problems in biology [113], sheared systems [41, 42] and other places like in fluid dynamics. One classic example include Rayleigh-Bénard (RB) convection in fluid [114]. In these confined systems, the effect of boundaries is very important. In this chapter, we will discuss about the collective behavior of polar SPPs confined in a narrow channel. <sup>1</sup>

Boundary can play very important role in the collection of self-propelled particles. It can induce many interesting phenomena like, in many cases, boundary can induce spontaneous flow inside the channel [115, 116]. We write the phenomenological equations of motion for local density and polarisation order parameter for the collection of polar self-propelled particles Eqs. 2.1 and 2.2. Self-propelled speed (SPS) of the particle introduces a non-equilibrium coupling between density and polarisation. For zero SPS both density and polarisation are decoupled. We solve these equations in the confined geometry shown in Fig. 2.2. At the two boundaries of the channel orientation of rods are antiparallel, which produces a gradient along the confinement direction. Diffusion tries to make them parallel. Hence the competition between above two create *rolls* of orientation along the long-axis of the channel. For zero SPS these rolls are static and density inside the channel is homogeneous. For non-zero SPS

---

<sup>1</sup> The work reported here is based on the paper “Boundary induced convection in a collection of polar self-propelled particles”, Shradha Mishra and Sudipta Pattanayak, *Physica A* 477, 128-135 (2017).

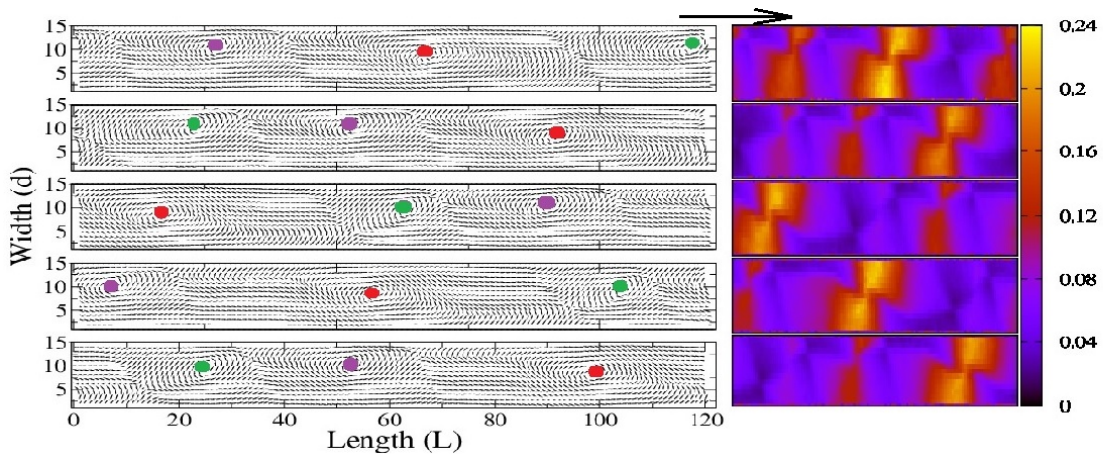


Figure 2.1: (left) Vector plot of local polarisation and (right) density inside the channel for activity  $R_A = 0.67$ . Different plots are snapshot of polarisation and density at different times. (left) local polarisation shows vortex type periodic pattern (*rolls*) along the long axis of the channel. Different color dots on periodic *rolls* represent distinct vortex. Density also shows periodic pattern. Bright regions are high density and dark regions are low density. Top to bottom figures are from small to large time. With time periodic *rolls* for both density and local polarisation moves from one end to other end of the channel. Arrow on the top of the figure represent direction of motion of periodic pattern. This direction is spontaneously chosen from two equally possible direction in the system.

both density and polarisation are coupled and such coupling produces moving rolls.

In Fig. 2.1, we show the (left) vector plot orientation and (right) density of particles inside the channel for SPS  $v_0 = 1.5$  at different times. We find inhomogeneous moving pattern of orientation and density along the long axis of the channel Fig. 2.1(top to bottom). Arrow indicate the direction of motion.

In this chapter, section 2.2 discusses the model in detail. Here we also write the hydrodynamic equations of motion for density and polarisation. Section 2.3 discusses the numerical details for solving these equations. We discuss our results in section 2.4 and finally conclude with discussion and future aspect of this study in section 2.5.

## 2.2 MODEL

We consider a collection of self-propelled particles of length  $l$  confined to a two-dimensional channel whose thickness  $d$  is very small compare to its long axis  $L$ . We fix the length of the channel  $L$  and vary the width of the channel  $d \ll L$ . Orientation at the lower boundary

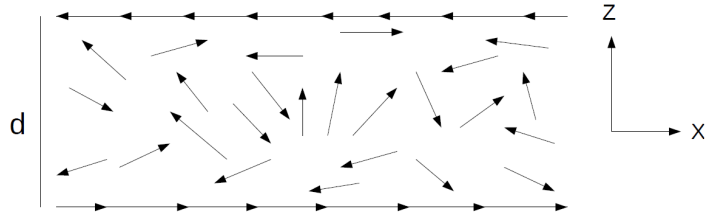


Figure 2.2: Geometry of confined channel and orientation of particle at the two confined boundaries. x-direction is chosen along the long axis of the channel and z-direction is the confinement direction. Periodic boundary condition is used along the long axis of the channel. Orientation is parallel to +x-direction at bottom boundary ( $z=1$ ) and parallel to -x-direction at top boundary ( $z=d$ ). Magnitude of polarisation  $|P| = 1$  is fixed at two boundaries and density is maintained to mean value  $\rho_0 = 0.1$ .

is parallel to horizontal axis and at the upper boundary it is antiparallel and magnitude of polarisation fixed at two boundaries. We also maintain mean density at two confined boundaries to avoid accumulation of particles at two boundaries. Periodic boundary condition is used for both density and polarisation along the long axis of the channel. Geometry of confined channel and orientation of particles at the two boundaries is shown in Fig. 2.2.

### 2.2.1 Hydrodynamic equations of motion

Dynamics of the system is described by the equations of motion for hydrodynamic variables for the collection of polar self-propelled particles. We write the phenomenological coupled hydrodynamic equations of motion for density  $\rho$ , because total number of particles are conserved and polarisation  $P$ , which is an orientation order parameter, is a broken symmetry variable in the ordered state. We write the minimum order terms allowed by symmetry. Two equations are

$$\frac{\partial \rho}{\partial t} = -v_0 \nabla \cdot (\rho \mathbf{P}) + D_\rho \nabla^2 \rho \quad (2.1)$$

and

$$\frac{\partial \mathbf{P}}{\partial t} = -D_R (-\alpha_0 + \alpha_1 |P|^2) \mathbf{P} - \frac{v_0}{2\rho_0} \nabla \rho + D_P \nabla^2 \mathbf{P} \quad (2.2)$$

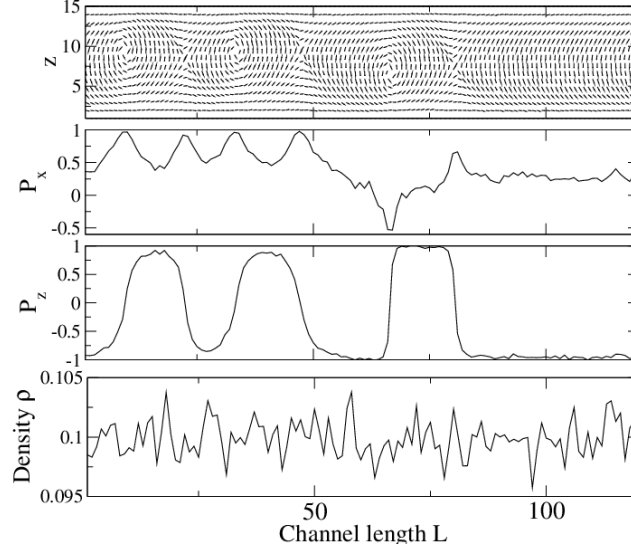


Figure 2.3: For zero activity  $R_A = 0$  or SPS  $v_0 = 0.0$ : (a) vector plot of orientation field, which shown periodic vortex type pattern *rolls*. (b) x-component of polarisation  $P_x$  (c) z-component of polarisation  $P_z$  and (d) density  $\rho(x)$ : along the long axis of the channel, averaged over the z-direction.

Density equation 2.1 is a continuity equation because total number of particles are conserved. Right hand side of Eq. 2.1 can be written as a divergence of a current  $\mathbf{J}$  which has two parts,  $\mathbf{J} = \mathbf{J}_a + \mathbf{J}_p$ , where  $\mathbf{J}_p \propto \nabla \rho$  is proportional to gradient in density we call it “passive current” and  $\mathbf{J}_a \propto v_0 \rho \mathbf{P}$  is proportional to polarisation vector  $\mathbf{P}$  and self-propelled speed  $v_0$  and we call it as “active current”. For zero SPS  $v_0 = 0$  or polarisation  $\mathbf{P} = 0$  active current is zero. The order parameter equation 2.2 contains (i) mean field order disorder terms  $\alpha_0$  and  $\alpha_1$ , (ii) pressure term present because of density fluctuation and (iii) diffusion in polarisation  $D_p$ .  $\alpha_0$  and  $\alpha_1$  are positive and determine the mean field value of polarisation  $\mathbf{P}$  in the bulk  $|\mathbf{P}| = \sqrt{\frac{\alpha_0}{\alpha_1}}$ . We choose  $\alpha_0 = \alpha_1 = 1.0$ , such choice of  $\alpha_0$  and  $\alpha_1$  prefers homogeneous polarised steady state  $|\mathbf{P}| = 1.0$  in the bulk.  $\nabla \rho$  is the pressure term and proportional to the self-propelled speed  $v_0$  of the particle.  $D_p$  term is written in the limit of equal elastic constant approximation for splay and bend deformations in two dimensions and  $D_R$  is the rotational diffusion.

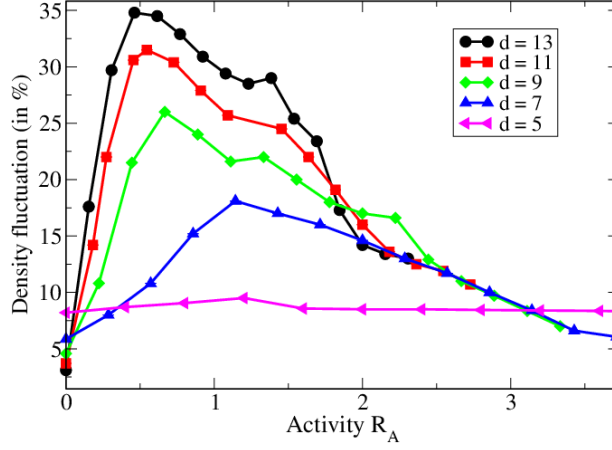


Figure 2.4: Plot of percentage density fluctuation  $\% \Delta N$  vs. activity  $R_A$  for different width  $d$  of the channel.  $\Delta N$  shows non monotonic behaviour as we increase activity  $R_A$ . Density inhomogeneity increases as we increase width of the channel.

We rescale all lengths by particle length  $l$  (which we choose 1) and time by rotational diffusion time  $D_R^{-1}$ .

$$\begin{aligned} r' &= r/l; \\ t' &= tD_R. \end{aligned} \tag{2.3}$$

and write the dimensionless equations of motion for density

$$\frac{\partial \rho}{\partial t} = -R_A \nabla \cdot (\rho \mathbf{P}) + \bar{D}_\rho \nabla^2 \rho \tag{2.4}$$

and polarisation order parameter

$$\frac{\partial \mathbf{P}}{\partial t} = (\alpha_0 - \alpha_1 |P|^2) \mathbf{P} - \frac{R_A}{2\rho_0} \nabla \rho + \bar{D}_P \nabla^2 \mathbf{P}. \tag{2.5}$$

where

$$R_A = \frac{v_0}{lD_R} \tag{2.6}$$

is the dimensionless activity. It is a ratio between the self-propelled speed  $v_0$  and the rotational diffusion  $D_R$ . Hence we can increase activity either by increasing speed  $v_0$  or having small  $D_R$ . We can also define dimensionless diffusions.

$$\bar{D}_{\rho,P} = \frac{D_{\rho,P}}{l^2 D_R}. \quad (2.7)$$

which is again ratio between bulk diffusion and rotational diffusion.

### 2.3 NUMERICAL STUDY

We numerically solve the coupled hydrodynamic equations of motion for density and polarisation order parameter. We go beyond mean field and add Gaussian random white noise to the density

$$\frac{\partial \rho}{\partial t} = -R_A \nabla \cdot (\rho \mathbf{P}) + \bar{D}_\rho \nabla^2 \rho + \nabla \cdot \mathbf{f}_\rho(\mathbf{r}, t) \quad (2.8)$$

and the order parameter

$$\frac{\partial \mathbf{P}}{\partial t} = -(-\alpha_0 + \alpha_1 |P|^2) \mathbf{P} - \frac{R_A}{2\rho_0} \nabla \rho + D_P \nabla^2 \mathbf{P} + \mathbf{f}_P(\mathbf{r}, t) \quad (2.9)$$

random forces are chosen to have zero mean and correlations

$$\langle f_\rho^i(\mathbf{r}, t) f_\rho^j(\mathbf{r}', t') \rangle = 2\Delta_\rho \delta_{ij} \delta(\mathbf{r} - \mathbf{r}') \delta(t - t') \quad (2.10)$$

and

$$\langle f_P^i(\mathbf{r}, t) f_P^j(\mathbf{r}', t') \rangle = 2\Delta_P \delta_{ij} \delta(\mathbf{r} - \mathbf{r}') \delta(t - t') \quad (2.11)$$

where  $\Delta_\rho$  and  $\Delta_P$  are dimensionless noise strengths. Numerical study is done for fix noise strength  $\Delta_\rho = \Delta_P = 0.05$ . We fix  $D_R = 0.1$ , mean density  $\rho_0 = 0.1$ , diffusivities  $D_\rho = D_P = 1.0$ . Hence activity  $R_A$  is varied by changing the SPS  $v_0$ . Typical diffusive length scale in the system  $\delta = \sqrt{\frac{D_P}{D_R}}$  and for the above specific choice of parameters  $\delta = \sqrt{10} \simeq 3.5$ . Hence, we

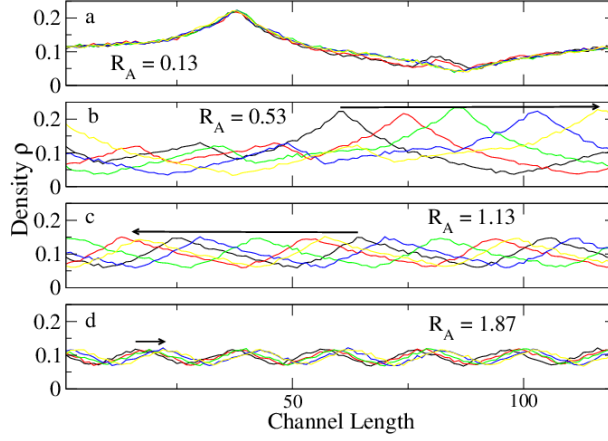


Figure 2.5: Plot of one dimensional density along the long axis of the channel for different self-propelled speeds (a) For small  $R_A = 0.13$ , density shows inhomogeneous structure but with time this inhomogeneous structure does not move much from its position. (b)-(c) For  $R_A = 0.53$  and  $1.13$ , pattern of high and low density move along the long axis of the channel. Patterns move with different speeds at different self-propelled speeds. (d) Again for large  $R_A = 1.87$ , pattern does not move much with time. Density inhomogeneity is small compared to that at intermediate  $R_A$ . Length of the arrow denotes the shift in the density pattern with time.

choose the lower limit on  $d > \delta$  such that  $d$  is not much bigger than  $\delta$  and upper limit such that effect of confinement is important. Hence  $d$  is varied from 5 to 15. We fixed the length of the channel and SPS is changed from from zero to large values.

We solve these PDE's 2.8 and 2.9 using Euler method for numerical differentiation on a grid  $\Delta x = 1.0$  and  $\Delta t = 0.1$  (we have checked that numerical scheme is convergent and stable for the above choice). Inside the channel we start from initially random order parameter and homogeneous density  $\rho = \rho_0 = 0.1 \pm 0.01$ , At the two boundaries the magnitude of polarisation is fixed to  $P_0 = 1.0$  and antiparallel orientation such that  $P_x(z = 1) = 1.0$ ,  $P_z(z = 1) = 0.0$  and  $P_x(z = d) = -1.0$ ,  $P_z(z = d) = 0.0$  and density is maintained to mean density  $\rho(z = 1) = \rho(z = d) = \rho_0$ . Periodic boundary condition is used along the long axis of the channel.

## 2.4 RESULTS

We divide our results in two parts. First we discuss what happens when activity is turned off, and then we discuss the effect of activity.

### 2.4.1 Zero activity $R_A = 0$ or SPS $v_0 = 0.0$

For zero activity  $R_A = 0.0$  density and order parameter are decoupled Eqs. 2.8 and 2.9. Steady state solution for density is homogeneous density  $\rho = \rho_0$ . Orientation order parameter shows formation of *rolls* along the long axis of the channel. These rolls are formed because of competition between antiparallel boundary condition which produces a gradient in orientation and diffusion term which tries to make them uniform. Mechanism is similar to *Rayleigh-Bénard convection* in fluid dynamics, where competition between temperature gradient and gravity produces convective rolls. In Fig. 2.3 (a) we plot the vector plot of orientation field for zero self-propelled speed  $v_0 = 0.0$ . We find formation of periodic pattern or *rolls* along the long axis of the channel. In Fig. 2.3(b) and (c) we also plot the  $x$  and  $z$  component of orientation field along the long axis of the channel which confirms the above periodic structure. In Fig. 2.3 (d) we plot the density along the long axis of the channel, which remains homogeneous inside the channel.

### 2.4.2 Non-zero activity or SPS $v_0 \neq 0.0$

When we switch on the activity parameter  $R_A$ , hydrodynamic equations of motion for density and polarisation order parameter Eqs. 2.8 and 2.9 are coupled. Non-zero activity introduces an active current  $\mathbf{J}_a \propto v_0 \mathbf{P} \rho$  which is proportional to the SPS  $v_0$  and local polarisation  $\mathbf{P}$  (discussed in detail in section 2.2). This active current produces density inhomogeneity and hence enhanced pressure in local polarisation, which is again proportional to SPS  $v_0$  or activity parameter  $R_A$  as shown in Eq. 2.8 and 2.9.

#### 2.4.2.1 Density fluctuation

We first calculate the density inhomogeneity for different width of the channel. Density inhomogeneity increases as we increase the width of the channel. In figure 2.4 we plot the percentage density fluctuation  $\% \Delta \rho$  along the long axis of the channel averaged over transverse direction for five different widths  $d = 5, 7, 9, 11, 13$  as a function of activity parameter  $R_A$ . For very small width  $d = 5$ , density fluctuation is small (*strong confinement*). For width of the channel  $d \geq 7$ , density fluctuation shows non-monotonic behaviour as a function of activity  $R_A$ . As we change  $R_A$  from zero, first increases very sharply with a peak at some finite  $R_A$  and then decreases slowly for larger activity. Peak position shift towards smaller activity as we increase width of the channel. It changes from  $R_A = 1.13$  to  $0.4$  as we change the width from  $d = 7$  to  $d = 13$ . Hence confinement suppresses the large density fluctuation present in general in self-propelled particles in bulk. Suppression of density fluctuation because of confinement is also found previously in the study of sheared suspension of Self-propelled particles [41, 42].

Non-monotonic nature of curve gives a finite range of activity, where fluctuations are large. For very small activity coupling of density to background periodic *rolls* is small and hence small density fluctuation. As we increase activity, active contribution to density current increases: which is proportional to the local order parameter  $\mathbf{P}$  and hence background periodic *rolls* of polarisation order parameter. Activity plays two role here, (i) it produces an active density current proportional to local polarisation. Since such active current creates density inhomogeneity hence (ii) it creates pressure in local polarisation. Hence for very large activity density current will be large but at the same time pressure will also increase and it will destroy the background periodic *rolls*. Hence small active current (because  $\mathbf{J}_a \propto \mathbf{P}$ ), hence small density inhomogeneity.

#### 2.4.2.2 Travelling rolls

Even for zero activity as discussed in section 2.4.1, antiparallel boundary conditions at the two confined boundaries creates *rolls* of orientation field. For the range of activity when density fluctuation is large, these *rolls* move from one end to another end of the channel. We call

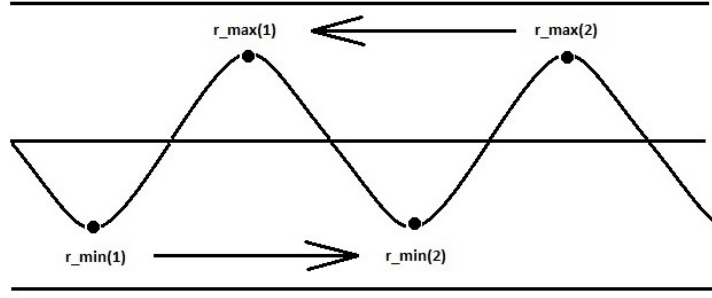


Figure 2.6: Cartoon of periodic pattern of density for finite self-propelled speed  $v_0$  or activity  $R_A$ .  $r_{max}[i]$  shows the position of  $i^{th}$  maxima and  $r_{min}[i]$  the position of the  $i^{th}$  minima of density. The two arrows denote the direction of alignment at the two boundaries. We record the position of maxima and minima at different times.

them as *travelling rolls*: where density and orientation both shows periodic pattern (please see fig. 2.1 for one such activity  $R_A = 0.67$ ). In Fig. 2.5 we plot density for width of the channel  $d = 13$ , along the long axis of the channel averaged over transverse direction. We calculate density for four different times (with equal time difference) and for four different activity strength  $R_A = 0.13, 0.53, 1.13$  and  $1.87$ . For all activities density shows inhomogeneous periodic pattern. Density inhomogeneity shows variation for different activity. For very small activity  $R_A = 0.13$ , density shows small inhomogeneity and remains static with time. For activity  $R_A = 0.53$ , density is periodic as well as inhomogeneous. These periodic pattern move with time. In Fig. 2.5(b) we draw a horizontal arrow to denote the motion of periodic pattern with time. Larger the arrow faster the pattern move. Direction of arrow shows the direction of motion of periodic pattern. This direction is spontaneously chosen from two equal possible directions in the system. For activity  $R_A = 1.13$  we get the similar result as for  $R_A = 0.53$  but density inhomogeneity is weaker. For activity  $R_A = 1.87$ , density is periodic but inhomogeneity is even more weak and very small shift in peak position as a function of time (as shown by small horizontal arrow in Fig. 2.5(d)). Hence travelling periodic pattern and density inhomogeneity are coupled and larger density inhomogeneity creates faster moving rolls from one end to other end of the channel. For very large activity, density coupling is strong enough such that it destroys the background periodic pattern of orientation and hence no travelling rolls.

### 2.4.2.3 Mean square displacement

We further characterise properties of *travelling rolls* assuming periodic density pattern as shown in Fig. 2.5. Cartoon picture of maxima and minima of periodic density profile for one such realization is shown in Fig. 2.6. We track the position of maxima and minima of periodic density pattern. Position of each maxima and minima we model as position of independent particles moving in one dimension. Hence each maxima and minima represent one particle and we save the position of maxima and minima or particles position with time. We calculate the square displacement of such positions and take average over all maximas and minimas and many initial realisations. Hence mean square displacement of is defined as

$$\Delta(t) = \frac{1}{N_e} \sum_{n_e=1}^{N_e} \frac{1}{2} \frac{1}{N_i} \sum_{i=1}^{N_i} [ |r_{max}^{n_e}(i, t_0) - r_{max}^{n_e}(i, t + t_0)|^2 + |r_{min}^{n_e}(i, t_0) - r_{min}^{n_e}(i, t + t_0)|^2 ] \quad (2.12)$$

where  $r_{max/min}^{n_e}(i, t)$  is the position of maxima/minima of the  $i^{th}$  periodic profile at time  $t$  for  $n_e^{th}$  realisation (as shown in Fig. 2.6). Averaging is done over all periodic positions  $i = 1, N_i$  and number of realisations  $n_e = 1, N_e$ . For our calculation we used total number of realisation  $N_e = 20$ .

When travelling rolls form as discussed in previous section 2.4.2.2, then  $\Delta(t)$  is proportional to  $t^2$ . In Fig. 2.7(a) we plot MSD,  $\Delta(t)$  for different activity  $R_A$  for channel of width  $d = 13$ . For zero activity density is homogeneous and no periodic pattern and  $\Delta(t) \simeq t$  (*diffusive*). As we increase activity  $R_A = 0.13$ , MSD  $\Delta(t)$  is *subdiffusion* where  $\Delta(t) \simeq t^\alpha$  and  $\alpha < 1$ . Subdiffusive behaviour shows the arrest of density in the center of the periodic *rolls*, which acts like a disorder site (with small polarisation). Similar arrest of density in the presence of quenched disorder field is found in recent study of [80]. But in our model disorder site or center of the *roll* moves for sufficient large activity. For activity  $R_A \geq 0.67$ , MSD shows two regimes with initial Subdiffusive with  $\alpha < 1$  to later *travelling* motion with  $\alpha \simeq 2$ . Hence for  $R_A \geq 0.67$ , density remains arrested for some time and then travelling rolls sets in. As we further increase activity  $R_A = 0.67$  and 1.33 we find initial Subdiffusive with  $\alpha < 1$  and the later travelling motion with  $\alpha = 2$ . Time spent in arrested state decreases as we increase activity. For large activity  $R_A \geq 1.67$ ,  $\Delta(t) \simeq t^\alpha$  for very small time and then switches to

transient faster dynamics and then saturates to diffusive  $\Delta(t) \simeq t$  for large time.

In Fig. 2.7(b) we also plot the diffusivity defined as

$$D(t) = \frac{1}{2t} \Delta(t) \quad (2.13)$$

$D(t)$  remain flat for zero activity, hence *diffusion*. For small activity  $R_A = 0.13$  it decrease with time and shows arrested subdiffusion. For intermediate activities  $R_A = 0.67$  to  $1.33$ ,  $D(t)$  shows initial subdiffusion and later travelling motion with  $D(t) \simeq t$ . For very large activity  $R_A \geq 1.67$  initial  $D(t)$  decreases with time then faster growth to diffusive regime with constant  $D(t)$  for very long time.

We further explain the dynamics of particle inside the channel as we vary the activity  $R_A$ . For zero activity density and orientation are decoupled hence we expect normal diffusive motion for the particle. As we have discussed before antiparallel boundary condition at the two confined boundaries creates periodic *rolls* along the long axis of the channel. As we switch on activity density is coupled to periodic orientation field. For very small activity coupling particles are trapped in periodic orientation. center of periodic pattern acts as quenched disorder site. For intermediate activity coupling is strong and large density inhomogeneity as shown in Fig. 2.4. Hence for initial transient time particles are trapped to periodic pattern of orientation and later active current sets the travelling *rolls*. Such initial subdiffusion to propagating motion is very common for particle moving in periodic structure. When particle move in a periodic background it spent some of its time in trapped phase and then start propagation. Similar subdiffusion to propagation is found for the particle moving in periodic media [117]. For very large activity coupling is very strong and it destroys the background periodic pattern of orientation and hence diffusive behaviour at late time.

## 2.5 DISCUSSION

In our present work we write the phenomenological hydrodynamics equations of motion for density and local polarisation order parameter Eq. 2.8 and 2.9 for the collection of self-propelled particles. We solve these equation in the confined channel of width  $d \ll L$  very

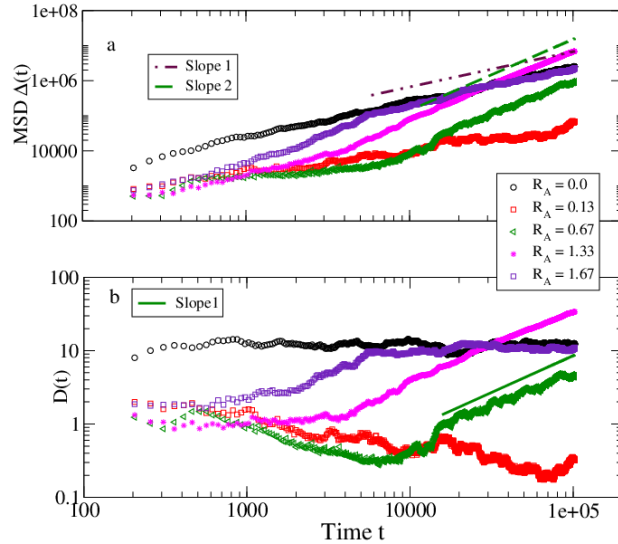


Figure 2.7: Plot of (a) mean square displacement (MSD)  $\Delta(t)$  and (b) corresponding diffusion coefficient  $D(t) = \Delta(t)/(2t)$  vs. time  $t$ , of position of high and low density peak position average over many realisation. Different curves are for different activity ranging from  $R_A = 0.0$ , large values  $R_A = 1.67$ . For small  $R_A \leq 0.13$ ,  $\Delta(t) \simeq t$  (a) and density shows diffusive behaviour hence  $D(t)$  approaches constant value (b) at large time. For intermediate  $0.67 \leq R_A < 1.33$ ,  $\Delta(t) \simeq t^2$  and travelling periodic pattern (a) and hence  $D(t) \simeq t$  (b), and for large  $R_A \geq 1.67$ , again diffusive and hence  $\Delta(t) \simeq t$  (a) and  $D(t)$  approaches constant value (b). Two Straight lines in (a) are line of slope 1 and 2. and in (b) straight line is of slope 1.

small compare to the long axis of the channel. We impose an antiparallel boundary conditions at the two confinement boundaries and maintain the density at its mean value and the magnitude of polarisation constant. Such a geometry is important because it mimics the shear. First we solved equations(1,2), for zero activity. Antiparallel boundary conditions impose a gradient of orientation along the confinement direction and diffusion tries to make them parallel. Hence there is a competition between these two terms and we find periodic patterns of the orientation field along the long axis of the channel Fig. 2.3(a). And, since for zero activity density is not coupled to the orientation field, it remains uniform.

Non-zero activity, turn on a contribution of active current, which is proportional to the local polarisation inside the channel. Such active currents make the inhomogeneous density inside the channel. Density inhomogeneity increases as we increase the width of the channel. For fixed channel width, as we increase activity initially density inhomogeneity increases with activity  $R_A$  Fig. 2.4 and then decrease for large activity  $R_A$ . For fixed channel width, for the range of activity when density inhomogeneity is large, density periodic pattern sets in and

start moving from one end to other end of the channel. Real space image of moving periodic orientation *rolls* and density profile for fixed channel width and activity is shown in Fig. 2.1 for different times.

Travelling periodic rolls we observe here is very similar to Rayleigh-Bénard convection in fluids. Orientation plays the role of temperature gradient and diffusion is like gravity which acts opposite to gradient. A competition between these two produces periodic rolls and in the presence of activity these rolls move from one end to other end of the channel.

It would be interesting to study other kinds of boundary condition on the flow properties of active particles inside the channel. For example recent study of [118], where boundary induces accumulation of particles. This phenomena where boundary induces spontaneous flow in confined channel can give some insight of transport of active fluid in biology [119].

---

## ENHANCED DYNAMICS OF ACTIVE BROWNIAN PARTICLES IN PERIODIC OBSTACLE ARRAYS AND CORRUGATED CHANNELS

---

### 3.1 INTRODUCTION

As we mentioned in previous Sec. 1.3, in addition to the extensive study of active systems in clean environments [19, 21, 52, 57, 63, 75, 76, 97], recently people have started to look for their bulk properties in heterogeneous medium [77–86]. In this chapter we have studied the single particle dynamics of ABP on a 2D substrate with periodic obstacle arrays, and in corrugated channels. <sup>1</sup> Active Brownian particles (ABPs) [68] are one kind of SPPs where the particles do not have any mutual alignment interaction, and they exhibit many interesting phenomena like motility induced phase separation [26, 47, 68, 73]. In recent study, Reichhardt *et al.* examine a two-dimensional system of run-and-tumble active matter disks that can exhibit motility induced phase separation interacting with a periodic quasi-one-dimensional traveling-wave substrate. Authors note that the collective clustering of run-and-tumble disks could be an effective method for forming an emergent object that can move against gradients or drifts even when individual disks on average move with the drift [120]. In another study, Reichhardt *et al.* consider ballistic active disks driven through a random obstacle array. Formation of a pinned or clogged state occurs at much lower obstacle densities for the active disks than for passive disks [121]. Very recently, the dynamics of the ABP is shown to be sub-diffusive in the presence of obstacles modeled as random Lorentz gas for density of obstacles close to

---

<sup>1</sup> The work reported here is based on the paper “Enhanced dynamics of active Brownian particles in periodic obstacle arrays and corrugated channels”, Sudipta Pattanayak, Rakesh Das, Manoranjan Kumar and Shradha Mishra, *Eur. Phys. J. E* 42, 62 (2019).

percolation threshold [98]. These ABPs are shown to attain their long-time dynamics faster than the passive (Brownian) particles, because of their persistent motion [98]. In contrast, when obstacles are arranged periodically, it is found that the persistent length of the active particle increases [122]. Choudhury *et al.*, consider chemically boosted self-propelled Janus colloids moving atop a two-dimensional crystalline surface. The authors find that the dynamics of the self-propelled colloid reflects a competition between hindered diffusion due to the periodic surface and enhanced diffusion due to active motion [123]. Hence, the nature of the heterogeneous environment modifies the dynamics of the active particles.

The dynamics of the active particle is not only modified in heterogeneous substrates, but also can be modified using confined channel. Boundary of the confined wall plays an important role in the motion of active particles [88–90, 124]. Recently, Dey *et al.*, showed that the confinement can enhance the average rate of binding of the motor-cargo complexes to the microtubule, which leads to an enhancement in the average velocity [88]. Also the asymmetric channel corrugation induces a net-flux in the motion of microswimmers along the channel, the strength and direction of which strongly depends on the swimmer type [89]. Furthermore, a non-zero average drift can be induced in ABP using potential modulation between two directions in a 2D periodic corrugated channel [90].

Motivated by the fact that the arrangement of the obstacles, and different kind of confined channel can modify the dynamics of the active particles, in the present work we ask the question: How the dynamics of the active particle varies with its activity, and density of the obstacles arranged periodically (i) on a two-dimensional substrate, (ii) along the boundary of a quasi-one-dimensional channel.

To answer the first question, we numerically study the dynamics of an ABP on a 2D substrate with periodically arranged obstacles. The ABP shows a cross-over from its initial super-diffusive to diffusive dynamics, and such a cross-over is an intrinsic feature of the active particles [92, 125]. We find that, due to steric interaction between the ABP and obstacles, the cross-over time of the ABP increases with its self-propulsion speed. Furthermore, we note that in a dense obstacle environment the ABP performs more directed motion. In the later part of this paper, the dynamics of the ABP in a quasi-one-dimensional corrugated channel comprised periodically arrayed obstacles is studied. We find that the corrugated

channel governs a super-diffusive dynamics of the ABP along the channel without any external drive. Also the transport is independent of the shape of the corrugated boundary, and it only depends on packing fraction of the obstacles in the channel. However, we find the flat boundary does not encourage the super-diffusive motion.

This chapter is organized as follows. In section 3.2 we introduce the microscopic rule based model for the ABP in periodic geometries. The results of the numerical simulation of 2D substrate with periodic obstacles and corrugated channel are given in section 3.3.1 and 3.3.2, respectively. Finally in section 3.4, we discuss our results and future prospect of our study.

## 3.2 MODEL

We consider a circular-disk shaped active Brownian particle of radius  $R_p$  placed in a periodic obstacle environment. Its dynamics is studied for two models; (i) in model I, we consider a 2D  $L \times L$  square lattice, where circular-disk shaped obstacles of radius  $R_o$  are placed periodically at the vertices, and (ii) in model II, we consider a quasi-one-dimensional corrugated channel comprised periodically arranged circular or elliptical obstacles at the boundary of the channel. The semi-major and the semi-minor axes of the elliptical obstacles are designated by  $\max(a', b')$  and  $\min(a', b')$ , respectively.  $a'$  and  $b'$  are always chosen along the  $x$  and  $y$ -axes, respectively, as shown in Fig. 3.1. For corrugated channel with circular obstacles  $a' = b'$ . Let us represent the position vector of the centre of the ABP by  $\mathbf{r}(t)$  at time  $t$ . The ABP moves along its orientation defined by a unit vector  $\mathbf{e}(t)$  in the  $x$ - $y$  plane. The dynamics of the ABP is governed by over-damped Langevin equation

$$\frac{d\mathbf{r}(t)}{dt} = v_0\mathbf{e}(t) + \mu \sum_i \mathbf{F}_0^i, \quad (3.1)$$

$$\frac{d\mathbf{e}(t)}{dt} = \sqrt{2D^R}\boldsymbol{\eta}^R(t) \times \mathbf{e}(t), \quad (3.2)$$

The first term on the right-hand-side (RHS) of Eq. 3.1 is due to the activity of the ABP, and its self-propulsion speed is  $v_0$ . The second term represents steric force acting on the ABP due to its neighboring obstacles, and it is tuned by a parameter  $\mu$ , which is 0 for the obstacle-free

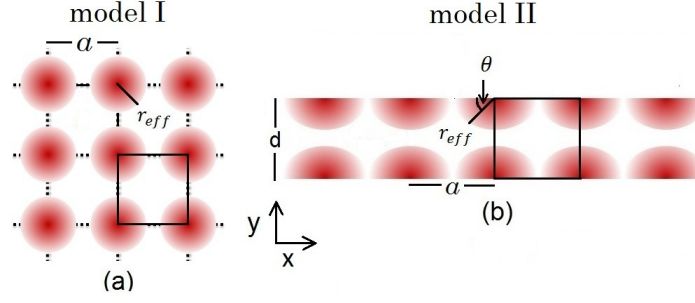


Figure 3.1: (a) The schematic picture of a square lattice with obstacles at its vertices. Centre to centre distance between obstacles  $a = 1.0$ . The packing fraction of the lattice is varied from  $\Phi = 0.125$  (obstacle free substrate) to  $\Phi = 0.39$ . (b) The schematic picture of a quasi-one-dimensional corrugated channel comprised periodically arrayed circular / elliptical obstacles. The periodicity  $a$ , and width of the channel  $d$  are shown.  $r_{eff}$  (defined in the text) is shown. The  $\Phi$  of the channel is varied from  $\Phi = 0.10$  to  $0.60$  by changing  $d$  or  $a$ . Boxes show unit cell for both cases.  $x$  and  $y$  directions for both model are shown.

substrate and 1 for all other cases. We consider  $F_0 = -\nabla V$ , where the steric interaction is incorporated by the *Weeks-Chandler-Anderson* potential defined as

$$\begin{aligned}
 V &= 4\epsilon \left[ \left( \frac{\sigma}{|\mathbf{r} - \mathbf{r}_o|} \right)^{12} - \left( \frac{\sigma}{|\mathbf{r} - \mathbf{r}_o|} \right)^6 \right] + \epsilon, & \text{for } |\mathbf{r} - \mathbf{r}_o| < r_{eff}, \\
 &= 0, & \text{for } |\mathbf{r} - \mathbf{r}_o| \geq r_{eff}.
 \end{aligned} \tag{3.3}$$

Here  $\mathbf{r}_o$  represents position vector of the centre of a neighboring obstacle. We treat the ABP as a point particle in our simulation, and its size is taken care by an effective radius  $r_{eff}$  of the obstacles. While in model I,  $r_{eff} = R_p + R_o$ , in model II,  $r_{eff} = R_p + a'b' / \sqrt{a'^2 \sin^2 \theta + b'^2 \cos^2 \theta}$ , where  $\theta$  is the angle of  $\mathbf{r} - \mathbf{r}_o$  with respect to the  $x$ -axis. We consider  $\epsilon = 1$ , and the parameter  $\sigma = r_{eff} / (2^{1/6})$ .

The rate of change of the orientation  $\mathbf{e}(t)$  of the ABP is given by Eq. 3.2.  $D^R$  represents the rotational diffusion constant, and  $\boldsymbol{\eta}^R = \eta_z^R \mathbf{e}_z$  is the stochastic torque with zero mean and Gaussian white noise correlations, *i.e.*,

$$\langle \boldsymbol{\eta}^R(t) \rangle = 0, \tag{3.4}$$

$$\langle \boldsymbol{\eta}^R(t_1) \otimes \boldsymbol{\eta}^R(t_2) \rangle = \mathbf{1} \delta(t_1 - t_2). \tag{3.5}$$

Note that the stochastic torque always points out of the substrate, *i.e.*, along the  $z$ -axis.

The schematic of the model I and II are shown in Fig. 3.1(a) and (b), respectively, and the closed boxes represents respective unit cells. Colors in Fig. 3.1 shows the intensity plot of the potential. White regions are zero-potential region, and repulsive potential increases from white to dark red. Fig. 3.1(a) depicts a square lattice with spacing  $a = 1$ . We define packing fraction  $\Phi$  of the system as the fraction of the area of a unit cell occupied by the obstacles and the ABP. Therefore, in model I the packing fraction is given by  $\Phi = (\pi R_o^2 + \pi R_p^2)/a^2$ . We vary  $\Phi$  from 0.125 (obstacle free substrate) to 0.39 by changing  $R_o$  so that the ABP does not get confined in a unit cell and it can pass through the obstacles.

In Fig. 3.1(b) a corrugated channel of width  $d$  (*i.e.*, centre to centre separation of two neighboring obstacles in the  $y$ -direction) is shown schematically. The channel is composed of elliptical or circular-disk shaped obstacles arrayed along the  $x$ -direction with periodicity  $a$ . The packing fraction for corrugated channel is defined as,  $\Phi = (\pi a' b' + \pi R_p^2)/ad$ . We vary  $\Phi$  in model II from 0.10 to 0.60. The surface to surface separation of the obstacles are chosen such that the ABP can not pass through the obstacles along  $y$ -direction.

The dimensionless angular Peclet number is defined as  $Pe = v_0/D_R R_p$ . The persistent length of the particle is defined as  $l = v_0/D_R$ , and the corresponding persistent time  $\tau = 1/D_R$ . The rotational diffusion constant is kept fixed at  $D_R = 0.1$ , and  $v_0$  is varied in our study. Initially the ABP is placed randomly in one of the unit cells with random  $e$ . The dynamics of the ABP is studied using the evolution Eqs. (3.1)-(3.2). Periodic boundary condition is used in both directions for model I and in  $x$ -direction for model II. Simulation is done for total time steps  $10^6$  and  $10^7$  for model I and II, respectively, and smallest time step considered is  $\Delta t = 10^{-3}$ . All the physical quantities calculated here are averaged over 10000 realizations.

### 3.3 RESULTS

#### 3.3.1 Substrate with periodic array of obstacles

We first study the dynamics of the ABP on a 2D substrate with periodic array of obstacles, *i.e.*, for model I. Typical trajectories of the ABP is shown in Fig. 3.2. The ballistic motion at

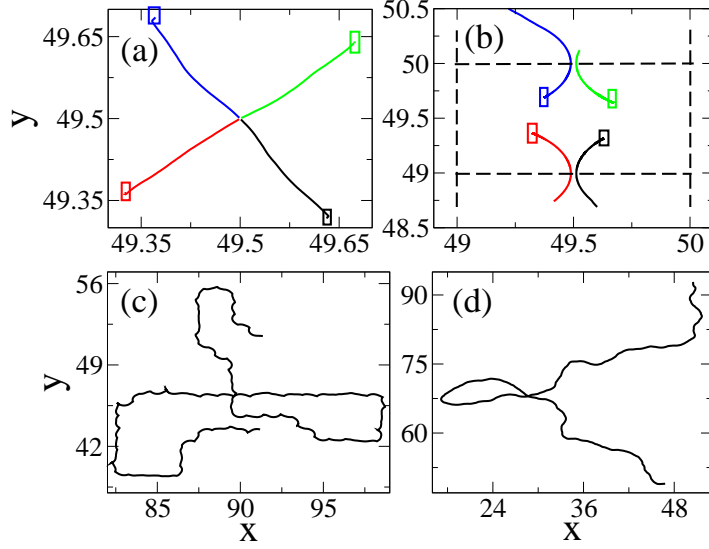


Figure 3.2: Plot of ballistic trajectory of four ABPs at the beginning and when they follow the obstacle boundary are shown in (a) and (b) respectively. Initial coordinate for all ABPs is  $(49.5, 49.5)$ , and their directions are different. Four different colors used for four ABPs. The intersection points of the dotted lines in (b) represent centre of an obstacle. The boxes in (a) represent the end point of the trajectories, and boxes in (b) represent the starting of the trajectories.  $\Phi = 0.39$ . Plot of late time diffusive trajectory of an ABP on the two dimensional periodic obstacle substrate of  $\Phi = 0.39$ , and  $\Phi = 0.125$  (free substrate) are shown in (c) and (d) respectively. The time interval is same (100) in (c) and (d). We consider  $Pe = 50$ .

the beginning for four ABPs with different initial direction is shown in Fig. 3.2(a). Interplay of obstacle hindrance and  $D_R$  causes the ABP to follow obstacle boundary, which is shown in Fig. 3.2(b). This phenomena also present at late time motion. The late time trajectories of the ABP on the 2D substrate with periodic obstacles and in obstacle free space are shown in Fig. 3.2(c) and (d) respectively. An interesting point to note from these two figures is that the late time trajectory of the ABP shows more directional motion in a periodic obstacle environment in comparison to the free space.

To characterize the dynamics of the ABP, we calculate its mean square displacement (MSD) defined as

$$\langle \Delta r^2(t) \rangle = \frac{1}{N} \sum_{n=1}^N \left[ (x_n(t) - x_n(0))^2 + (y_n(t) - y_n(0))^2 \right], \quad (3.6)$$

where  $N$  is the total number of realizations,  $x_n(t)$  and  $y_n(t)$  represent the respective coordinates of the ABP at time  $t$  for the  $n^{\text{th}}$  ensemble in the  $x$ - $y$  plane. The MSD of the ABP in a periodic obstacle environment and in a free substrate for different  $Pe$  are shown in Fig. 3.3(a)

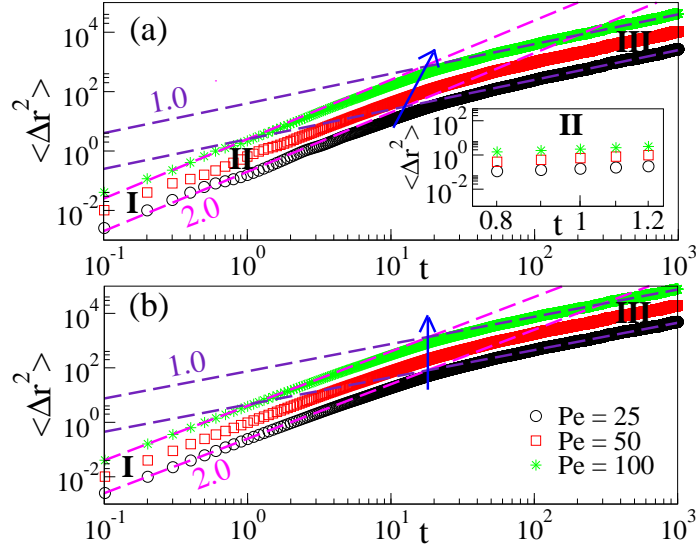


Figure 3.3: Plot of the mean square displacement of the ABP  $\langle \Delta r^2 \rangle$  vs. time  $t$  in the periodic square lattice of  $\Phi = 0.39$  (a) and  $\Phi = 0.125$  (obstacle free substrate)(b). Region I and III are ballistic and diffusive regions of the ABP respectively. Line of slope 2 (magenta) and 1 (indigo) are shown. The approximate cross-over point from super-diffusive to diffusive dynamics for different  $Pe$  for both cases are shown by an blue arrow. In inset of (a),  $\langle \Delta r^2 \rangle$  with time  $t$  for different  $Pe$  in region II (when ABP moves along obstacle boundary) is shown.

and (b), respectively. The ABP performs persistent random walk, which is one of the common features in the active systems [92, 98, 122, 123]. Therefore, the MSD can be written as,

$$\langle \Delta r^2 \rangle = 2\mathcal{D}D_{eff}t \left[ 1 - \exp\left(-\frac{t}{t_c}\right) \right], \quad (3.7)$$

where  $\mathcal{D}$  represents dimensionality of the space,  $D_{eff}$  is the effective diffusion constant in the steady state, and  $t_c$  is the cross-over time from initial ballistic regime  $\langle \Delta r^2 \rangle = 4D_{eff}t^2/t_c$  for  $t \ll t_c$  to late time diffusive regime  $\langle \Delta r^2 \rangle = 4D_{eff}t$  for  $t \gg t_c$ . The two lines of slope 2 and 1 shown in Fig. 3.3 represent the ballistic (I) and the diffusive (III) regimes of the ABP, respectively, for different  $Pe$ . We estimate the effective diffusivity  $D_{eff}$  from asymptotic limit of  $\langle \Delta r^2 \rangle / 4t$  vs.  $t$  variation as shown in Fig. 3.5 (a), and the cross-over time  $t_c$  is estimated by fitting numerical data with Eq. 3.7. The cross-over time  $t_c$  for the obstacle free environment does not change with  $Pe$ , but  $t_c$  changes with  $Pe$  for the periodic obstacle environment. The approximate change in  $t_c$  is shown by arrows in Fig. 3.3 (a) and (b). The ABP also realizes a small confinement effect (regime with label II) in the presence

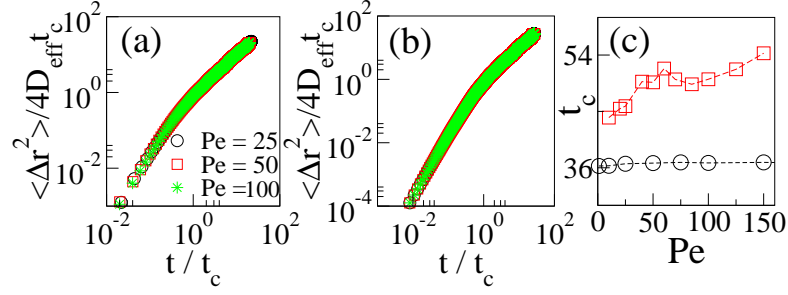


Figure 3.4: Plot of scaled mean square displacement  $\langle \Delta r^2 \rangle / 4D_{eff}t_c$  vs. scaled time  $t/t_c$  of the ABP in the square lattice of  $\Phi = 0.39$  (a) and  $\Phi = 0.125$  (obstacle free substrate) (b) are shown. (c) The cross-over time  $t_c$  with  $Pe$  for  $\Phi = 0.39$  and  $\Phi = 0.125$ (obstacle free substrate) are shown by red squares and black circles respectively.

of the obstacles during its persistent motion, and MSD shows plateau for that time duration, which is shown in the inset of Fig. 3.3(a), and this kind of confinement is also present at long-time. The scaled MSD  $\langle \Delta r^2 \rangle / 4D_{eff}t_c$  versus scaled time  $t/t_c$  for different  $Pe$  for the periodic obstacle and the obstacle free environment are plotted in Fig. 3.4(a) and (b), respectively. In both cases, the data shows good scaling collapse. The plot of  $t_c$  versus  $Pe$  for the periodic obstacle (squares) and obstacle free substrate (circles) are shown in Fig. 3.4(c). The  $t_c$  changes with  $Pe$  for the periodic obstacle substrate, whereas it is constant for the free substrate. Also, the  $t_c$  is larger for the periodic obstacle environment as compared to the free case. Therefore, the periodicity enhances the persistent motion of the ABP.

Variation in the effective diffusion constant  $D_{eff}$  with  $Pe^2$  for different  $\Phi$  are shown in Fig. 3.5(b). The enhanced diffusion is one of the intrinsic features in active systems, as found before in [126]. We find the effective diffusivity  $D_{eff}$  of the ABP for a fixed  $v_0$  decreases as we increase  $\Phi$ . For  $\Phi = 0.39$  and  $0.125$ ,  $D_{eff} \sim Pe^2$  with slopes 0.0009 and 0.0018 respectively. Interestingly,  $D_{eff}$  in the dense periodic ( $p$ ) obstacle environment is exactly half of its value in the obstacle free ( $f$ ) space. In the steady state, the MSD of the ABP can be expressed by  $2\mathfrak{D}_{eff}D_{eff}^{p/f}t$ , where  $\mathfrak{D}_{eff}$  is the effective dimensionality of the space and  $D_{eff}^{p/f}$  represents the effective diffusivity in the periodic obstacle / obstacle free environment. Since  $D_{eff}^p = \frac{1}{2}D_{eff}^f$ , that implies the effective dimensionality for the system for a dense periodic array of obstacles reduces to one. To further explain this, we calculate the probability distribution function  $P(\Theta)$  of the instantaneous orientation  $\Theta$  of the ABP in the steady state. Plots of  $P(\Theta)$  for the periodic obstacle and the obstacle free substrate are shown in Fig. 3.5(c) and (d), respectively.  $P(\Theta)$  shows peaks for a dense periodic obstacle environment and magnitude

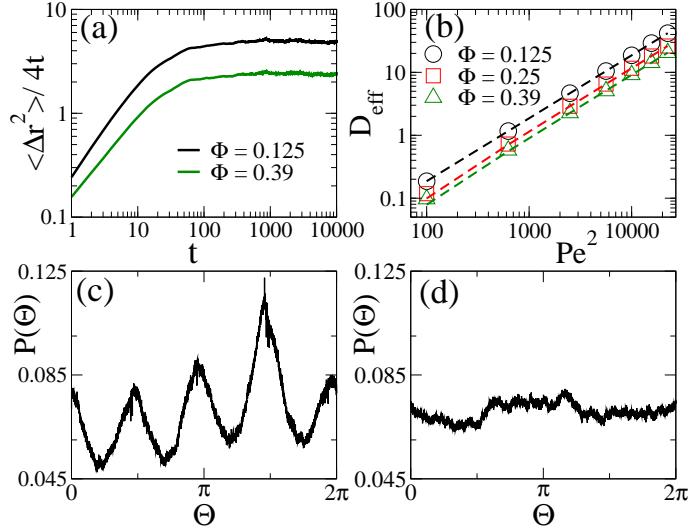


Figure 3.5: (a) Variation of the  $\langle \Delta r^2 \rangle / 4t$  with time  $t$  for  $Pe = 50$  is shown. The black and green line is for  $\Phi = 0.125$  (obstacle free substrate) and  $\Phi = 0.39$ , respectively. (b) Plot of the effective translational diffusion constant  $D_{eff}$  of the ABP for different  $Pe$ . The black circles and red squares and blue triangles are for the periodic  $\Phi = 0.125$  (obstacle free substrate),  $\Phi = 0.25$  and  $\Phi = 0.39$  respectively. Linear slope for  $\Phi = 0.125, 0.25$  and  $0.39$  are  $0.0018, 0.0011, 0.0009$ , respectively. Plot of  $P(\Theta)$  of the ABP for  $\Phi = 0.39$  and  $\Phi = 0.125$  (obstacle free substrate) are shown in (c) and (d) respectively. For (c) and (d) we consider  $Pe = 50$ .

of one peak is always larger. The height of the peaks decrease as we decrease  $\Phi$  (data is not shown). However,  $P(\Theta)$  becomes flat for obstacle free environment. Therefore the ABP moving in a dense periodic obstacle environment shows directional preference during its motion. It explains why the  $D_{eff}$  of the ABP in periodic environment is half of its value in free space.

The periodic arrangement of the obstacles enhances the persistent motion of the ABP, and at the late time, the motion is more like one-dimensional persistent random walk. This phenomenon of the ABP is not present either in random obstacles [98] or in free environment. The immediate question arises what will happen if we restrict the motion of the ABP along one direction only. In the next part of this paper we study the dynamics of the ABP in a quasi-one-dimensional corrugated channel as shown in Fig. 3.1(b).

### 3.3.2 Corrugated channel

First we consider a corrugated channel comprised of circular-disk shaped obstacles with periodicity  $a$  and width  $d$ . The radii of each obstacle and the ABP are chosen as  $R_o = 0.29$  and  $R_p = 0.2$ , respectively. The dynamics of the ABP is characterized by its MSD as defined in Eq. (3.6) and a MSD exponent  $\beta$  such that  $\langle \Delta r^2(t) \rangle \sim t^\beta$ . This exponent  $\beta$  can also be defined as

$$\beta(t) = \log_{10} \frac{\langle \Delta r^2(10t) \rangle}{\langle \Delta r^2(t) \rangle}. \quad (3.8)$$

The exponent  $\beta = 2$  and  $1$  for the ballistic and the diffusive dynamics, respectively. We fixed periodicity of the channel, and changed the width of the channel to vary the  $\Phi$  of the system. The MSD for different  $\Phi$  is shown in Fig. 3.6(a), and we calculate the  $\beta$  from MSD data. We note that at early time  $t \lesssim 100$ , the exponent  $\beta < 1$  for large  $\Phi$ , *i.e.*, the ABP exhibits sub-diffusive dynamics for high packing fraction and it exhibits diffusive dynamics ( $\beta = 1$ ) for low packing fraction, as shown in Fig. 3.6(b). However, at the late time  $t \gtrsim 100$ , the ABP shows super-diffusive behavior ( $\beta > 1$ ) only for high packing fraction ( $\Phi = 0.52, 0.43$ ), whereas for low packing fraction ( $\Phi = 0.17$ ) of the channel, the dynamics is diffusive ( $\beta = 1$ ), as shown in Fig. 3.6(c). Here we consider  $Pe = 100$ , and we also note similar behavior for  $Pe = 50$ .

To understand the importance of the corrugated geometry, we also calculate the MSD of the ABP in a quasi-one-dimensional channel with flat boundary. We note that the ABP performs diffusive motion in the flat geometry, as is evident from Fig. 3.6(d-f) drawn for channel width  $d = 0.42$  and ABP radius  $R_p = 0.2$ . Therefore, the quasi-one-dimensional corrugated channel drives the ABP towards super-diffusive dynamics ( $\beta > 1$ ) for sufficiently large time as shown in Fig. 6(c). But after very long time ( $\sim 3 \times 10^4$ ) the ABP changes its direction due to its rotational diffusion, and further moves in opposite direction for similar period of time. Hence, periodicity of the corrugated channel leads to much larger ( $\sim 10^4$ ) persistent time / motion of the ABP for high packing fraction  $\Phi$  of the obstacles.

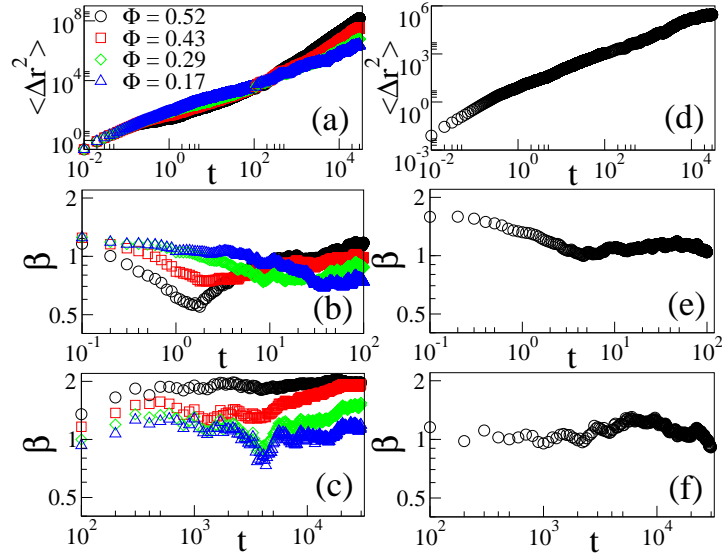


Figure 3.6: Plot of the mean square displacement  $\langle \Delta r^2 \rangle$ , the exponent  $\beta$  at early and late time of the ABP in the corrugated channel for different  $\Phi$  are shown in (a-c), respectively. We consider  $Pe = 100$  and  $\Phi$  changes as we vary channel width  $d$ .  $\langle \Delta r^2 \rangle$ , the exponent  $\beta$  at early and late time of the ABP in a flat repulsive channel of width  $d = 0.42$  are shown in (d-f), respectively. For flat channel the radius of the ABP  $r_p = 0.2$ , and  $Pe = 50$ .

The induced directionality in the quasi-one-dimensional corrugated channel motivates us to look for a net transport of the ABP through the channel. The transport is explored through statistical averages, specifically through the absolute value of the mean displacement,  $\Delta r(t) = \sqrt{\langle \Delta r^2(t) \rangle}$ . The transport speed is defined as  $V_T = \frac{1}{v_0} (\Delta r(t)/t)$ . The  $V_T$  for different packing fraction  $\Phi$  of the obstacles in the channel are shown in Fig. 3.7(a). We note that  $V_T$  increases with  $\Phi$ . We can tune the  $\Phi$  of the channel either by decreasing channel width  $d$ , or by placing the obstacles more periodically (by decreasing  $a$ ). Therefore, corru-

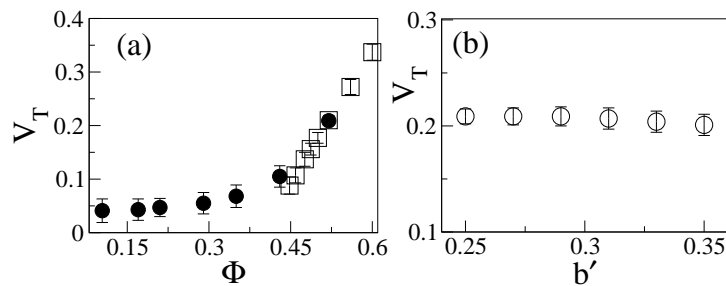


Figure 3.7: (a) Plot of the transport speed  $V_T$  of the ABP in the corrugated channel with packing fraction  $\Phi$ . We varied  $\Phi$  from 0.10 to 0.60. For circles, we change channel width  $d$  to vary  $\Phi$ , and for squares,  $\Phi$  is changed by varying periodicity  $a$  of the obstacles along the boundary of the channel. (b) Plot of  $V_T$  of the ABP in the corrugated channel comprised periodically arrayed elliptical obstacles vs.  $b'$ . We fixed the  $\Phi = 0.52$  and  $a' = 0.29$ . For (a) and (b)  $Pe = 100$ . Error bar of  $V_T$  is shown for all cases.

gated channel with closely placed circular-disk shaped obstacles speeds up the net transport of the ABP.

To study how the super-diffusive transport of the ABP depends on the shape of the corrugated channel, we consider a quasi-one-dimensional corrugated channel comprised periodically arrayed elliptical-disk shaped obstacles, as described in Sec. 4.2. The earlier described case of circular-disk shaped obstacles is a special case of the elliptical obstacles when  $a' = b'$ . We keep  $a' = 0.29$  fixed, and vary  $b'$  such that shape of the elliptical obstacles change from oblate to prolate.  $b'$  has been varied by varying the width  $d$  of the channel.  $b'$  and width  $d$  are chosen such that the packing fraction  $\Phi$  of the channel remains constant. We note that  $V_T$  does not depend on  $b'$  for a particular value of  $\Phi$ , as shown in Fig. 3.7(b). Therefore, the transport speed of the ABP in a corrugated channel does not depend on the shape of the corrugated channel.

### 3.4 DISCUSSION

In first part of this paper, we have studied dynamics of an ABP in the presence of circular-disk shaped obstacles arrayed periodically on a 2D substrate. In the presence of the periodically arrayed obstacles, the cross-over time from ballistic to diffusive dynamics of the ABP increases with its activity. We find the induced directionality in ABP's motion increases with packing fraction of the obstacles. The motion of the ABPs is directional in crowded environment when obstacles are arrayed in periodic fashion.

Motivated by the induced directed motion of the ABP in periodic crowded environment, in the second part of this paper, we have studied the motion of the ABP in a quasi-one-dimensional corrugated channel, where motion of the ABP is confined along one direction. We find the super-diffusive dynamics of the ABP over a long time in the quasi-one-dimensional corrugated channel without any external drive. This makes our study different from the previous studies, where the net transport of the ABP is observed with asymmetric corrugated channel [89] or using potential modulation in corrugated channel[90]. The net transport of the ABP in a corrugated channel does not depend on the shape of the wall.

The transport speed only depends on the packing fraction of the obstacles in the system. However, the ABP shows usual diffusive dynamics in channel with flat boundary.

Hence the channel with corrugated wall, activity of the ABP lead to super-diffusive dynamics of the ABP without any external drive. Such transport is useful to understand the dynamics of biological microorganisms, intercellular particles, since those often encounter crowded environment during their motion. This model provides significant understanding about the dynamics of the self-propelled particles in confined geometry, which can be verified in experiments and may be helpful for designing efficient transport mechanism. In our current study, we have ignored the inter-particle interaction. It is also interesting to study the dynamics of the interacting ABPs in different kinds of confined geometries.

---

## COLLECTION OF POLAR SELF-PROPELLED PARTICLES WITH A MODIFIED ALIGNMENT INTERACTION

---

### 4.1 INTRODUCTION

In previous two chapters, we have discussed about the effects of confinement. In Chapter 2, we studied the collective behavior of polar SPPs in a narrow channel. The dynamics of a ABP is studied on a heterogeneous substrate and in a corrugated channel in Chapter 3. In this chapter, we will discuss about bulk property of a collection of polar SPPs on a clean substrate. One of the key features of the polar SPPs is that there is a transition from a disordered state to a long ranged ordered state in two-dimensions with the variation of system parameters (e.g., density, noise strength) [57, 75, 76]. In the Vicsek, it is observed that the disordered to ordered state transition is continuous [57], but later other studies [75, 76] confirmed that the transition is discontinuous. Some studies on the topological distance model claim the transition to be discontinuous [127], whereas other studies [128, 129] find it continuous. Therefore, the nature of the transition of polar flock is still a matter of debate. <sup>1</sup>

In this chapter we ask a question, whether the nature of transition in polar flock can be tuned by tuning certain system parameters. And how do the characteristics of system change for the two types of transitions (discontinuous / continuous) ? To answer this, we introduce a distance dependent parameter  $a$  such that the strength of interaction decays with distance. For  $a = 1$ , the interaction is same as that in the Vicsek model. For all non-zero distance

---

<sup>1</sup> The work reported here is based on the paper “Collection of polar self-propelled particles with a modified alignment interaction”, Sudipta Pattanayak and Shradha Mishra, J. Phys. Commun. 2, 045007 (2018).

dependent parameter ( $a > 0$ ), the system is in a disordered state at small density and high noise strength, and in an ordered state at high density and low noise strength. We calculate the critical noise strength  $\eta_c(a)$  for different  $a$  and compare it with the mean-field result. The nature of the disorder to order transition continuously changes from discontinuous to continuous with decreasing  $a$ . We estimate the tri-critical point in the noise strength  $\eta$  and  $a$  plane, where the nature of the transition changes from discontinuous to continuous. We also calculate the density phase separation in the system. The density phase separation order parameter is large for  $a$  close to unity, and it monotonically decays with decreasing  $a$ . Linear stability analysis of the homogeneous ordered state shows an instability as  $a$  approaches to 1, which is consistent with large density phase separation for  $a \simeq 1$ .

This chapter is organised as follows. In section 4.2, we introduce the microscopic rule based model for distance dependent interaction. The results of numerical simulation are given in section 4.3. In section 4.4, we write the coarse-grained hydrodynamic equation of motion, calculate the mean field estimate of critical  $\eta_c(a)$ , and discuss the results of linear stability analysis. Finally in section 4.6, we discuss our results and future prospect of our study. Section 4.5 is at the end, that contains the detailed calculation of the linear stability analysis.

## 4.2 MODEL

We study a collection of polar self-propelled particles on a two-dimensional substrate. The particles interact through a short range *alignment* interaction, which decays with the metric distance.

Each particle is defined by its position  $\mathbf{r}_i(t)$  and orientation  $\theta_i(t)$  or unit direction vector  $\mathbf{n}_i(t) = [\cos \theta_i(t), \sin \theta_i(t)]$ . Dynamics of the particles are given by two update equations. One for the position and other for the orientation. Self-propulsion is introduced as a motion

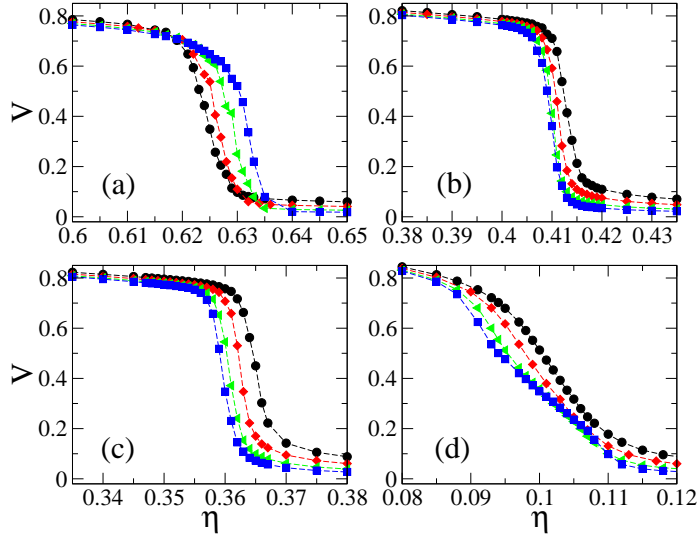


Figure 4.1: Plot of the global velocity  $V$  vs. the noise strength  $\eta$  for four different distance dependent parameters  $a$ . Fig. (a-d) are for  $a = 1.0, 0.5, 0.4, 0.01$  respectively. In Fig. (d), the variation of  $V$  is clearly continuous for all system sizes, and there is no crossover. The variation of  $V$  changes as we increase  $a$ , and there is a crossover for  $a = 1.0$ . Plot of the  $V$  for four different system sizes ( $N = 1000, 2000, 5000, 10000$ ) are shown by black  $\bullet$ , red  $\blacklozenge$ , green  $\blacktriangle$  and blue  $\blacksquare$  respectively.

towards its orientation with a fixed step size ( $v_0$  in unit time). Hence, the position update equation of the particles

$$\mathbf{r}_i(t+1) = \mathbf{r}_i(t) + v_0 \mathbf{n}_i, \quad (4.1)$$

and the orientation update equation with a distance dependent short range alignment interaction

$$\mathbf{n}_i(t+1) = \frac{\sum_{j \in R_0} \mathbf{n}_j(t) a^d + N_i(t) \eta \mathbf{1}_i}{W_i(t)} \quad (4.2)$$

where the sum is over all the particles within the interaction radius ( $R_0$ ) of the  $i^{th}$  particle, i.e.,  $|\mathbf{r}_j(t) - \mathbf{r}_i(t)| < R_0 (= 1)$ .  $N_i(t)$  is the number of particles within the interaction radius of the  $i^{th}$  particle at time  $t$ , and  $d$  is the metric distance between a pair of particles  $(i, j)$ .  $W_i(t)$  is the normalisation factor. The strength of the noise  $\eta$  is varied between zero to 1, and  $\mathbf{1}_i(t)$  is a random unit vector. Note that this model reduces to the celebrated Vicsek model for  $a = 1.0$ .

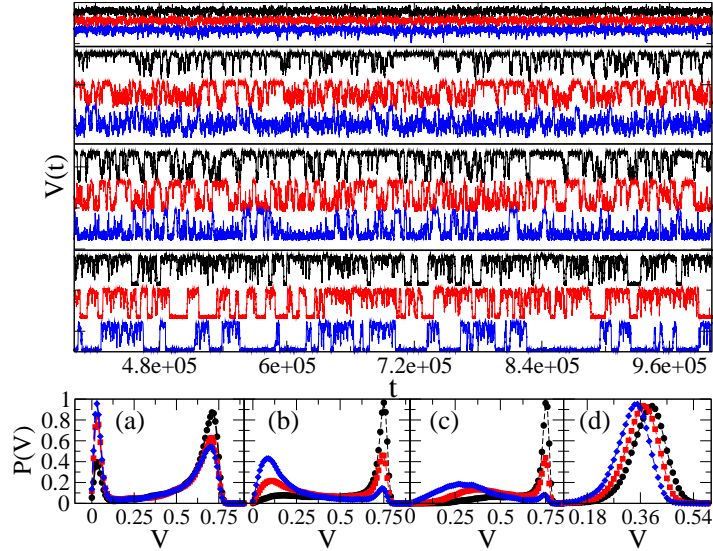


Figure 4.2: *Upper panel* : Plot of the time series of the global velocity  $V$  for four different  $a = (0.01, 0.4, 0.5, 1.0)$ , from top to bottom. The time series of the  $V$  are plotted for three different noise strengths  $\eta_1(a)$ (black)  $<$   $\eta_2(a)$ (red)  $<$   $\eta_3(a)$ (blue) close to the critical noise strength  $\eta_c$  for each  $a$ . For  $a = 0.01$  the time-series of the  $V(t)$  is shown for  $\eta_1 = 0.099$ (black),  $\eta_2 = 0.100$ (red) and  $\eta_3 = 0.101$ (blue). Similarly  $\eta_1 < \eta_2 < \eta_3$  for  $a = 0.4, 0.5$  and  $1.0$  are  $(0.358, 0.359, 0.360)$ ,  $(0.409, 0.410, 0.411)$  and  $(0.627, 0.628, 0.629)$  respectively. There is a clear switching behavior in the global velocity variation for  $a = 1.0$ , and it vanishes as we decrease  $a$ . Time-series are shifted on the vertical axis for clarity. *Lower panel* : We plot the probability distribution function (PDF) of the global velocity  $P(V)$  for four different  $a = (1.0, 0.5, 0.4, 0.01)$  in Fig. (a - d) respectively. We consider three different  $\eta$  for each  $a$ , same as in upper panel. In Fig. (a) plot of  $P(V)$  is clearly bimodal, and as we decrease  $a$  it becomes to uni-modal in Fig. (d). All the plots are for  $N = 5000$ .

### 4.3 NUMERICAL STUDY

We numerically simulate the microscopic model introduced by Eqs.4.1 and 4.2 for different distance dependent parameter  $a$ . For  $a = 1$ , the particle interacts with the same strength with all the particles inside its interaction radius (Vicsek's model [57]). As we decrease  $a$ , interaction strength decays with distance.  $a$  is varied from 1.0 to small value 0.001. For  $a = 0.0$  the particles are non-interacting. Speed of the particles is fixed to  $v_0 = 0.5$ . We start with random orientation and homogeneously distributed particles on a 2-dimensional substrate of size  $L \times L$  with periodic boundary conditions. For all the simulations, we keep mean density  $\rho_0 = \frac{N}{L^2} = 2.0$ . Number of particles were varied from  $N = 1000$  to 10000. We start from a random state and each particle is updated using Eqs. 4.1 and 4.2. One

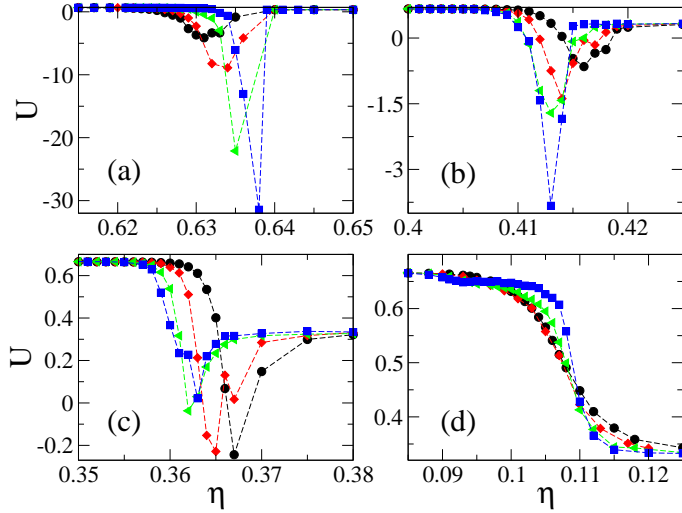


Figure 4.3: Plot of the Binder cumulant  $U$  vs. the noise strength  $\eta$  for four different distance dependent parameter  $a$ . Fig. (a-d) are for  $a = 1.0, 0.5, 0.4, 0.01$  respectively.  $U$  varies discontinuously from  $1/3$  (disordered state) to  $2/3$  (ordered state) in Fig. (a), and it goes continuously from  $1/3$  to  $2/3$  in Fig. (d). Discontinuity in the variation of  $U$  increases with system size for  $a \gtrsim 0.4$ , and it decreases for  $a \lesssim 0.4$ . Symbols have the same meaning as in Fig. 4.1.

simulation step is counted after sequential update of all the particles. All the measurements are performed after  $10^5$  simulation steps, and a total of  $10^6$  steps are used in simulations.

#### 4.3.1 Disorder-to-order transition

First we study the disorder-to-order transition in the system for different  $a$ . Ordering in the system is characterised by the global velocity,

$$V = \left| \frac{1}{N} \sum_{i=1}^N \mathbf{n}_i(t) \right|. \quad (4.3)$$

In the ordered state, i.e., when large number of particles are oriented in the same direction, then  $V$  is close to 1, and it is close to zero for a random disordered state. In Fig. 4.1 (a-d) we have shown the variation of  $V$  with the noise strength  $\eta$  for four different  $a$  ( $= 1.0, 0.5, 0.4, 0.01$ ) respectively. For  $a = 1$ , on increasing  $N$ , the variation of  $V$  shows a crossover behaviors. This kind of crossover is a common feature of first order transition [75, 127]. Whereas for  $a = 0.01$ ,  $V$  varies continuously, and the transition is second order. The

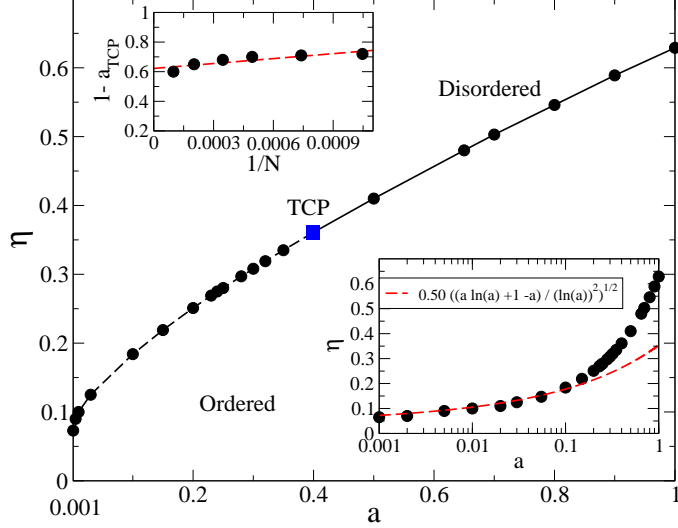


Figure 4.4: *Main* : Schematic phase diagram of the disorder-to-order transition in noise strength  $\eta$  and distance dependent parameter  $a$  ( $\eta, a$ ) plane. For all  $a > 0$  there is a phase transition from a disordered to an ordered phase with decreasing  $\eta$  across the critical noise strength line. Dashed line indicates the nature of the transition is continuous, whereas solid line indicates the discontinuous transition. The nature of transition changes from discontinuous to continuous at a tri-critical point  $a_{TCP}$  (square). *Lower inset*: we compare with the mean-field calculation of the critical noise strength  $\eta_c$  for different  $a$  with our numerical data. Mean field results fit well with numerical data for small values of  $a$ . In upper inset : plot of  $1 - a_{TCP}$  vs.  $1/N$  shows the variation of TCP with system size. We find  $a_{TCP}$  converges to  $a \approx 0.39$  for  $N \rightarrow \infty$  (thermodynamic limit).

variation of  $V$  in the intermediate region of  $a$ , changes smoothly from one type to another. We also estimate the critical  $\eta_c(a)$  for different  $a$  values, and it decreases with  $a$ , provided other parameters (*viz* mean density  $\rho_0$ , speed  $v_0$ ) are kept fixed.

Now to characterize the nature of the transition with the variation of  $a$ , we plot the time series of the global velocity  $V(t)$  for four different  $a$  ( $= 0.01, 0.4, 0.5, 1.0$ ), from top to bottom in the upper panel of Fig. 4.2. We choose three different  $\eta$  ( $\eta_1(a)$ (black)  $<$   $\eta_2(a)$ (red)  $<$   $\eta_3(a)$ (blue)) for each  $a$  close to the critical noise strength  $\eta_c(a)$ . For  $a = 1$ , we choose  $\eta_1 = 0.627$ ,  $\eta_2 = 0.628$  and  $\eta_3 = 0.629$ , and plotted the time-series of  $V$ .  $V(t)$  shows switching behaviour, and it alternates between two finite values of  $V$ .  $V(t)$  keeps switching throughout the simulation time. At smaller  $a = 0.5$  ( $\eta_1 = 0.409$ ,  $\eta_2 = 0.410$ ,  $\eta_3 = 0.411$ ) we again find switching behaviour, but the difference between two finite values of  $V$  decreases. Switching behaviour further reduces for  $a = 0.4$  ( $\eta_1 = 0.358$ ,  $\eta_2 = 0.359$ ,  $\eta_3 = 0.360$ ). For small

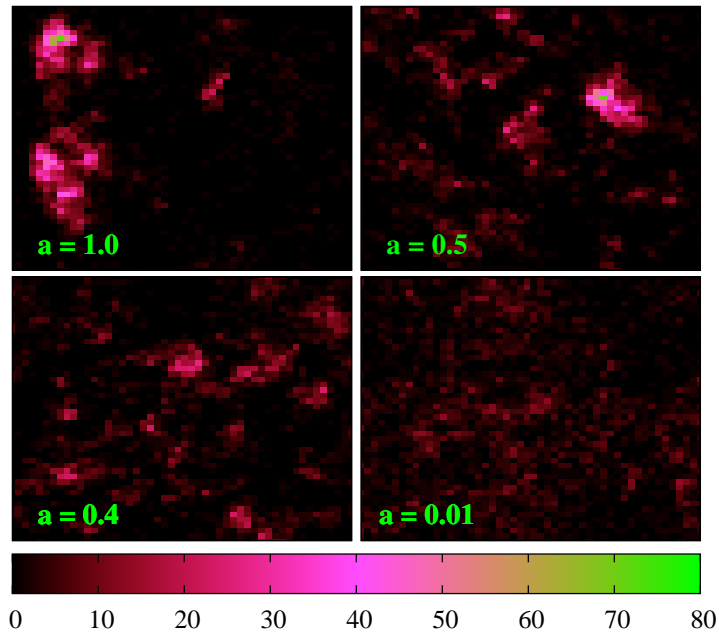


Figure 4.5: Plot of real space snapshots of the particle density distribution for four different  $a(1.0, 0.5, 0.4, 0.01)$ . *Upper panel:* Plot of the particle density distribution for  $a = 1.0$  and  $a = 0.5$  from left to right respectively. *Lower panel:* Plot of the particle density distribution for  $a = 0.4$  and  $a = 0.01$  in the same order. Color bar shows the number of particles in a unit sized sub-cell.

$a = 0.01$  ( $\eta_1 = 0.099, \eta_2 = 0.100, \eta_3 = 0.101$ )  $V(t)$  shows fluctuations, but there is no switching behaviour. We further calculate probability distribution  $P(V)$  of the global velocity for the same set of  $a$  and  $\eta$  values as used for the time series plots. As shown in Fig. 4.2(a),  $P(V)$  is bimodal for  $a = 1.0$ , i.e., there are two distinct peaks for  $P(V)$ . Two finite values of  $V$  corresponds to two states of the system. Two peaks come closer with decreasing  $a$ , and for small  $a(= 0.01)$ ,  $P(V)$  shows only one broad peak in Fig. 4.2(d). The bimodal distribution of the  $V$  confirms that the transition is discontinuous for  $a \simeq 1$ .

To further characterise the nature of the transition, we calculate the fourth order cumulant or the Binder cumulant, i.e.,

$$U = 1 - \frac{\langle V^4 \rangle}{3 \langle V^2 \rangle^2} \quad (4.4)$$

$U(\eta)$  vs.  $\eta$  plot is shown in Fig. 4.3. It shows strong discontinuity from  $U = 1/3$  (for disordered state) to  $U = 2/3$  (for ordered state) as we approach critical  $\eta_c(a)$  for  $a = 1$  in Fig. 4.3

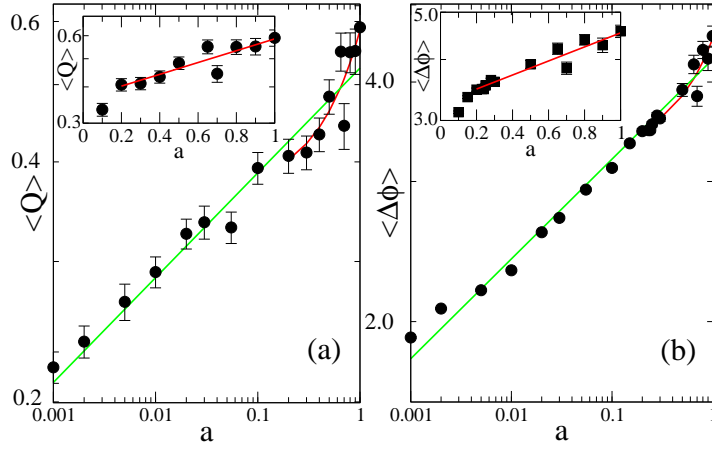


Figure 4.6: Plot of the average density phase separation order parameter  $\langle Q \rangle$  vs.  $a$ , and the average standard deviation in particle number in a unit cell  $\langle \Delta\phi \rangle$  vs.  $a$  are shown in Fig. (a) and (b) respectively in log-log scale.  $\langle Q \rangle$  and  $\langle \Delta\phi \rangle$  decay exponentially from  $a = 1.0$  to  $a \approx 0.2$ . Both show similar power law decay with the exponent 0.13, for small values of  $a$ . In the insets of Fig (a) and (b), we show the exponential decay of the  $\langle Q \rangle$  ( $\sim e^{0.46a}$ ) and  $\langle \Delta\phi \rangle$  ( $\sim e^{0.33a}$ ) in semi-log scale.

(a), and discontinuity decreases with  $a$ . It smoothly goes from a disordered state ( $U = 1/3$ ) to an ordered state ( $U = 2/3$ ) for  $a = 0.01$  in Fig. 4.3 (d). For  $a \gtrsim 0.4$ ,  $U$  vs.  $\eta$  plot shows strong discontinuity at large  $N$ , but for  $a \lesssim 0.4$  it becomes continuous.

Therefore, The nature of the transition continuously changes from discontinuous to continuous on decreasing  $a$ . The critical noise strength  $\eta_c(a)$  also decreases with decreasing  $a$ . We plot  $\eta_c(a)$  vs.  $a$  in the of Fig. 4.4. The solid line indicates the nature of the disorder-to-order transition is discontinuous, and the dashed line indicates the continuous transition. The value of  $a$  at which the above transition changes from discontinuous to continuous one, we call it as tri-critical-point (TCP)  $a_{TCP}$ . For  $a > a_{TCP}$  the transition is discontinuous, and for  $a < a_{TCP}$  it is continuous. TCP shows a small dependence on  $N$  for any fixed  $v_0$  and  $\rho_0$ . We define the TCP for any system size as the point where the Binder cumulant  $U$  starts to show discontinuous variation. In the upper inset of Fig. 4.4, we plot  $1 - a_{TCP}$  vs.  $1/N$ , and extrapolate the TCP for  $N \rightarrow \infty$  or  $1/N \rightarrow$  zero. As  $1/N$  approaches to zero,  $1 - a_{TCP} \approx 0.61$ . Hence the  $a_{TCP}$  is  $\approx 0.39$ . Hence, the extrapolated value of  $a_{TCP}$  matches well with the  $a_{TCP}$  in phase diagram, which is marked as blue square in Fig. 4.4. In the lower inset of Fig. 4.4, we plot

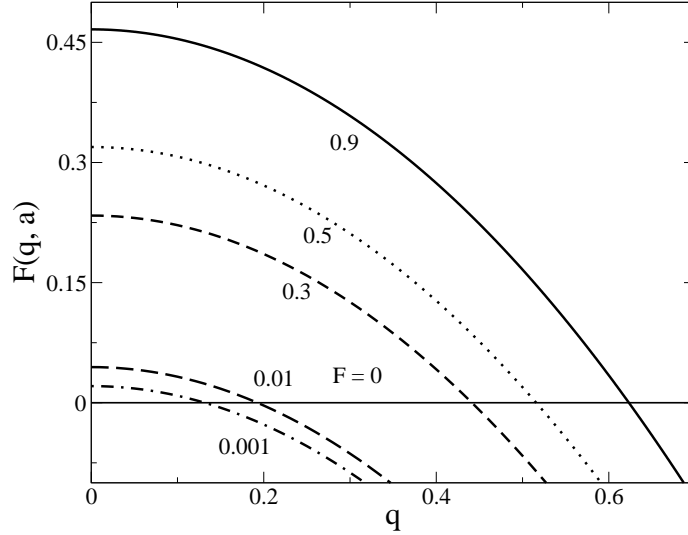


Figure 4.7: Plot of  $F(q, a) = \frac{(a \ln(a) + 1 - a)}{(\ln(a))^2} - \frac{D_V q^2}{2} \left[ \left( \frac{\lambda}{v_0} - 1 \right) + \sqrt{\left( \frac{\lambda}{v_0} - 1 \right)^2 + \frac{1}{2v_0}} \right]$  vs. wave vector  $q$ . For  $v_0 = 0.5$ ,  $D_v = 1.0$ ,  $\lambda = 1.0$ ,  $\alpha_0 = 1.0$ .  $F(q, a)$  becomes +ve for small  $q$ , which suggests that hydrodynamic mode becomes unstable at smaller wave vector. Region of instability continuously increases with increasing  $a$ .

the critical  $\eta_c(a)$  vs.  $a$  on semi-log scale and compare the results with the mean field result in Eq. 4.13. Mean field approximation is good when density distribution is homogeneous. In such limit, density at each point is close to the mean density of the system. As shown in Fig. 4.5 density distribution becomes more and more inhomogeneous as we increase  $a$ . Hence, for the small  $a$  values numerical estimate of  $\eta_c(a)$  should be more close to MF. We show in lower inset of Fig. 4.4 the numerical  $\eta_c(a)$  matches very well with MF for small  $a < 0.1$ .

#### 4.3.2 Density phase separation

The density distribution of particles also changes as we vary  $a$ . Density fluctuation plays an important role in determining the nature of the transition in polar flock [50, 75, 110, 130–133]. In Fig. 4.5 we show the real space snapshot of particle density for different  $a$  ( $= 1, 0.5, 0.4$  and  $0.01$ ) close to critical noise strength  $\eta_c(a)$ . Clusters are small and homogeneously distributed for small  $a$ , but as  $a$  approaches to 1 we find large, dense and anisotropic clusters. We

quantify the density distribution by calculating the density phase separation order parameter in Fourier space defined as,

$$Q(\mathbf{k}) = \left| \frac{1}{L} \sum_{i,j=1}^L e^{i\mathbf{k}\cdot\mathbf{r}} \rho(i,j) \right| \quad (4.5)$$

where  $\mathbf{k} = \frac{2\pi(m,n)}{L}$  is a two dimensional wave vector and  $m, n = 0, 1, 2, \dots, L-1$ . The reference frame is chosen so that the orthogonal axes  $(1,0)$  and  $(0,1)$  are along the boundary of the substrate, and  $(1,1)$  represents diagonal direction. We calculate the first non-zero value of  $Q(\mathbf{k})$  in all three directions  $Q(1,0)$ ,  $Q(0,1)$  and  $Q(1,1)$ . The average density phase separation order parameter  $\langle Q \rangle$  is  $(Q(1,0) + Q(0,1) + Q(1,1))/3$ .

We also characterize the density phase separation using the standard deviation in particle number  $\Delta\phi$  in a unit size sub-cell. It is defined as

$$\Delta\phi = \sqrt{\frac{1}{N_c} \sum_{j=1}^{N_c} (\phi_j)^2 - \left( \frac{1}{N_c} \sum_{j=1}^{N_c} \phi_j \right)^2} \quad (4.6)$$

where  $\phi_j$  is the number of particles in the  $j^{\text{th}}$  sub-cell. To calculate  $\Delta\phi$  we first divide the whole system into  $N_c (= L^2)$  unit sized sub-cells, then calculate the number of particles in each sub-cell, and from there we calculate the standard deviation in particle distribution.  $Q(t)$  and  $\Delta\phi(t)$  are calculated at different times in the steady state, and then average over a large time to obtain  $\langle Q \rangle$  and  $\langle \Delta\phi \rangle$  respectively. Plots of  $\langle Q \rangle$  and  $\langle \Delta\phi \rangle$  vs.  $a$  on log-log scale are shown on Fig. 4.6 (a) and (b) respectively. For  $a \simeq 1$  both  $\langle Q \rangle$  and  $\Delta\phi$  are large; however, as we decrease  $a$ , they decay monotonically. For  $a$  close to unity both  $\langle Q \rangle$  and  $\langle \Delta\phi \rangle$  show fast decay (*exponential*), and for smaller  $a$  they decay algebraically with  $a$ . In the insets of Fig. (a) and (b), we show the exponential decay of the density phase separation order parameter  $\langle Q \rangle$  ( $\sim e^{0.46a}$ ), and the standard deviation in particle distribution  $\langle \Delta\phi \rangle$  ( $\sim e^{0.33a}$ ) for  $a \approx 1$ . We find that for  $a \approx 1$ , the density phase separation is high, and the nature of the disorder-to-order transition is also first order. Hence, the change in the nature of both the disorder-to-order transition and the density phase separation shows

variation on decreasing  $a$ .

#### 4.4 HYDRODYNAMIC EQUATIONS OF MOTION

We estimate the  $\eta_c(a)$  and also study the linear stability of homogeneous ordered state with varying  $a$ . The coarse-grained hydrodynamic variables are coarse-grained density  $\rho(r, t)$  and velocity  $V(r, t)$  and they are defined as,

$$\rho(\mathbf{r}, t) = \sum_{i=1}^N \delta(\mathbf{r} - \mathbf{r}_i(t)) \quad (4.7)$$

$$\mathbf{V}(\mathbf{r}, t) = \frac{\sum_{i=1}^N v_0 \mathbf{n}_i(t) \delta(\mathbf{r} - \mathbf{r}_i(t))}{\rho(\mathbf{r}, t)} \quad (4.8)$$

We can write the coupled hydrodynamic equations of motion for density and velocity as obtained in Toner and Tu [52, 63]

$$\partial_t \rho = -v_0 \nabla \cdot (\rho \mathbf{V}) \quad (4.9)$$

and for velocity

$$\partial_t \mathbf{V} = \alpha(\rho, \eta, a) \mathbf{V} - \beta(|V|^2) \mathbf{V} - \frac{v_1}{2\rho_0} \nabla \rho + D_V \nabla^2 \mathbf{V} - \lambda_1 (\mathbf{V} \cdot \nabla) \mathbf{V} - \lambda_2 (\nabla \cdot \mathbf{V}) \mathbf{V} - \lambda_3 \nabla (|V|^2) \quad (4.10)$$

For our distance dependent model we have introduced an additional general  $a$  dependence to alignment parameter  $\alpha(\rho, \eta, a)$  in the velocity equation 4.10. In [52, 63]  $\alpha$  is treated as a constant. But in general  $\alpha$  is a function of microscopic parameters (e.g. density, noise strength etc.) when derived from microscopic model. For  $a = 1$ , our model reduces to the Vicsek's model, and  $\alpha = \alpha_0(\rho - \rho_c)$ .  $\rho_c$  in general depends on system parameters (*viz*: noise strength, speed etc.) On increasing density large noise is required to break the order or  $\rho_c$  increases

with  $\eta$ . Using mean-field-like argument it can be shown that  $\rho_c \simeq \frac{\eta^2}{v_0^2}$  [75] or  $\alpha = \alpha_0(\rho - 4\eta^2)$ .  $\alpha$  shows linear dependence on  $\rho$  for  $a = 1$ , when all the particles within the coarse-grained radius interact with same strength. In general for  $a < 1$ , strength of interaction decays with distance. Again using the mean-field limit when density inside the coarse-grained radius is homogeneous, following form of  $\alpha$  is obtained

$$\alpha(\rho, a, \eta) = \alpha_0 \left( \rho_0 \left[ \frac{(a \ln(a) + 1 - a)}{(\ln(a))^2} \right] - 8\eta^2 \right) \quad (4.11)$$

Hence  $\alpha$  changes sign at critical  $\eta_c$ .

$$\eta_c(a) = \sqrt{\frac{\rho_0}{8}} \sqrt{\frac{(a \ln(a) + 1 - a)}{(\ln(a))^2}} \quad (4.12)$$

Which for mean density  $\rho_0 = 2.0$  reduces to

$$\eta_c(a) = \frac{1}{2} \sqrt{\frac{(a \ln(a) + 1 - a)}{(\ln(a))^2}} \quad (4.13)$$

The homogeneous solution for the disordered state is  $V_0 = 0$  (for  $\eta > \eta_c$ ), and for the ordered state is  $V_0 = \sqrt{\frac{\alpha(\rho_0, a)}{\beta}}$  (for  $\eta < \eta_c$ ).

In Fig. 4.4 (lower inset) we plot the function  $\eta_c(a)$  vs.  $a$  as given in Eq.4.13 on semi-log scale and its comparison to numerically estimated  $\eta_c(a)$ . We find that the data matches very well with numerical result for small  $a$  limit. Deviation from the MF expression increases with increasing  $a$  when the density distribution becomes more inhomogeneous Fig. 4.5.

Now we study the linear stability analysis of Eqs. 4.9 and 4.10 about the homogeneous ordered state for general  $a$ . Detail steps of linear stability analysis are given in the section 4.5. We find that for large  $a$  homogeneous ordered state is unstable with respect to small perturbation. The condition for the instability is obtained in Eq. 4.28.

$$\alpha'_1 > \frac{D_V q^2}{2} \left[ \left( \frac{\lambda}{v_0} - 1 \right) + \sqrt{\left( \frac{\lambda}{v_0} - 1 \right)^2 + \frac{1}{2v_0}} \right] \quad (4.14)$$

where  $\alpha'_1(\rho_0) = \frac{d\alpha(\rho)}{d\rho}|_{\rho=\rho_0} = \alpha_0 \left( \left[ \frac{a \ln(a) + 1 - a}{(\ln(a))^2} \right] \right)$ . Hence, using the expression for  $\alpha$  from Eq. 4.11 we get condition for instability of the hydrodynamic mode,

$$\alpha_0 \frac{(a \ln(a) + 1 - a)}{(\ln(a))^2} - \frac{D_V q^2}{2} \left[ \left( \frac{\lambda}{v_0} - 1 \right) + \sqrt{\left( \frac{\lambda}{v_0} - 1 \right)^2 + \frac{1}{2v_0}} \right] > 0 \quad (4.15)$$

We plot  $F(q, a) = \alpha_0 \frac{(a \ln(a) + 1 - a)}{(\ln(a))^2} - \frac{D_V q^2}{2} \left[ \left( \frac{\lambda}{v_0} - 1 \right) + \sqrt{\left( \frac{\lambda}{v_0} - 1 \right)^2 + \frac{1}{2v_0}} \right]$  vs.  $a$  in Fig. 4.7, and find that the instability of the hydrodynamic mode increases with  $a$ . Unstable homogeneous state for  $a \approx 1$  is consistent with the large density phase separation obtained in numerical simulation. System shows first order disorder-to-order transition for large  $a$ . As we decrease  $a$  the nature of the transition changes continuously, and also the density phase separation decays.

#### 4.5 LINEARISED STUDY OF THE BROKEN SYMMETRY STATE

The hydrodynamic equations Eq.4.9 and 4.10 admit two homogeneous solutions: an isotropic state with  $\mathbf{V} = 0$  for  $\rho < \rho_c$  and a homogeneous ordered state with  $\mathbf{V} = V_0 \mathbf{x}$  for  $\rho > \rho_c$ , where  $\mathbf{x}$  is the direction of ordering. We are mainly interested in the symmetry broken phase. For  $\alpha(\rho) > 0$  we can write the velocity field as  $\mathbf{V} = (V_0 + \delta V_x) \mathbf{x} + \delta V_y \mathbf{y}$ , where  $\mathbf{x}$  is the direction of broken symmetry and  $\mathbf{y}$  is the perpendicular direction.  $V_0 \mathbf{x} = \langle \mathbf{V} \rangle$  is the spontaneous average value of  $\mathbf{V}$  in ordered phase. We choose  $V_0 = \sqrt{\frac{\alpha(\rho_0, a)}{\beta}}$  and  $\rho = \rho_0 + \delta\rho$  where  $\rho_0$  is coarse-grained density. Combining the fluctuations we can write in a vector format,

$$\delta X_\alpha(\mathbf{r}, t) = \begin{bmatrix} \delta\rho \\ \delta V_x \\ \delta V_y \end{bmatrix} \quad (4.16)$$

Now we introduce fluctuations in hydrodynamic equation for density and if we consider only linear terms then Eq.4.9 will reduce to,

$$\partial_t \delta\rho + v_0 V_0 \partial_x \delta\rho + v_0 \rho_0 \partial_x \delta V_x + v_0 \rho_0 \partial_y \delta V_y = 0 \quad (4.17)$$

We consider the velocity fluctuation only in the direction of orientational ordering. So  $\delta V_y$  and  $q_y$  is zero in our analysis. Now density Eq. 4.17 we can write as,

$$\partial_t \delta \rho + v_0 V_0 \partial_x \delta \rho + v_0 \rho_0 \partial_x \delta V_x = 0 \quad (4.18)$$

Similarly we introduce fluctuations in velocity Eq. 4.10 and we are writing velocity fluctuation equation for ordering direction. We also introduce functional density dependency in  $\alpha(\rho)$ . We have done Taylor series expansion of  $\alpha(\rho)$  in Eq.4.10 at  $\rho = \rho_0$ , and consider upto first order derivative term of  $\alpha(\rho)$ . Now velocity equation will reduces to,

$$\begin{aligned} \partial_t \delta V_x = & (\alpha(\rho_0) + \alpha'_1(\rho_0) \delta \rho)(V_0 + \delta V_x) - \beta(V_0^2 + 2V_0 \delta V_x)(V_0 + \delta V_x) - \frac{v_1}{2\rho_0} \partial_x \delta \rho \\ & + D_V \partial_x^2 \delta V_x + D_V \partial_y^2 \delta V_x - \lambda V_0 \partial_x \delta V_x \end{aligned} \quad (4.19)$$

where  $\alpha'_1 = \frac{\partial \alpha}{\partial \rho} |_{\rho_0}$  also  $\lambda$  is combination of three  $\lambda'$ s ( $\lambda = \lambda_1 + \lambda_2 + 2\lambda_3$ ) terms.

Now considering no fluctuation along perpendicular direction of velocity field, equation along ordering direction(x-direction) reduces to,

$$\partial_t \delta V_x + 2\alpha(\rho_0) \delta V_x + \lambda V_0 \partial_x - D_V \partial_x^2 \delta V_x - \alpha'_1 V_0 \delta \rho + \frac{v_1}{2\rho_0} \partial_x \delta \rho = 0 \quad (4.20)$$

Now we are introducing Fourier component,  $\Delta Y(q, S) = \int dr \exp(i\mathbf{q} \cdot \mathbf{r}) \exp(St) dt$  in above two fluctuation equations 4.18, 4.20 . Then we are writing the coefficient matrix for the coupled equations. Here we are writing  $q_x = q$ .

$$\begin{bmatrix} S + iv_0 V_0 q & iv_0 \rho_0 q \\ i \frac{v_1}{2\rho_0} q - \alpha'_1(\rho_0) V_0 & S + 2\alpha + D_V q^2 + i\lambda V_0 q \end{bmatrix} \quad (4.21)$$

Earlier study [100, 101] finds horizontal fluctuation or fluctuation in the direction of ordering is important when system is close to transition. Here important thing is that unlike isotropic problem  $d > 2$  there is no transverse mode, we always have just two longitudinal Goldstone

modes associated with  $\delta\rho$  and  $V_x$ . We get solution for hydrodynamic modes in symmetry broken state,

$$S_{\pm} = -ic_{\pm}q - \epsilon_{\pm} \quad (4.22)$$

where the sound speeds,

$$c_{\pm} = \frac{1}{2}(\lambda + v_0)V_0 \pm c_2 \quad (4.23)$$

with

$$c_2 = \frac{1}{2}\sqrt{(\lambda - v_0)^2V_0^2 + \frac{v_0v_1}{2}} \quad (4.24)$$

and the damping  $\epsilon_{\pm}$  in the Eq. 4.22 are  $O(q^2)$  and given by,

$$\epsilon_{\pm} = \pm \frac{c_{\pm}}{2c_2}[2\alpha + D_Vq^2] \mp \frac{1}{2c_2}[2\alpha v_0V_0 + v_0V_0\alpha'_1 + v_0V_0D_Vq^2] \quad (4.25)$$

So real part of the modes are  $-\epsilon_{\pm}$ . Now we know the instability conditions are 1) If  $\text{Re}[S_{\pm}] > 0$  we will get homogeneous polarized state, which is unstable. 2) If  $\text{Re}[S_{\pm}] < 0$  we will get homogeneous polarized state, which is stable to small perturbation. We know the expression for  $\epsilon_{\pm}$ ,

$$\epsilon_{\pm} = \pm \frac{c_{\pm}}{2c_2}[D_Vq^2 + 2\alpha] \mp \frac{1}{2c_2}[2\alpha v_0V_0 + v_0V_0\alpha'_1 + v_0V_0D_Vq^2] \quad (4.26)$$

Close to transition point  $\alpha \simeq 0$ . So we can write,

$$\epsilon_{\pm} = \pm \frac{c_{\pm}}{2c_2}[D_Vq^2] \mp \frac{1}{2c_2}[v_0V_0\alpha'_1 + v_0V_0D_Vq^2] \quad (4.27)$$

We have checked  $\text{Re}[S_-] = -\epsilon_- < 0$  always holds, so this mode is always stable.  $\text{Re}[S_+] = -\epsilon_+ > 0$  for

$$\alpha'_1 > \frac{D_Vq^2}{2}\left[\left(\frac{\lambda}{v_0} - 1\right) + \sqrt{\left(\frac{\lambda}{v_0} - 1\right)^2 + \frac{1}{2v_0}}\right], \quad (4.28)$$

and then this mode becomes unstable.

#### 4.6 DISCUSSION

We introduce a variant of the Vicsek model [57] for the collection of polar self propelled particles with a modified alignment interaction. Our model is similar to the celebrated Vicsek model for  $a = 1.0$ . Numerical simulations reveal that for all  $a > 0$ , the system shows a transition from a disordered (global velocity  $V \approx 0$ ) to an ordered state (finite global velocity) on decreasing noise strength  $\eta$ , and the critical noise strength  $\eta_c(a)$  also decreases with  $a$ . We find that in a homogeneous system the disordered to ordered transition can be discontinuous or continuous depending on the distance dependent parameter  $a$ . The nature of the transition is characterized by calculating (a) the global velocity  $V$ , (b) the fourth order variance in the global velocity (Binder cumulant  $U$ ), and (c) the probability distribution of the global velocity for different distance dependent parameter  $a$ . For the discontinuous transition,  $U$  shows a strong discontinuity close to critical noise strength  $\eta_c(a)$ . The variation of  $V$  with time also shows switching between two states, and the probability distribution of the global velocity is bimodal for  $a \approx 1$ . However, for the continuous transition,  $V$  continuously varies from large to small values and  $U$  changes smoothly, and there is no switching behaviour in the global velocity time series, also the probability distribution of the global velocity is uni-modal.

We construct the phase diagram in the noise strength and the distance dependent parameter  $(\eta, a)$  plane. The nature of the disorder-to-order transition is first order for  $a \simeq 1$ , and it changes to continuous type with decreasing  $a$ , and at a tri-critical point the nature of the transition changes from discontinuous to continuous. Earlier studies of [130, 131] find that the disorder-to-order transition in polar flock can be mapped to the liquid-gas transition. In our study, we find that the density plays an important role and the large density inhomogeneity leads to the discontinuous transition in these systems. The effect of density is characterized by the phase separation order parameter  $\langle Q \rangle$  and the standard deviation in number of particles in unit sized sub-cells  $\langle \Delta\phi \rangle$  for different  $a$ . We find that the density phase separation is large for  $a \simeq 1$ , and it decays with decreasing  $a$ . Hence, the discontin-

uous disorder-to-order transition and the large density phase separation are common for  $a$  approaching to unity.

Our study concludes that the nature of the disorder-to-order transition in collection of polar flock is not always necessarily first order, and it strongly depends on the interaction amongst the particles. The study of [134] shows that the transition from random to collective motion changes from continuous to discontinuous with decreasing restriction angle. The critical noise amplitude also decreases monotonically on decreasing the restriction angle. In our model we propose a parameter  $a$ , which can also tune the nature of such transition. Our model would be useful to study the disorder-to-order transition in biological and granular systems, where interaction between close-by neighbours is stronger than the interaction of particles with other neighbours.

---

## SELF-PROPELLED PARTICLES WITH INHOMOGENEOUS QUENCHED SPEED

---

### 5.1 INTRODUCTION

Most of the natural systems where the particles show collective motion, contain different kind of inhomogeneities. Examples of these flocks range from a few micrometers to some kilometers. Bacteria shows collective behavior in different kind of inhomogeneous medium like the soil or inside a cell. On the other hand, flock of birds, fish schools, *etc.* show collective behavior upto a few meters. After introduction of the Vicsek model [57] there are numerous works, experimental as well as theoretical, about the active matter systems. Still little is known about the impact of different kind of inhomogeneities in the active systems. Recently, different steady state properties of the polar SPPs in inhomogeneous environments are addressed in many theoretical and experimental works [77–79, 82, 135], as we have already discussed in Sec. 1.3.

In natural systems, all the particles do not move with the same propulsion speed. In this chapter, we introduce a inhomogeneity in the self-propulsion speed of the polar SPPs. In the Vicsek model [57], the polar SPPs move with a constant propulsion speed  $v_0$ . But we consider that the polar SPPs move with different self-propulsion speed, and they maintain the speed during their motion. In this study, the self-propulsion speed of the polar SPPs are taken from a Gaussian distribution. The fluctuation in self-propulsion speed among the polar SPPs increases with the standard deviation  $\sigma$  of the Gaussian distribution.

We have organized this chapter as follows. We have defined the microscopic model in Sec. 5.2. Technique for simulating the microscopic model and appropriate system parameter are defined in the same section. In Sec. 5.3.1, we have discussed about the long-range ordering of the system for different standard deviation  $\sigma$  of the Gaussian distribution. We find that the long-range ordering of the system is independent of the self-propulsion speed fluctuation among the particles. In Sec. 5.3.2 we characterize the ordering dynamics of the system for different  $\sigma$  values. We note that the fluctuation in the self-propulsion speed among the SPPs helps the system to reach the steady state faster, as compared to the Vicsek model. We have also characterized different steady state properties like clustering, density phase separation, and information transfer in the system for finite speed fluctuation among the SPPs in Sec. 5.3.3. We note isolated cluster formation in the ordered state for small speed fluctuation among the SPPs, whereas for large speed fluctuation the system becomes homogeneous in the ordered state. In Sec. 5.3.3.2, we have studied the response of the system in the steady state to an external information. To study the system response, we have introduced some quenched (space and orientation) external agents in the steady state, and these external agents try to divert the flock to a new direction. We find that for larger fluctuation in self-propulsion speed among the SPPs response to the external agents is fast. Hence more inhomogeneous speed distribution introduces faster information transfer among the SPPs.

## 5.2 MODEL

We consider a collection of  $N$  polar SPPs moving on a substrate of size  $L \times L$  with periodic boundary conditions. During the motion, SPPs try to follow their neighbors and interact among themselves via short-range velocity alignment (ferromagnetic like) interaction [57]. The inhomogeneity in the system is introduced through the self-propulsion speed  $v_0$  of the SPPs. In this model, the pointlike SPPs move at discrete time  $\Delta t = 1$  with different self-propulsion speed  $v_0$  which are taken from a Gaussian (Normal) distribution of mean  $\mu = 0.3$  and standard deviation  $\sigma$ . We performed agent based numerical simulation. The standard deviation  $\sigma$  is to tune the speed fluctuation among the SPPs. But, each SPP maintain its

speed during the motion, *i.e.*, the self-propulsion speed of the SPPs is quenched to its initial value. We express the update equations of the SPPs as:

$$\mathbf{r}_i(t+1) = \mathbf{r}_i(t) + v_0^i \Delta t, \quad (5.1)$$

$$\mathbf{n}_i(t+1) = \frac{1}{W_i(t)} \left[ \sum_{j=1}^{N_R} \mathbf{n}_j(t) + N_R \eta_0 \boldsymbol{\eta} \right] \quad (5.2)$$

where  $\mathbf{r}_i(t)$  represents the position vector of the  $i^{\text{th}}$  particle on the substrate at time  $t$ , and  $v_0^i$  is the self-propulsion speed of the  $i^{\text{th}}$  particle which is taken from the Gaussian distribution.  $\mathbf{n}_i(t) = (\cos\theta_i(t), \sin\theta_i(t))$  is a unit direction vector of the  $i^{\text{th}}$  particle, which indicates particle direction of motion on the substrate. The direction of motion of the  $i^{\text{th}}$  particle is calculated from the previous direction vectors of all the particles inside its interaction range  $R = 1 (> v_0^i \Delta t)$  where  $N_R$  is the number of neighbors within  $R$ .  $\boldsymbol{\eta}$  is the random unit vector (noise) to incorporate the error made by the SPPs during following their neighbors, and  $\eta_0 \leq 1$  defines the strength of it. In our simulations, we consider the noise strength  $\eta_0 = 0.2$ . For this choice of  $\eta_0$ , the steady state is in the ordered state for all values of  $\sigma$ . To study the response of the flock to an external information, we introduce  $N_a$  external agents at  $t = t_0$  (in the steady state).  $\theta_a$  is the direction of the external agents. The density of the external agents is defined by  $\rho_a$ . The external agents are quenched in space, and they do not change the direction with time. But they change the direction of the flock to  $\theta_a$  through alignment interaction with the SPPs, as defined in Eqs. 5.1 and 5.2.

## 5.3 RESULTS

### 5.3.1 Long range ordering

We characterize the macroscopic collective behavior of the system by global orientation order parameter is defined as:

$$V = \frac{1}{N} \left| \sum_{i=1}^N \mathbf{n}_i \right|. \quad (5.3)$$

The study of Vicsek and his collaborators [57] find long-range ordered or broken-orientational-symmetry state in 2D for a collection polar SPPs moving with constant self-propulsion speed. In this study, we consider that the SPPs move with different self-propulsion speed which are taken from a Gaussian distribution with mean  $\mu = 0.3$  and standard deviation  $\sigma$ .  $\sigma$  is varied from 0.0 to 0.05. We are able to vary  $\sigma$  up to 0.05 beyond which the Gaussian distribution with  $\mu = 0.3$  will generate negative numbers, and the self-propulsion speed can not be negative. We have calculated the global orientation order parameter  $V$  for different  $\sigma$  values and find that  $V$  does not decay with the system sizes, as shown in Fig. 5.1. The non-decaying feature of the order parameter with  $\sigma$  suggests that the well-known long range ordered state in the polar systems is intact even in the presence of speed fluctuation among the SPPs.

### 5.3.2 Ordering to steady state

We study the effect of the speed fluctuation in the system. At the beginning, all the SPPs are homogeneously distributed on a substrate with random orientation. For different values of  $\sigma$ , the SPPs will form an ordered flock for noise strength  $\eta_0$  smaller than the critical noise strength. In our study we choose  $\eta_0$  such that the steady states are ordered flock for all  $\sigma$  values. The time required for the SPPs to reach the flock state decreases as we increase the standard deviation  $\sigma$ , as shown in Fig. 5.2. Therefore, the inhomogeneity in the self-propulsion speed of in the collection polar SPPs helps in faster ordering of the system.

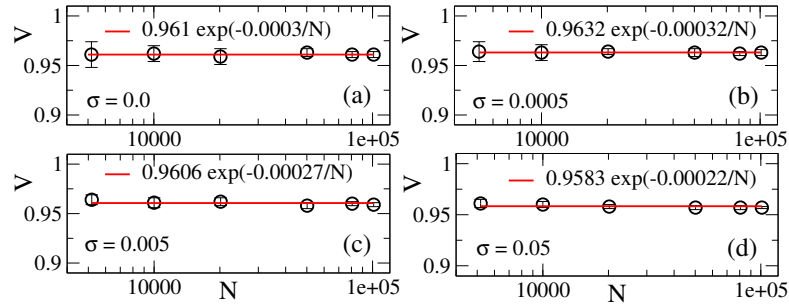


Figure 5.1: Plot of the global order parameter  $V$  with different system sizes  $N$  for four different values of  $\sigma$  (0.0, 0.0005, 0.005 and 0.05) are shown in (a-d), respectively. Black circles are numerical data and red line is exponential fitting of the numerical data points. We consider density of the system  $\rho = 1$ .

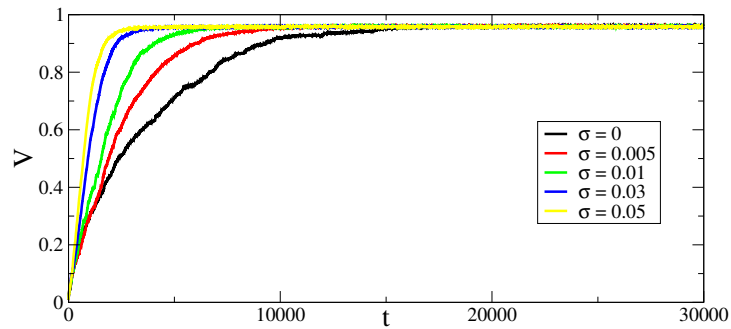


Figure 5.2: Plot of the global order parameter  $V$  time series for five different values of  $\sigma = 0, 0.005, 0.01, 0.03$  and  $0.05$ . We have considered  $224 \times 224$  system, and the mean density of the system  $\rho = 1$ .

### 5.3.3 Steady state features

#### 5.3.3.1 Clustering and density phase separation

We have shown snapshots of the system at the steady state for different values of  $\sigma$  in Fig. 5.3. As shown in Fig. 5.3, for  $\sigma = 0$  (VM) there are many isolated clusters in the steady state, whereas the isolated clusters gradually break down and form homogeneous state with increasing  $\sigma$ . Now to characterize the clustering behavior for different values of  $\sigma$ , we have calculated cluster size distribution at the steady state. We have calculated average number of particles  $N$  inside the interaction radius  $R$  for different values of  $\sigma$ , and it is defined as cluster size for the corresponding  $\sigma$ . We find that the probability distribution function (PDF) of the cluster  $P(N)$  shows exponential decay, as shown in Fig. 5.4. We also find a good scaling

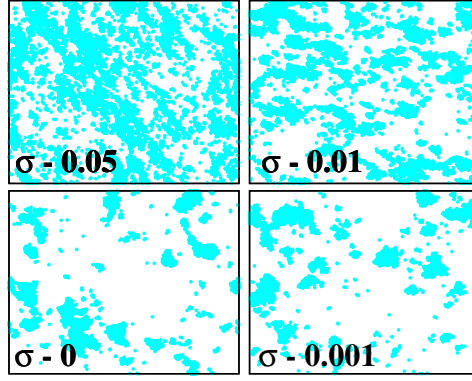


Figure 5.3: Snapshots of the system at steady state for different values of  $\sigma = 0.0, 0.001, 0.01$  and  $0.05$ . We have considered  $224 \times 224$  system and density  $\rho = 1$ .

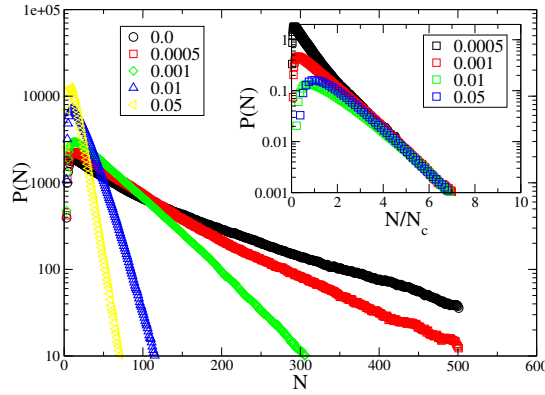


Figure 5.4: Plot of the probability distribution of the number of neighbors  $P(N)$  vs. number of neighbors  $N$  for different values of  $\sigma = (0, 0.0005, 0.001, 0.01)$  and  $0.05$ . Inset: Plot of  $P(N)$  vs. scaled number of neighbors  $N/N_c$ . We consider  $318 \times 318$  system size and density  $\rho = 1$ .

behavior of PDF  $P(N)$  with  $N/N_c$  for different  $\sigma$ , as shown in the inset of Fig. 5.4, where  $N_c$  is the critical number of particles inside the interaction radius  $R$  for different  $\sigma$ .

We have also characterized the density phase separation of the system in the steady state for different values of  $\sigma$ . We have divided the  $L \times L$  system into unit sized sub-cells and calculate the average number of particles in each sub-cell. Then we have calculated the standard deviation in particle number among the  $L^2$  sub-cells.

$$\langle \Delta\phi \rangle = \sqrt{\frac{1}{L^2} \sum_{j=1}^{L^2} (\phi_j)^2 - \left( \frac{1}{L^2} \sum_{j=1}^{L^2} \phi_j \right)^2}, \quad (5.4)$$

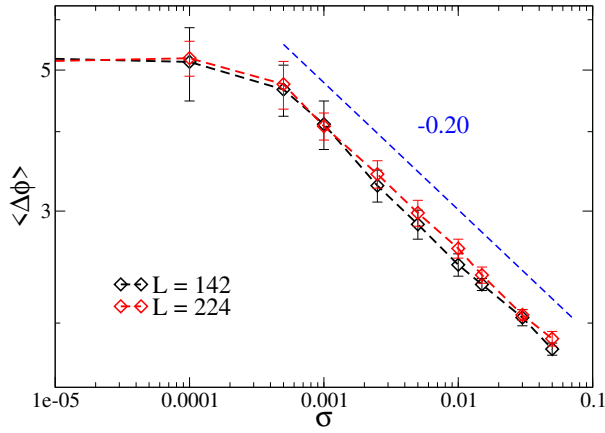


Figure 5.5: Plot of  $\langle \Delta \phi \rangle$  vs.  $\sigma$  for two different system sizes  $142 \times 142$  and  $224 \times 224$ . The dashed line represents slope of  $-0.20$ . We have considered density  $\rho = 1$ .

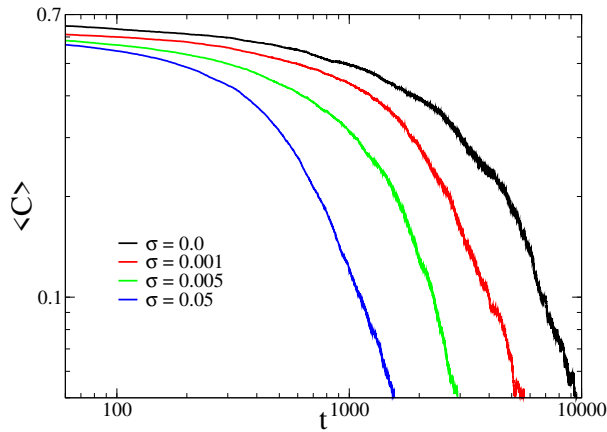


Figure 5.6: Plot of  $\langle C \rangle$  vs.  $t$  for different  $\sigma = 0, 0.001, 0.005$  and  $0.05$  of the Gaussian distribution. We have considered  $142 \times 142$  system size and the auto correlation is averaged over 20 ensembles. Density of the system  $\rho = 1$ .

where  $\phi_j$  is the number of particles in  $j^{\text{th}}$  sub-cell. We have calculated  $\phi_j$  at different time in the steady state. We note that the average standard deviation in particles number among the sub-cells  $\langle \Delta \phi \rangle$  shows power-law decay with  $\sigma$ , and for very small  $\sigma$  it saturates to a finite value, as shown in Fig. 5.5. The decay in  $\langle \Delta \phi \rangle$  with  $\sigma$  suggests that the system becomes homogeneous in the ordered state with increasing speed fluctuation among the SPPs.

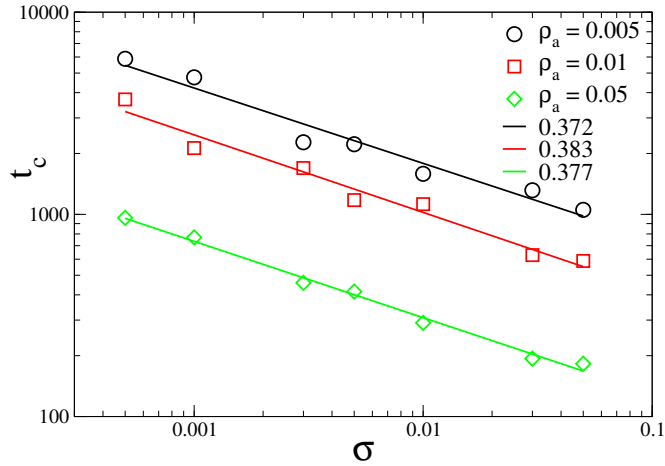


Figure 5.7: Plot of  $t_c$  vs.  $\sigma$  for different densities of the external agents  $\rho_a$ . We have considered three different external agent density ( $\rho_a = 0.005, 0.01$  and  $0.05$ ). We have consider  $142 \times 142$  system size and the  $t_c$  is averaged over 20 ensembles.

### 5.3.3.2 Response to external perturbation

In this study, we characterize the advantages of the speed fluctuation among the SPPs instead of considering the constant speed model. We have defined direction auto-correlation as:

$$\langle C \rangle = \langle \cos(\theta_i(t) - \theta_i(0)) \rangle - \langle \cos(\theta_a - \theta_i(0)) \rangle, \quad (5.5)$$

where  $\theta_i(t)$  and  $\theta_i(0)$  are the directions of the  $i^{\text{th}}$  particle at time  $t$  and at the time external agents are introduced, respectively.  $\theta_a$  is the orientation of the external agents.  $\langle \cdot \rangle$  represents average over all the SPPs and many realisations. We find that the auto-correlation function takes long time to decay for  $\sigma = 0$ , whereas it decays faster as we increase the value of  $\sigma$ , as shown in Fig. 5.6. Therefore, the system takes longer time to follow the external agents for the constant speed model, and the SPPs align faster towards the direction of the external agents if there is nonzero fluctuation in self-propulsion speed among them. The auto-correlation function shows exponential decay with time. The time taken by the SPPs to follow the external agents is defined as critical time  $t_c$  (when the auto-correlation function decays to zero) of the flock. We have considered three different density of the external agent ( $\rho_a = 0.005, 0.01$  and  $0.05$ ) and find that the response of SPPs does not change with the density of the external agent  $\rho_a$ , as shown in Fig. 5.7.

## 5.4 DISCUSSION

In summary, we have studied the steady state behavior of a collection of polar SPPs with fluctuation in self-propulsion speed among themselves. We find that the long range ordered state is present for any finite fluctuation in self-propulsion speed among the SPPs. We also find that finite speed fluctuation helps the system to reach to its steady state faster compare to the constant speed model like the Vicsek model. To ensure this behavior of the system, we introduce a few external agents in the system in the steady state. These external agents divert the direction of motion of the flock to their own direction. We study the response of the flock to the external agents for different values of  $\sigma$ . We find that the flock changes its direction faster with the increasing value of the speed fluctuation  $\sigma$ . The system forms isolated ordered clusters for constant speed model ( $\sigma = 0.0$ ), whereas the ordered state of the system becomes homogeneous as we increase the value of the speed fluctuation  $\sigma$ . This homogeneous ordered state helps in faster information transfer throughout the system. But for isolated clusters, there is a lack of information transfer among the clusters. Therefore, the fluctuation in self-propulsion speed among the SPPs helps in faster information transfer in the system. Recently, in an experimental study on unicellular eukaryotes, *e.g.*, flagellates and ciliates, Lisicki *et al.* [136] find that the probability distributions of swimming speed of these eukaryotes can be accurately represented by log-normal distributions. Hence, our study gives a comparison of constant speed vs. a distribution of of speed.

---

## A COMPARATIVE STUDY OF ORDERING KINETICS IN ACTIVE AND PASSIVE MODEL B

---

### 6.1 INTRODUCTION

Up to now in this thesis, we have discussed about the steady state properties of the active polar self-propelled particles in various boundary conditions in chapter 2 and 3, and also about bulk properties in chapter 4 and 5. The ordering kinetics of a system to a steady state is also an active area of research. As we have discussed in the introduction section 1.2.2, the ABPs shows motility induced phase separation without any alignment interaction beyond a critical packing fraction  $\Phi_c$ . In this study we have discussed about the kinetics of the ABPs towards the phase separated state. Also we study the role of different kind of noises (additive/multiplicative) in ordering kinetics of the ABPs.

For binary system (passive), one can describe the phase separation kinetics using conserved scalar order parameter field  $\psi$  or model B [36, 137], and this model is also known as Cahn-Hilliard model [137]. The order parameter field  $\psi$  is linearly related to the local density of the particles. The domain growth for this model varies as  $L_c(t) \sim t^{1/3}$ , as discusses in Sec. 1.5.2, where  $L_c(t)$  is the characteristic domain length at time  $t$ . Although there is a deep distinction in the phase separation between the active and the passive systems, still there is a partial mapping in the coarse-graining at the large scale between the two systems. Main difference between the passive and active systems is that the detailed balance is present in the former systems, whereas the detailed balance is violated by the latter one. In a recent study, Wittkowski *et al.* [112] introduce a gradient term  $\nabla\psi$  in the passive model B. This

gradient term is non-integrable, and it breaks the detailed balance in the passive model B. Therefore, the resulting model is known as active model B which can not be derived from any free energy functional. In this chapter we study the ordering kinetics in active model B and compare it with corresponding passive model B.

This chapter is organised as follows. We have studied the effect of the activity on the kinetics of a collection of ABPs for both critical and off-critical mixture in Sec. 6.3.1 and Sec. 6.3.2, respectively. For critical active model B, the domain growth exponent  $z = 4$  at late time (asymptotic limit), and the system takes larger and larger time to reach to the asymptotic limit with increasing activity. But, for the off-critical active model B the growth exponent is  $z \sim 3$ . We have also investigated the effect of noise, both additive and multiplicative, in active model B in Sec. 6.3.3. We find that the growth phenomena of active model B is independent of the noise and the nature of the noise.

## 6.2 MODEL

We consider a collection of randomly distributed active Brownian particles (ABPs) on a  $L \times L$  2D square lattice. Occupation number of any lattice point can take values 0(occupied) or 1(unoccupied). We map the system to a binary mixture: ABPs are one kind of species and void lattice points represent another kind. The conserved coarse-grained order parameter of the system is defined as,  $\psi(\mathbf{r}, t) = n^A(\mathbf{r}, t) - n^B(\mathbf{r}, t)$ , where  $n^\alpha(\mathbf{r}, t)$  is the local density of the species  $\alpha(A,B)$ . We introduce a gradient term in the Cahn-Hilliard (CH) equation, as discussed in Sec. 1.5.2.

$$\frac{\partial \psi(\mathbf{r}, t)}{\partial t} = \nabla \cdot \{ \nabla [-\psi(\mathbf{r}, t) + \psi(\mathbf{r}, t)^3 - \nabla^2 \psi(\mathbf{r}, t) - \lambda(\nabla \psi)^2] \} \quad (6.1)$$

The  $\psi$  and  $\psi^3$  terms in the right hand side represent the aggregation, and  $\nabla^2$  term is for the diffusion.  $\lambda$  is the activity parameter of the system. We use continuum time update with  $\Delta t = 0.01$ , and  $\Delta x = 1.0$  for the coarse-grained order parameter  $\psi$ . In our simulation we have varied the activity parameter  $\lambda$ .

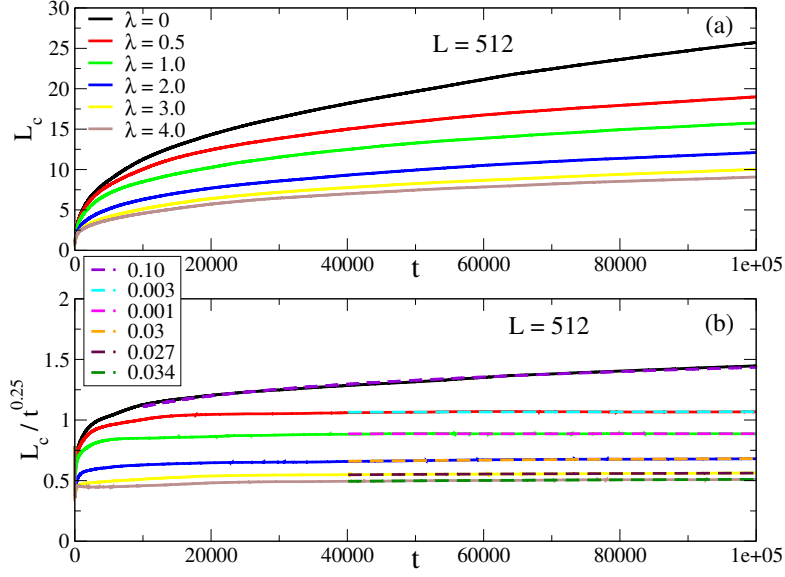


Figure 6.1: Upper panel: (a) Plot of the correlation length  $L_c$  vs. time  $t$  for different activity  $\lambda$ . Lower panel: (b) Plot of scaled  $L_c/t^{0.25}$  vs.  $t$  for different activity  $\lambda$ . The dashed line in the lower panel represents the slope of the  $L_c/t^{0.25}$  vs.  $t$  plot. We have considered  $512 \times 512$  system size, and  $L_c$  is averaged over 20 ensembles.

In the later part of this chapter, we have studied the effect of different kind of noises (thermal fluctuations) on the ordering kinetics of the ABPs. We have compared the effect of both additive and multiplicative noise. We consider the strength of the multiplicative noise  $\eta_m$  varies as  $\eta_m = (\frac{1+\psi(\mathbf{r},t)}{2})^{1/2}$ . The order parameter update equation Eq. 6.1 in presence of additive noise

$$\frac{\partial \psi(\mathbf{r}, t)}{\partial t} = \nabla \cdot \left\{ \nabla [-\psi(\mathbf{r}, t) + \psi(\mathbf{r}, t)^3 - \nabla^2 \psi(\mathbf{r}, t) - \lambda (\nabla \psi)^2] + \eta_a \mathbf{f} \right\}, \quad (6.2)$$

where  $\eta_a$  is the strength of the Gaussian white noise  $\mathbf{f}$  with mean zero and unit variance. Similarly the the update equation for  $\psi(\mathbf{r}, t)$  in presence of multiplicative noise

$$\frac{\partial \psi(\mathbf{r}, t)}{\partial t} = \nabla \cdot \left\{ \nabla [-\psi(\mathbf{r}, t) + \psi(\mathbf{r}, t)^3 - \nabla^2 \psi(\mathbf{r}, t) - \lambda (\nabla \psi)^2] + \left( \frac{1 + \psi(\mathbf{r}, t)}{2} \right)^{1/2} \eta_m \mathbf{f} \right\}, \quad (6.3)$$

where  $\eta_m$  is the strength of the Gaussian  $\mathbf{f}$  with noise with mean zero and unit variance.

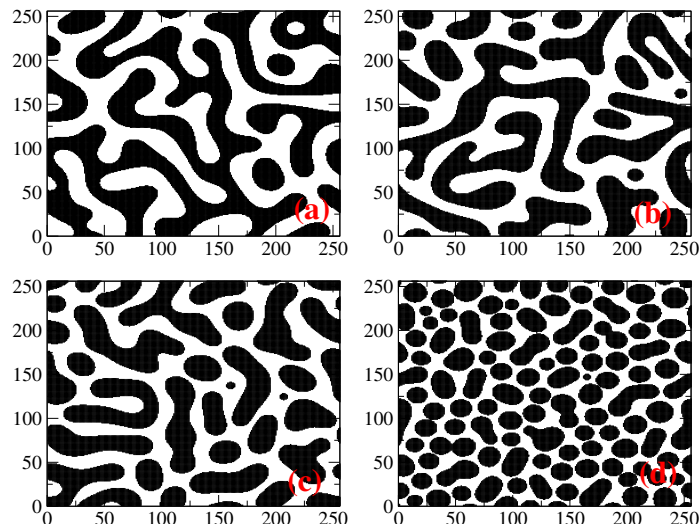


Figure 6.2: Plot of snapshots of the system at time  $t = 2000$  for the activity  $\lambda = 0$  (passive), 0.5, 1.0, 4.0 from (a-d), respectively. We have considered critical mixture  $\psi(\mathbf{r}, t)$  is 0.0, and system size is  $256 \times 256$ .

## 6.3 RESULTS

### 6.3.1 Critical active model B

#### 6.3.1.1 Domain growth

There will be formation of domains as the system approaches towards a steady state, and the size of these domains are characterized by a characteristic length  $L_c(t)$ . We consider  $512 \times 512$  lattice and the value of the order parameter  $\psi(\mathbf{r}, t)$  is zero for critical (symmetric) mixture. The activity parameter  $\lambda$  is varied from 0 (passive mixture) to 4.0. We find that the characteristic length of the domain  $L_c(t)$  decreases with the activity  $\lambda$ , as shown in Fig. 6.1 (a). To characterize the growth exponent  $z$  in the asymptotic limit, we have scaled  $L_c(t)$  with  $t^{0.25}$ . If the growth exponent  $z = 4$  then the  $L_c/t^{0.25}$  vs.  $t$  plot becomes flat at late time, whereas for the passive model B slope of the  $L_c/t^{0.25}$  vs.  $t \approx 0.08$  ( $z = 3$ ). We also note that the system takes longer time to reach to its asymptotic region for large activity. For non-zero  $\lambda$ , the bicontinuous domain of the passive binary mixture breaks into isolated domains, as shown in the snapshots 6.2. But for large  $\lambda$  size of these isolated domains is small compare

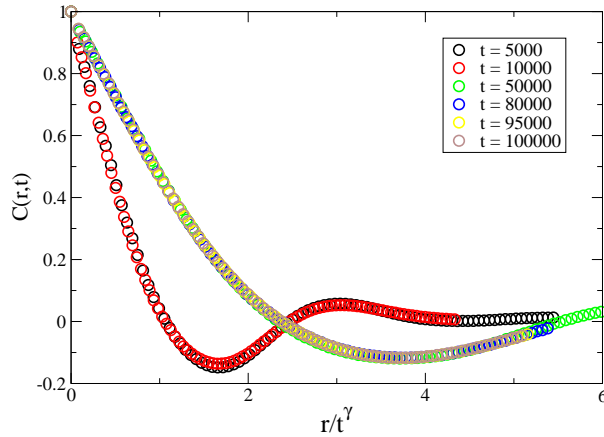


Figure 6.3: Plot of  $C(\mathbf{r}, t)$  vs.  $\mathbf{r}/t^\gamma$  at different times for  $\lambda = 1$ .  $\gamma = 1/3$  for  $t < 50000$  and  $\gamma = 1/4$  for  $t \geq 50000$ . We have considered  $256 \times 256$  system size, and  $C(\mathbf{r}, t)$  is averaged over 20 ensembles.

to its size for small  $\lambda$ . Therefore, the system takes longer time to reach to asymptotic limit for large  $\lambda$ .

#### 6.3.1.2 Correlation function

To characterize the domain morphology we have calculated the correlation function  $C(\mathbf{r}, t)$ , as defined in Sec. 1.5.3. For  $\lambda = 1.0$ , we find that the early time correlation function scales with  $t^{0.33}$ , whereas the correlation functions  $C(\mathbf{r}, t)$  at late time scales with  $t^{0.25}$ , as shown in Fig. 6.3. Therefore, for any non-zero activity the early time growth exponent is  $z = 3$  and it changes to 4 at the asymptotic limit. We have shown the correlation functions  $C(\mathbf{r}, t)$  at different time for passive  $\lambda = 0$  and active  $\lambda = 1.0$  binary mixture in Fig. 6.4 (a) and (c), respectively. We find that a dynamical scaling of the correlation function for both active and passive models, as shown in Figs. 6.4 (b) and 6.4 (d). We have also shown the correlation function at time  $t = 10^5$  for different activity  $\lambda$  in Fig. 6.5 (a). We find that the static scaling of the correlation function  $C(\mathbf{r}, t)$  is not good with the activity  $\lambda$ .

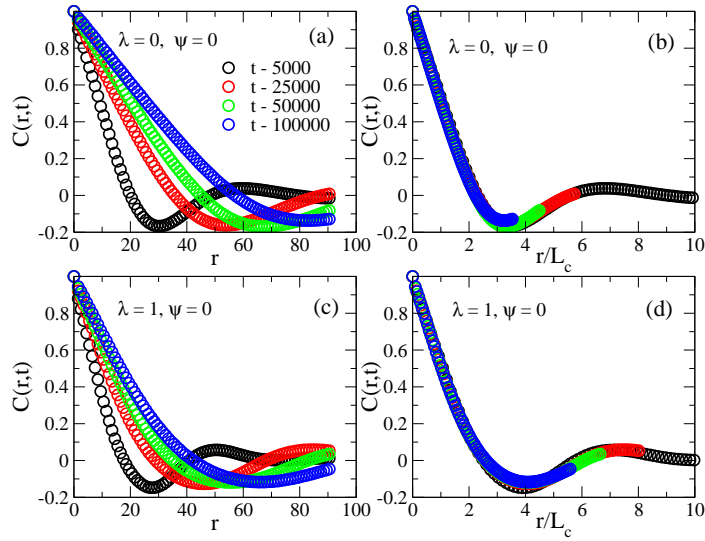


Figure 6.4: Upper panel: Plot of  $C(\mathbf{r}, t)$  vs.  $\mathbf{r}$ , and  $C(\mathbf{r}, t)$  vs.  $\mathbf{r}/L_c$  for  $\lambda = 0$  are shown in (a) and (b), respectively. Lower panel: Plot of  $C(\mathbf{r}, t)$  vs.  $\mathbf{r}$ , and  $C(\mathbf{r}, t)$  vs.  $\mathbf{r}/L_c$  for  $\lambda = 1.0$  are shown in (a) and (b), respectively. We have considered  $256 \times 256$  system size and number of realizations is 20.

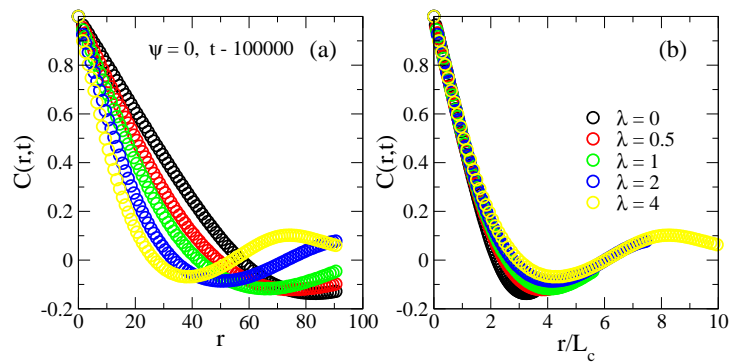


Figure 6.5: Plot of  $C(\mathbf{r}, t)$  vs.  $\mathbf{r}$  at  $t = 10^5$  for different  $\lambda$  is shown in (a). Plot of  $C(\mathbf{r}, t)$  vs.  $\mathbf{r}/L_c$  at  $t = 10^5$  for different  $\lambda$  is shown in (b). We have considered  $256 \times 256$  system size and number of realizations is 20.

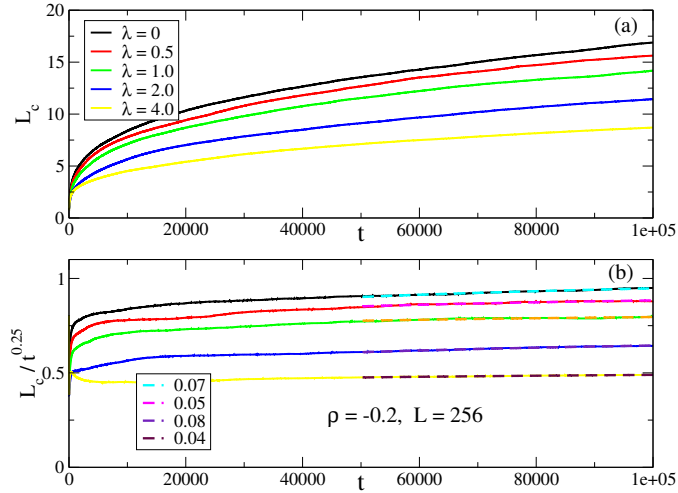


Figure 6.6: Upper panel: (a) Plot of the correlation length  $L_c$  vs. time  $t$  for different activity  $\lambda$ . Lower panel: (b) Plot of scaled  $L_c/t^{0.25}$  vs.  $t$  for different activity  $\lambda$ . The dashed line in the lower panel represents the slope of the  $L_c/t^{0.25}$  vs.  $t$  plot. We have considered  $256 \times 256$  system size, and  $L_c$  is averaged over 20 ensembles.

### 6.3.2 Off-critical model B

#### 6.3.2.1 Domain growth

In previous Sec. 6.3.1, we have discussed about critical mixture where half of the total area of the system is occupied by the ABPs. In this section, we will discuss about the system where less than half of the lattice points is occupied by the ABPs. The dynamics of this kind of system can be studied by the off-critical binary mixture. However, the morphology of the system is characterized by the minority phase (ABPs) droplets. We consider the value of the conserved order parameter  $\psi(\mathbf{r}, t) = -0.2$  (40% – 60% mixture) which suggests that the 40% of the lattice points are occupied by the ABPs. Similar to the critical mixture, we have studied the domain growth using the Eq. 6.1. In our numerical study, we consider  $256 \times 256$  system and varied the value of  $\lambda$ . We find that the characteristic length of the domain decreases with the  $\lambda$ , as shown in Fig. 6.6 (a). We also characterize the growth exponent  $z$  for different activity  $\lambda$  in Fig. 6.6 (b). At late time the growth exponent  $z \sim 3$ . We also note that the asymptotic value of  $z$  for small off-criticality  $\sim 4$ , and its value approaches towards 3 with increasing the off-criticality (data not shown). We characterize the domain morphology of the off-critical mixture by calculating the dynamical correlation function  $C(\mathbf{r}, t)$ , as defined

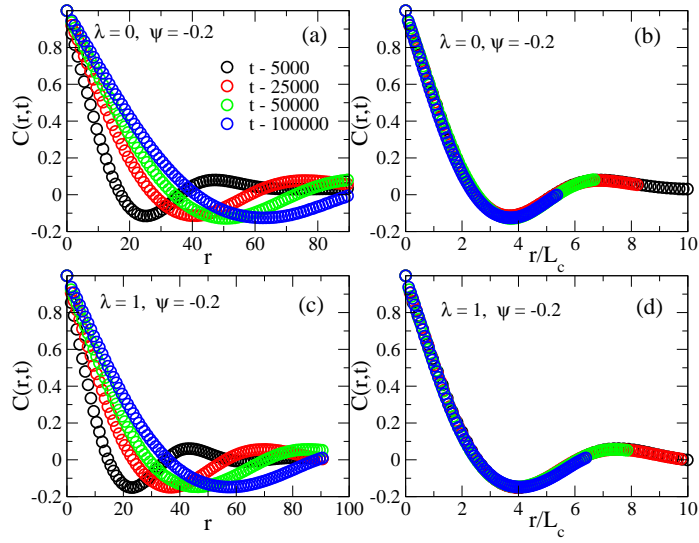


Figure 6.7: Plot of  $C(\mathbf{r}, t)$  vs.  $\mathbf{r}$  for  $\lambda = 0$  and  $1$  are shown in (a) and (c), respectively. Plot of  $C(\mathbf{r}, t)$  vs.  $\mathbf{r}/L_c$  for  $\lambda = 0$  and  $1$  are shown in (b) and (d), respectively, where  $L_c$  is average correlation length. We have considered  $256 \times 256$  system size and number of realizations is 20. The order parameter value is  $-0.2$ , which gives 40:60 off-critical mixture.

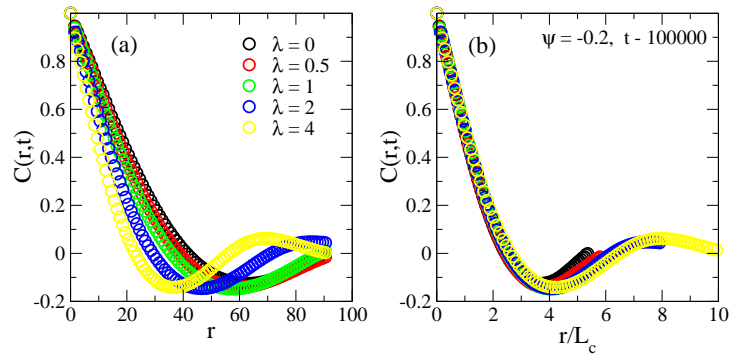


Figure 6.8: Plot of  $C(\mathbf{r}, t)$  vs.  $\mathbf{r}$  at  $t = 10^5$  for different  $\lambda$  is shown in (a). Plot of  $C(\mathbf{r}, t)$  vs.  $\mathbf{r}/L_c$  at  $t = 10^5$  for different  $\lambda$  is shown in (b), where  $L_c$  is average correlation length. We have considered  $256 \times 256$  system size and number of realizations is 20. The order parameter  $\psi(\mathbf{r}, t)$  is  $-0.2$ .

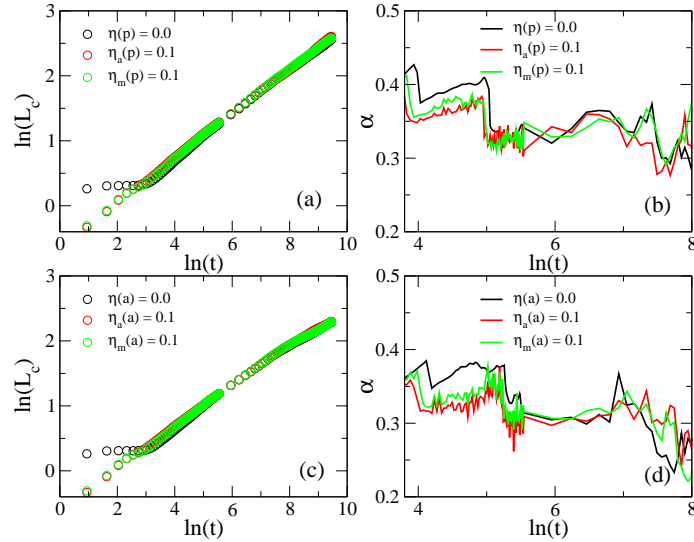


Figure 6.9: Plot of  $\ln(L_c)$  vs.  $\ln(t)$  and  $\alpha$  vs.  $\ln(t)$  for noise free  $\eta(p) = 0.0$ , additive  $\eta_a(p) = 0.1$  and multiplicative  $\eta_m(p) = 0.1$  noise in passive model B are shown in (a) and (b) respectively. Plot of  $\ln(L_c)$  vs.  $\ln(t)$  and  $\alpha$  vs.  $\ln(t)$  for noise free  $\eta(a) = 0.0$ , additive  $\eta_a(a) = 0.1$  and multiplicative  $\eta_m(a) = 0.1$  noise in active model B are shown in (c) and (d) respectively. Here for active model B we consider the  $\lambda = 1.0$ . For all cases correlation length  $L_c$  is averaged over five ensembles, and system size is  $256 \times 256$ .

in Sec. 1.5.3. We have shown the plot of  $C(\mathbf{r}, t)$  vs.  $r$  at different time for both passive ( $\lambda = 0$ ) and active ( $\lambda = 1.0$ ) cases in Fig. 6.7 (a) and (c), respectively. We have also shown the scaling of the correlation function for both  $\lambda = 0$  and 1 in Fig. 6.7 (b) and (d), respectively. We find that both passive and active off-critical mixture shows a good dynamical scaling. Moreover, we have shown the static scaling of correlation function with activity  $\lambda$ , as shown in Fig. 6.8. We note that the correlation functions for different  $\lambda$  show relatively good scaling for off-critical mixture compare to the critical one.

### 6.3.3 Effect of noise

In this section we will discuss about the effect of thermal fluctuations using an additive noise, as discussed in Eq. 6.2. The ABPs show motility induced phase separation and the fluctuation in order parameter depends on the local density. Therefore, it is suitable to consider the fluctuations in form of multiplicative noise, as the strength of the multiplicative noise depends of the local density, as discussed in Eq. 6.3. To characterize the growth behavior

for different kind of noises, we have define the growth exponent  $\frac{1}{z} = \alpha = \frac{d \ln(L_c)}{d \ln(t)}$ , where  $L_c$  the characteristic length of the domain. We have shown the variation of  $\alpha$  for noise free, additive and multiplicative noise for passive critical mixture in Fig. 6.9 (a) and for active critical mixture in Fig. 6.9 (b). We find that the late time exponent is independent of the type of noise.

#### 6.4 DISCUSSION

In this chapter we have studied the phase separation dynamics of the ABPs considering the dynamics of the conserved order parameter. We consider two different kind of mixtures: a) critical mixture- the ABPs occupy half of the total area of the system, and b) off-critical mixture- the ABPs occupy less than half of the area of the system. Previous study of Witkowski *et al.* find that the growth exponent for the active model B depends on the activity parameter  $\lambda$ . The growth dynamics becomes slow as we increase the activity of the ABPs for both critical and off-critical mixture [112]. But in our study, we find that the growth exponent is independent of the activity of the ABPs for both critical and off-critical mixture. We also find that the asymptotic value of the growth exponent is  $z = 4$  for critical mixture, and the system takes more time to reach to the asymptotic limit for the larger activity of the ABPs. On the other hand, for off-critical mixture value of the growth exponent at the asymptotic limit is  $z \sim 3$ . We find good dynamical scaling for both critical and off-critical mixture. We also note that the correlation functions of the off-critical mixture show a relatively good scaling with activity, where as the correlation functions of the critical mixture does not show scaling behavior with activity. We also studied the domain morphology for additive and multiplicative noise and find that the domain morphology does not change in presence of noise, and the growth exponent is independent of type of the noise.

---

## CONCLUSION

---

In this chapter, we provide a brief summary and concluding remarks on all the studies discussed so far. In Chapter 2, we have discussed about the collective behavior of a collection of polar SPPs in a narrow confined channel. We consider the channel with antiparallel orientation at the two boundaries which mimics the shear. Also the SPPs interact among them through alignment interaction. In this work, we have written the phenomenological hydrodynamical equations of motion of the density and the local polarization field for the collection of the polar SPPs. The anti-parallel orientation at the boundaries impose a gradient of orientation along the vertical direction (confinement) of the channel, and the alignment interaction among the SPPs try to make them parallel. Due to the competition between these two terms, we find formation of a periodic pattern of the orientation field along the channel for zero activity of the particles. Non-zero activity of the SPPs induces an active current which is proportional to the local polarization field. Such active current creates density inhomogeneity inside the channel. The density inhomogeneity becomes large beyond a certain width of the channel, and the rolls start to move. Formation of the travelling periodic rolls is similar to the Rayleigh-Bénard (RB) convection in fluids. The gradient in orientation plays similar to the temperature gradient of the RB convection, and the alignment is like gravity which acts opposite to the gradient. In Chapter 3, we have studied dynamics of an ABP on a 2D substrate with periodic arrangement of obstacles, and in a quasi-one-dimensional corrugated channel. We find that the periodic arrangement of the obstacles induces a directionality in ABP motion. We also note that the ABP shows effective one directional motion for high packing fraction of the obstacles. Motivated by the induced directional motion of the

ABP, we have studied the motion of the ABP in a quasi-one-dimensional corrugated channel. The ABP performs a super-diffusive dynamics over a long time in the corrugated channel without any external drive. This makes our study different from the previous studies where net transport of the ABP is observed in the presence of asymmetric potential [89] or using potential modulation in a corrugated channel [90]. We note that the net transport of the particle does not depend on the shape of the corrugated wall. However, the ABP shows diffusive dynamics in a channel with flat boundary.

Up to now, we have discussed about the effects of confinement in the dynamics of a collection of active particles, and on a single active particle. In Chapter 4, we have studied the bulk properties of a collection of polar SPPs on a 2D substrate. In 1995, Vicsek *et al.* find that these systems show a phase transition from randomly oriented disordered state (zero global velocity) to a ordered state (finite global velocity) depending on the different system parameters like density and noise strength [57]. The particle interacts with the neighbors inside its interaction range through an alignment interaction. There is a long debate about the nature of the order-disorder phase transition in the systems with polar SPPs. In this chapter, we have studied that how does the nature of the transition depends on the system parameters? We have introduced a distance dependent alignment interaction among the particles, and the interaction is always short range. The particle will follow more its nearest neighbors compare to the other neighbors inside the interaction range. We conclude that the nature of the disorder to order state transition in a collection of polar SPPs is strongly depends on the interaction amongst the particles. We note that the nature of the transition changes with the strength of the interaction with its neighbors. A similar study of [134] shows that the the transition from random to collective motion changes from continuous to discontinuous with decreasing restriction angle. In the Chapter 4, all the SPPs move with a constant self-propulsion speed. But in natural systems, there is a inhomogeneity in the self-propulsion speed in a collection of SPPs. In Chapter 5, we have considered inhomogeneous self-propulsion speed of the SPPs. We have varied the fluctuation in self-propulsion speed among the SPPs and find that the long range ordering behavior of these systems is independent of the speed fluctuation among them. We also note that the finite speed fluctuation helps the system to reach to its steady state faster compare to the constant speed model like the Vicsek model. Due to speed

inhomogeneity among the particles the ordered state of the system becomes homogeneous which helps faster information transfer in the system, whereas for zero speed fluctuation the system forms isolated clusters in the ordered state which slows down the information transfer. Recently in an experimental study on unicellular eukaryotes, e.g., flagellates and ciliates Lisicki *et al.* [136] find that the probability distributions of the swimming speed of these eukaryotes can be accurately represented by log-normal distributions. Therefore, our study gives a comparison between constant speed model vs. a model with Gaussian speed distribution.

We have discussed about the different steady state properties of the active particles using various boundary conditions in chapter 2, 3, and also about the bulk properties in Chapter 4, 5. In Chapter 6, we have discussed about the ordering kinetics of a collection of ABPs. We consider the ABPs on a 2D lattice and studied their phase separation dynamics using active model B. We consider two different kind of mixtures: a) critical mixture- the ABPs occupy half of the total area of the system, and b) off-critical mixture- the ABPs occupy less than half of the area of the system. Previous study of Wittkowski *et al.* [112] find that the growth exponent for the active model B depends on the activity parameter  $\lambda$ . But, we find that for both critical and off-critical mixture the growth exponent of the active model B is independent of the activity of the particles. We also find that the asymptotic value of the growth exponent is  $z = 4$  for critical mixture, and the system takes more time to reach to the asymptotic limit for the larger activity of the ABPs. On the other hand, for off-critical mixture value of the growth exponent at the asymptotic limit is  $z \sim 3$ . We find a good dynamical scaling for both critical and off-critical mixture. We also note that the correlation functions of the off-critical mixture show a relatively good scaling with activity, where as the correlation functions of the critical mixture does not show scaling behavior with activity. Furthermore, We have studied the domain morphology in presence of additive and multiplicative noise, and we find that the domain morphology does not change in presence of noise, and the growth exponent is independent of type of the noise.

---

## BIBLIOGRAPHY

---

- <sup>1</sup>L. D. Landau and E. M. Lifshitz, *Statistical physics i-ii* (Pergamon Press, Oxford, 1989) (cit. on pp. 1–3).
- <sup>2</sup>K. Huang, *Statistical mechanics* (Wiley, NY, 1987) (cit. on pp. 1, 2, 12).
- <sup>3</sup>R. K. Pathria, *Statistical mechanics*, English, 2nd ed. (Butterworth-Heinemann Oxford ; Boston, 1996), xiv, 529 p. : (cit. on pp. 1–3, 12).
- <sup>4</sup>M. W. Zemansky, *Heat and thermodynamics; an intermediate textbook [by] mark w. zemansky*, English, 5th ed. (McGraw-Hill New York, 1968), xx, 658 p. (Cit. on pp. 1, 3).
- <sup>5</sup>B. J. K, *Statistical Mechanics: An Introductory Text* (Allied Publishers Limited, 20000) (cit. on p. 2).
- <sup>6</sup>H. Stanley, *Introduction to phase transitions and critical phenomena*, International series of monographs on physics (Oxford University Press, 1971) (cit. on p. 2).
- <sup>7</sup>P. Meakin "*phase transitions and critical phenomena*", (Academic press, New work, 1987)(cit.onp. 2).
- <sup>8</sup>Alberts B, Johnson A, *Molecular biology of the cell* (Garland Sci., New York, 2002) (cit. on p. 2).
- <sup>9</sup>T. Surrey, F. Nédélec, S. Leibler, and E. Karsenti, "Physical properties determining self-organization of motors and microtubules," *Science* **292**, 1167–1171 (2001) (cit. on pp. 2, 3).
- <sup>10</sup>J. K. Parrish and W. M. Hamner, *Animal groups in three dimensions : how species aggregate* (CAMBRIDGE UNIVERSITY PRESS, 2015), p. 402 (cit. on p. 2).
- <sup>11</sup>B. Szabó, G. J. Szöllösi, B. Gönci, Z. Jurányi, D. Selmeczi, and T. Vicsek, "Phase transition in the collective migration of tissue cells: experiment and model," *Physical Review E* **74**, 061908 (2006) (cit. on p. 2).

- <sup>12</sup>C. Dombrowski, L. Cisneros, S. Chatkaew, R. E. Goldstein, and J. O. Kessler, “Self-concentration and large-scale coherence in bacterial dynamics,” *Phys. Rev. Lett.* **93**, 098103 (2004) (cit. on pp. 2, 3, 5).
- <sup>13</sup>PM Bendix, GH Koenderink, “A quantitative analysis of contractility in active cytoskeletal protein networks,” *Biophys J* **94**, 3126–36 (2008) (cit. on pp. 2, 5).
- <sup>14</sup>S. Rafai, L. Jibuti, and P. Peyla, “Effective viscosity of microswimmer suspensions,” *Phys. Rev. Lett.* **104**, 098102 (2010) (cit. on p. 2).
- <sup>15</sup>F. Peruani, J. Starruß, V. Jakovljevic, L. Søgaard-Andersen, A. Deutsch, and M. Bär, “Collective motion and nonequilibrium cluster formation in colonies of gliding bacteria,” *Physical Review Letters* **108**, 098102 (2012) (cit. on p. 2).
- <sup>16</sup>Y. Sumino, K. H. Nagai, Y. Shitaka, D. Tanaka, K. Yoshikawa, H. Chaté, and K. Oiwa, “Large-scale vortex lattice emerging from collectively moving microtubules,” *Nature* **483**, 448–452 (2012) (cit. on p. 2).
- <sup>17</sup>P. Nelson, *Biological physics: energy, information, life* (Freeman, New York, 2003) (cit. on p. 3).
- <sup>18</sup>J. K. R. Phillips and J Theriot, *Physical biology of the cell* (Garland Sci., New York, 2008) (cit. on p. 3).
- <sup>19</sup>M. C. Marchetti, J. F. Joanny, S. Ramaswamy, T. B. Liverpool, J. Prost, M. Rao, and R. A. Simha, “Hydrodynamics of soft active matter,” *Review of Modern Physics* **85**, 1143–1189 (2013) (cit. on pp. 3, 7, 22, 24, 38).
- <sup>20</sup>J. Toner, Y. Tu, and S. Ramaswamy, “Hydrodynamics and phases of flocks,” *Annals of Physics* **318**, Special Issue, 170 –244 (2005) (cit. on pp. 3, 4, 21, 24).
- <sup>21</sup>S. Ramaswamy, “The mechanics and statistics of active matter,” *Annual Review of Condensed Matter Physics* **1**, 323–345 (2010) (cit. on pp. 3, 7, 22, 24, 38).
- <sup>22</sup>T. Vicsek and A. Zafeiris, “Collective motion,” *Physics Reports* **517**, Collective motion, 71 –140 (2012) (cit. on pp. 3, 24).
- <sup>23</sup>M. E. Cates, “Diffusive transport without detailed balance in motile bacteria: does microbiology need statistical physics?” *Reports on Progress in Physics* **75**, 042601 (2012) (cit. on p. 3).

- <sup>24</sup>C. A. Yates, R. Baker, R. Erban, and P. Maini, “Refining self-propelled particle models for collective behaviour,” *Canadian Applied Maths Quarterly* **18** (2011) (cit. on p. 3).
- <sup>25</sup>S. Ramaswamy, “Active matter,” *Journal of Statistical Mechanics: Theory and Experiment* **2017**, 054002 (2017) (cit. on p. 3).
- <sup>26</sup>M. E. Cates and J. Tailleur, “Motility-induced phase separation,” *Annual Review of Condensed Matter Physics* **6**, 219–244 (2015) (cit. on pp. 3, 38).
- <sup>27</sup>A. Bricard, J.-B. Caussin, N. Desreumaux, O. Dauchot, and D. Bartolo, “Emergence of macroscopic directed motion in populations of motile colloids,” *Nature* **503**, 95 EP – (2013) (cit. on p. 3).
- <sup>28</sup>I. Theurkauff, C. Cottin-Bizonne, J. Palacci, C. Ybert, and L. Bocquet, “Dynamic clustering in active colloidal suspensions with chemical signaling,” *Physical Review Letters* **108**, 268303 (2012) (cit. on p. 3).
- <sup>29</sup>J. Deseigne, O. Dauchot, and H. Chaté, “Collective motion of vibrated polar disks,” *Physical Review Letters* **105**, 098001 (2010) (cit. on pp. 3, 4, 17).
- <sup>30</sup>V. Narayan, N. Menon, and S. Ramaswamy, “Nonequilibrium steady states in a vibrated-rod monolayer: tetratic, nematic, and smectic correlations,” *Journal of Statistical Mechanics: Theory and Experiment* **1**, 01005 (2006), eprint: [cond-mat/0510082](https://arxiv.org/abs/cond-mat/0510082) (cit. on p. 3).
- <sup>31</sup>V. Narayan, S. Ramaswamy, and N. Menon, “Long-lived giant number fluctuations in a swarming granular nematic,” *Science* **317**, 105–108 (2007) (cit. on pp. 3, 4, 7, 17).
- <sup>32</sup>D. L. Blair, T. Neicu, and A. Kudrolli, “Vortices in vibrated granular rods,” *Physical Review E* **67**, 031303 (2003) (cit. on pp. 3, 9).
- <sup>33</sup>N. Kumar, H. Soni, S. Ramaswamy, and A. K. Sood, “Flocking at a distance in active granular matter,” *Nature Communications* **5**, Article, 4688 EP – (2014) (cit. on p. 3).
- <sup>34</sup>W. F. Paxton, K. C. Kistler, C. C. Olmeda, A. Sen, S. K. St. Angelo, Y. Cao, T. E. Mallouk, P. E. Lammert, and V. H. Crespi, “Catalytic nanomotors: autonomous movement of striped nanorods,” *Journal of the American Chemical Society* **126**, 13424–13431 (2004) (cit. on pp. 3, 5, 9).
- <sup>35</sup>K. Huang, *Statistical mechanics*, 2nd ed. (John Wiley & Sons, 1987) (cit. on p. 3).

- <sup>36</sup>P. M. Chaikin and T. C. Lubensky, *Principles of condensed matter physics* (Cambridge University Press, 1995) (cit. on pp. 3, 14, 77).
- <sup>37</sup>R. Kemkemer, D. Kling, D. Kaufmann, and H. Gruler, “Elastic properties of nematoid arrangements formed by amoeboid cells,” *European Physical Journal E* **1** (2000) epje/v1/p215(e9284) (cit. on p. 3).
- <sup>38</sup>I. D. Couzin, J. Krause, N. R. Franks, and S. A. Levin, “Effective leadership and decision-making in animal groups on the move,” *Nature* **433**, 513–516 (2005) (cit. on pp. 3, 5).
- <sup>39</sup>U. Lopez, J. Gautrais, I. D. Couzin, and G. Theraulaz, “From behavioural analyses to models of collective motion in fish schools,” *Interface Focus* **2**, 693–707 (2012) (cit. on p. 3).
- <sup>40</sup>J. Werfel, K. Petersen, and R. Nagpal, “Designing collective behavior in a termite-inspired robot construction team,” *Science* **343**, 754–758 (2014) (cit. on p. 3).
- <sup>41</sup>G. P. Saracco, G. Gonnella, D. Marenduzzo, and E. Orlandini, “Shearing self-propelled suspensions: arrest of coarsening and suppression of giant density fluctuations,” *Phys. Rev. E* **84**, 031930 (2011) (cit. on pp. 3, 24, 32).
- <sup>42</sup>G. P. Saracco, G. Gonnella, D. Marenduzzo, and E. Orlandini, “Equilibrium and dynamical behavior in the vicsek model for self-propelled particles under shear,” *Central European Journal of Physics* **10**, 1109–1115 (2012) (cit. on pp. 3, 24, 32).
- <sup>43</sup>V. Balakrishnan, *Elements of nonequilibrium statistical mechanics*, English (CRC Press, 2008), p. 314 (cit. on p. 3).
- <sup>44</sup>G. Szamel, “Self-propelled particle in an external potential: existence of an effective temperature,” *Physical Review E* **90**, 012111 (2014) (cit. on p. 4).
- <sup>45</sup>D. Loi, S. Mossa, and L. F. Cugliandolo, “Effective temperature of active matter,” *Physical Review E* **77**, 051111 (2008) (cit. on p. 4).
- <sup>46</sup>T. Speck, J. Bialké, A. M. Menzel, and H. Löwen, “Effective cahn-hilliard equation for the phase separation of active brownian particles,” *Physical Review Letters* **112**, 218304 (2014) (cit. on p. 4).
- <sup>47</sup>J. Tailleur and M. E. Cates, “Statistical mechanics of interacting run-and-tumble bacteria,” *Physical Review Letters* **100**, 218103 (2008) (cit. on pp. 4, 7, 38).

- <sup>48</sup>T. Speck, “Stochastic thermodynamics for active matter,” *Europhysics Letters* **114**, 30006 (2016) (cit. on p. 4).
- <sup>49</sup>E. Fodor, C. Nardini, M. E. Cates, J. Tailleur, P. Visco, and F. van Wijland, “How far from equilibrium is active matter?” *Physical Review Letters* **117**, 038103 (2016) (cit. on p. 4).
- <sup>50</sup>S. Ramaswamy, R. A. Simha, and J. Toner, “Active nematics on a substrate: giant number fluctuations and long-time tails,” *Europhysics Letters* **62**, 196 (2003) (cit. on pp. 4, 7, 59).
- <sup>51</sup>D. K. C. Wolgemuth, E. Hoiczyk, and G. Oster, “How myxobacteria glide,” *Curr Biol.* **5**, 369–77 (cit. on p. 4).
- <sup>52</sup>J. Toner and Y. Tu, “Flocks, herds, and schools: a quantitative theory of flocking,” *Physical Review E* **58**, 4828–4858 (1998) (cit. on pp. 4, 6, 13, 16, 38, 61).
- <sup>53</sup>D. Yamada, T. Hondou, and M. Sano, “Coherent dynamics of an asymmetric particle in a vertically vibrating bed,” *Physical Review E* **67**, 040301 (2003) (cit. on pp. 4, 9).
- <sup>54</sup>A. Kudrolli, G. Lumay, D. Volfson, and L. S. Tsimring, “Swarming and swirling in self-propelled polar granular rods,” *Physical Review Letters* **100**, 058001 (2008) (cit. on p. 4).
- <sup>55</sup>“Fluid dynamics and noise in bacterial cell-cell and cell-surface scattering,” *Proc Natl Acad Sci* **108**, 10940 (2011) (cit. on p. 5).
- <sup>56</sup>T. B. Liverpool, “Anomalous fluctuations of active polar filaments,” *Phys. Rev. E* **67**, 031909 (2003) (cit. on p. 5).
- <sup>57</sup>T. Vicsek, A. Czirók, E. Ben-Jacob, I. Cohen, and O. Shochet, “Novel type of phase transition in a system of self-driven particles,” *Physical Review Letters* **75**, 1226–1229 (1995) (cit. on pp. 5–7, 9–11, 21, 22, 38, 51, 54, 66, 68, 69, 71, 88).
- <sup>58</sup>J. Palacci, B. Abécassis, C. Cottin-Bizonne, C. Ybert, and L. Bocquet, “Colloidal motility and pattern formation under rectified diffusiophoresis,” *Phys. Rev. Lett.* **104**, 138302 (2010) (cit. on p. 5).
- <sup>59</sup>D. J. T. Sumpter, J. Krause, R. James, I. D. Couzin, and A. J. W. Ward, “Consensus decision making by fish,” *Current Biology* **18**, 1773–1777 (2008) (cit. on p. 5).

- <sup>60</sup>J. W. Jolles, N. J. Boogert, V. H. Sridhar, I. D. Couzin, and A. Manica, “Consistent individual differences drive collective behavior and group functioning of schooling fish,” *Current Biology* **27**, 2862–2868.e7 (2017) (cit. on p. 5).
- <sup>61</sup>A. Ahmadi, T. B. Liverpool, and M. C. Marchetti, “Nematic and polar order in active filament solutions,” *Phys. Rev. E* **72**, 060901 (2005) (cit. on p. 5).
- <sup>62</sup>A. Ahmadi, M. C. Marchetti, and T. B. Liverpool, “Hydrodynamics of isotropic and liquid crystalline active polymer solutions,” *Phys. Rev. E* **74**, 061913 (2006) (cit. on p. 5).
- <sup>63</sup>J. Toner and Y. Tu, “Long-range order in a two-dimensional dynamical XY model: how birds fly together,” *Physical Review Letters* **75**, 4326–4329 (1995) (cit. on pp. 6, 13, 16, 38, 61).
- <sup>64</sup>E. Bertin, M. Droz, and G. Grégoire, “Boltzmann and hydrodynamic description for self-propelled particles,” *Physical Review E* **74**, 022101 (2006) (cit. on pp. 7, 9, 15, 16).
- <sup>65</sup>T. Ihle, “Kinetic theory of flocking: derivation of hydrodynamic equations,” *Physical Review E* **83**, 030901 (2011) (cit. on pp. 7, 9).
- <sup>66</sup>E. Bertin, H. Chaté, F. Ginelli, S. Mishra, A. Peshkov, and S. Ramaswamy, “Mesoscopic theory for fluctuating active nematics,” *New Journal of Physics* **15**, 085032 (2013) (cit. on p. 7).
- <sup>67</sup>H. Chaté, F. Ginelli, and R. Montagne, “Simple model for active nematics: quasi-long-range order and giant fluctuations,” *Physical Review Letters* **96**, 180602 (2006) (cit. on pp. 7, 21).
- <sup>68</sup>Y. Fily and M. C. Marchetti, “Athermal phase separation of self-propelled particles with no alignment,” *Phys. Rev. Lett.* **108**, 235702 (2012) (cit. on pp. 7, 9, 12, 13, 38).
- <sup>69</sup>F. D. C. Farrell, M. C. Marchetti, D. Marenduzzo, and J. Tailleur, “Pattern formation in self-propelled particles with density-dependent motility,” *Physical Review Letters* **108**, 248101 (2012) (cit. on p. 7).
- <sup>70</sup>J. Bialké, T. Speck, and H. Löwen, “Crystallization in a dense suspension of self-propelled particles,” *Phys. Rev. Lett.* **108**, 168301 (2012) (cit. on p. 7).
- <sup>71</sup>G. S. Redner, M. F. Hagan, and A. Baskaran, “Structure and dynamics of a phase-separating active colloidal fluid,” *Phys. Rev. Lett.* **110**, 055701 (2013) (cit. on p. 7).

- <sup>72</sup>A. P. Solon, J. Stenhammar, R. Wittkowski, M. Kardar, Y. Kafri, M. E. Cates, and J. Tailleur, “Pressure and phase equilibria in interacting active brownian spheres,” *Phys. Rev. Lett.* **114**, 198301 (2015) (cit. on pp. 7, 11).
- <sup>73</sup>M. E. Cates and J. Tailleur, “When are active brownian particles and run-and-tumble particles equivalent? consequences for motility-induced phase separation,” *EPL (Europhysics Letters)* **101**, 20010 (2013) (cit. on pp. 7, 38).
- <sup>74</sup>A. P. Solon, M. E. Cates, and J. Tailleur, “Active brownian particles and run-and-tumble particles: a comparative study,” *The European Physical Journal Special Topics* **224**, 1231–1262 (2015) (cit. on p. 7).
- <sup>75</sup>H. Chaté, F. Ginelli, G. Grégoire, and F. Raynaud, “Collective motion of self-propelled particles interacting without cohesion,” *Physical Review E* **77**, 046113 (2008) (cit. on pp. 7, 9, 11, 21, 22, 38, 51, 55, 59, 62).
- <sup>76</sup>H. Chaté, F. Ginelli, and G. Grégoire, “Comment on “phase transitions in systems of self-propelled agents and related network models”,” *Physical Review Letters* **99**, 229601 (2007) (cit. on pp. 7, 11, 22, 38, 51).
- <sup>77</sup>D. A. Quint and A. Gopinathan, “Topologically induced swarming phase transition on a 2d percolated lattice,” *Physical Biology* **12**, 046008 (2015) (cit. on pp. 7, 22, 38, 68).
- <sup>78</sup>A. Morin, N. Desreumaux, J.-B. Caussin, and D. Bartolo, “Distortion and destruction of colloidal flocks in disordered environments,” *Nature Physics* **13**, 63 EP – (2016) (cit. on pp. 7, 8, 22, 38, 68).
- <sup>79</sup>O. Chepizhko, E. G. Altmann, and F. Peruani, “Optimal noise maximizes collective motion in heterogeneous media,” *Physical Review Letters* **110**, 238101 (2013) (cit. on pp. 7, 8, 22, 38, 68).
- <sup>80</sup>O. Chepizhko and F. Peruani, “Diffusion, subdiffusion, and trapping of active particles in heterogeneous media,” *Phys. Rev. Lett.* **111**, 160604 (2013) (cit. on pp. 7, 22, 34, 38).
- <sup>81</sup>F. Peruani and I. S. Aranson, “Cold active motion: how time-independent disorder affects the motion of self-propelled agents,” *Phys. Rev. Lett.* **120**, 238101 (2018) (cit. on pp. 7, 22, 38).

- <sup>82</sup>C. Sándor, A. Libál, C. Reichhardt, and C. J. Olson Reichhardt, “Dynamic phases of active matter systems with quenched disorder,” *Physical Review E* **95**, 032606 (2017) (cit. on pp. 7, 22, 38, 68).
- <sup>83</sup>C. Sándor, A. Libál, C. Reichhardt, and C. J. Olson Reichhardt, “Dewetting and spreading transitions for active matter on random pinning substrates,” *The Journal of Chemical Physics* **146**, 204903 (2017), eprint: <https://doi.org/10.1063/1.4983344> (cit. on pp. 7, 22, 38).
- <sup>84</sup>J. Toner, N. Guttenberg, and Y. Tu, “Hydrodynamic theory of flocking in the presence of quenched disorder,” *Phys. Rev. E* **98**, 062604 (2018) (cit. on pp. 7, 8, 22, 38).
- <sup>85</sup>J. Toner, N. Guttenberg, and Y. Tu, “Swarming in the dirt: ordered flocks with quenched disorder,” *Phys. Rev. Lett.* **121**, 248002 (2018) (cit. on pp. 7, 22, 38).
- <sup>86</sup>R. Das, M. Kumar, and S. Mishra, “Polar flock in the presence of random quenched rotators,” *Phys. Rev. E* **98**, 060602 (2018) (cit. on pp. 7, 8, 22, 38).
- <sup>87</sup>P. S. Burada, P. Hanggi, F. Marchesoni, G. Schmid, and P. Talkner, “Diffusion in confined geometries,” *ChemPhysChem* **10**, 45–54, eprint: <https://onlinelibrary.wiley.com/doi/pdf/10.1002/cphc.200800526> (cit. on p. 8).
- <sup>88</sup>S. Dey, K. Ching, and M. Das, “Active and passive transport of cargo in a corrugated channel: a lattice model study,” *The Journal of Chemical Physics* **148**, 134907 (2018), eprint: <https://doi.org/10.1063/1.5022163> (cit. on pp. 8, 39).
- <sup>89</sup>P. Magaretti and H. Stark, “Model microswimmers in channels with varying cross section,” *The Journal of Chemical Physics* **146**, 174901 (2017), eprint: <https://doi.org/10.1063/1.4981886> (cit. on pp. 9, 39, 49, 88).
- <sup>90</sup>B.-q. Ai, Q.-y. Chen, Y.-f. He, F.-g. Li, and W.-r. Zhong, “Rectification and diffusion of self-propelled particles in a two-dimensional corrugated channel,” *Phys. Rev. E* **88**, 062129 (2013) (cit. on pp. 9, 39, 49, 88).
- <sup>91</sup>G. Grégoire and H. Chaté, “Onset of collective and cohesive motion,” *Physical Review Letters* **92**, 025702 (2004) (cit. on pp. 9–11, 21).
- <sup>92</sup>X.-L. Wu and A. Libchaber, “Particle diffusion in a quasi-two-dimensional bacterial bath,” *Phys. Rev. Lett.* **84**, 3017–3020 (2000) (cit. on pp. 9, 39, 44).

- <sup>93</sup>X.-q. Shi and Y.-q. Ma, "Topological structure dynamics revealing collective evolution in active nematics," *Nature Communications* **4**, Article, 3013 EP – (2013) (cit. on p. 9).
- <sup>94</sup>S. Pattanayak, R. Das, M. Kumar, and S. Mishra, "Enhanced dynamics of active brownian particles in periodic obstacle arrays and corrugated channels," *The European Physical Journal E* **42**, 62 (2019) (cit. on p. 9).
- <sup>95</sup>M. Aldana, V. Dosssetti, C. Huepe, V. M. Kenkre, and H. Larralde, "Phase transitions in systems of self-propelled agents and related network models," *Physical Review Letters* **98**, 095702 (2007) (cit. on p. 11).
- <sup>96</sup>S. Pattanayak and S. Mishra, "Collection of polar self-propelled particles with a modified alignment interaction," *Journal of Physics Communications* **2**, 045007 (2018) (cit. on p. 11).
- <sup>97</sup>P. Romanczuk, M. Bär, W. Ebeling, B. Lindner, and L. Schimansky-Geier, "Active brownian particles," *The European Physical Journal Special Topics* **202**, 1–162 (2012) (cit. on pp. 12, 38).
- <sup>98</sup>M. Zeitz, K. Wolff, and H. Stark, "Active brownian particles moving in a random lorentz gas," *The European Physical Journal E* **40**, 23 (2017) (cit. on pp. 13, 39, 44, 46).
- <sup>99</sup>R. Voituriez, J. F. Joanny, and J. Prost, "Generic phase diagram of active polar films," *Phys. Rev. Lett.* **96**, 028102 (2006) (cit. on p. 15).
- <sup>100</sup>S. Mishra, A. Baskaran, and M. C. Marchetti, "Fluctuations and pattern formation in self-propelled particles," *Physical Review E* **81**, 061916 (2010) (cit. on pp. 16, 21, 64).
- <sup>101</sup>E. Bertin, M. Droz, and G. GrÃlgoire, "Hydrodynamic equations for self-propelled particles: microscopic derivation and stability analysis," *Journal of Physics A: Mathematical and Theoretical* **42**, 445001 (2009) (cit. on pp. 16, 64).
- <sup>102</sup>A. Bray, "Theory of phase-ordering kinetics," *Advances in Physics* **43**, 357–459 (1994), eprint: <https://doi.org/10.1080/00018739400101505> (cit. on pp. 17, 20).
- <sup>103</sup>S. Puri, "Kinetics of phase transitions," *Phase Transitions* **77**, 407–431 (2004), eprint: <https://doi.org/10.1080/01411590410001672648> (cit. on p. 17).
- <sup>104</sup>M. Plischke and B. Bergersen, *Equilibrium Statistical Physics (2ND Edition) - Solutions Manual* (World Scientific Press, Dec. 1994) (cit. on p. 17).

- <sup>105</sup>R. J. Glauber, "Time-Dependent Statistics of the Ising Model," *Journal of Mathematical Physics* **4**, 294–307 (1963) (cit. on p. 18).
- <sup>106</sup>K. Kawasaki, "Diffusion constants near the critical point for time-dependent ising models. i," *Physical Review* **145**, 224–230 (1966) (cit. on p. 19).
- <sup>107</sup>I. Lifshitz and V. Slyozov, "The kinetics of precipitation from supersaturated solid solutions," *Journal of Physics and Chemistry of Solids* **19**, 35–50 (1961) (cit. on p. 21).
- <sup>108</sup>S. Dey, D. Das, and R. Rajesh, "Spatial structures and giant number fluctuations in models of active matter," *Physical Review Letters* **108**, 238001 (2012) (cit. on p. 21).
- <sup>109</sup>F. Ginelli, F. Peruani, M. Bär, and H. Chaté, "Large-scale collective properties of self-propelled rods," *Physical Review Letters* **104**, 184502 (2010) (cit. on p. 21).
- <sup>110</sup>S. Mishra and S. Ramaswamy, "Active nematics are intrinsically phase separated," *Physical Review Letters* **97**, 090602 (2006) (cit. on pp. 21, 59).
- <sup>111</sup>Y. Tu, J. Toner, and M. Ulm, "Sound waves and the absence of galilean invariance in flocks," *Physical Review Letters* **80**, 4819–4822 (1998) (cit. on p. 21).
- <sup>112</sup>R. Wittkowski, A. Tiribocchi, J. Stenhammar, R. J. Allen, D. Marenduzzo, and M. E. Cates, "Scalar  $\phi_4$  field theory for active-particle phase separation," *Nature Communications* **5**, Article, 4351 EP – (2014) (cit. on pp. 21, 77, 86, 89).
- <sup>113</sup>R. J. Hawkins, M. Piel, G. Faure-Andre, A. M. Lennon-Dumenil, J. F. Joanny, J. Prost, and R. Voituriez, "Pushing off the walls: a mechanism of cell motility in confinement," *Phys. Rev. Lett.* **102**, 058103 (2009) (cit. on p. 24).
- <sup>114</sup>E. Bodenschatz, W. Pesch, and G. Ahlers, "Recent developments in rayleigh-bäl'nard convection," *Annual Review of Fluid Mechanics* **32**, 709–778 (2000), eprint: <https://doi.org/10.1146/annurev.fluid.32.1.709> (cit. on p. 24).
- <sup>115</sup>A. Zumdieck, R. Voituriez, J. Prost, and J. F. Joanny, "Spontaneous flow of active polar gels in undulated channels," *Faraday Discussions* **139**, 369 (2008) (cit. on p. 24).
- <sup>116</sup>Voituriez, R., Joanny, J. F., and Prost, J., "Spontaneous flow transition in active polar gels," *Europhys. Lett.* **70**, 404–410 (2005) (cit. on p. 24).

- <sup>117</sup>B. W. S. Mishra S. Bhattacharya and E. G. D. Cohen, "Subdiffusion, anomalous diffusion and propagation of a particle moving in random and periodic media," *J Stat Phys* **162** (2016) <https://doi.org/10.1007/s1095> (cit. on p. 35).
- <sup>118</sup>A. Bricard, J.-B. Caussin, D. Das, C. Savoie, V. Chikkadi, K. Shitara, O. Chepizhko, F. Peruni, D. Saintillan, and D. Bartolo, "Emergent vortices in populations of colloidal rollers," *Nature Communications* **6**, Article, 7470 EP – (2015) (cit. on p. 37).
- <sup>119</sup>R. L. Fournier, *Basic transport phenomena in biomedical engineering* (2007) (cit. on p. 37).
- <sup>120</sup>C. Sándor, A. Libál, C. Reichhardt, and C. J. O. Reichhardt, "Collective transport for active matter run-and-tumble disk systems on a traveling-wave substrate," *Phys. Rev. E* **95**, 012607 (2017) (cit. on p. 38).
- <sup>121</sup>C. Reichhardt and C. J. O. Reichhardt, "Clogging and depinning of ballistic active matter systems in disordered media," *Phys. Rev. E* **97**, 052613 (2018) (cit. on p. 38).
- <sup>122</sup>F. I.P.J.T.M.P.R.B.B.E. T. T. Chinnasamy J. L. Kingsley and U. Demirci, "Guidance and self-ãsorting of active swimmers: 3d periodic arrays increase persistence length of human sperm selecting for the fittest," *Adv Sci (Weinh)* **5**, 1700531 (2018) (cit. on pp. 39, 44).
- <sup>123</sup>U. Choudhury, A. V. Straube, P. Fischer, J. G. Gibbs, and F. Hãúfling, "Active colloidal propulsion over a crystalline surface," *New Journal of Physics* **19**, 125010 (2017) (cit. on pp. 39, 44).
- <sup>124</sup>S. Mishra and S. Pattanayak, "Boundary induced convection in a collection of polar self-propelled particles," *Physica A: Statistical Mechanics and its Applications* **477**, 128 –135 (2017) (cit. on p. 39).
- <sup>125</sup>A. E. Patteson, A. Gopinath, P. K. Purohit, and P. E. Arratia, "Particle diffusion in active fluids is non-monotonic in size," *Soft Matter* **12**, 2365–2372 (2016) (cit. on p. 39).
- <sup>126</sup>A. Baskaran and M. C. Marchetti, "Enhanced diffusion and ordering of self-propelled rods," *Phys. Rev. Lett.* **101**, 268101 (2008) (cit. on p. 45).
- <sup>127</sup>B. Bhattacharjee, S. Mishra, and S. S. Manna, "Topological-distance-dependent transition in flocks with binary interactions," *Phys. Rev. E* **92**, 062134 (2015) (cit. on pp. 51, 55).
- <sup>128</sup>F. Ginelli and H. Chaté, "Relevance of metric-free interactions in flocking phenomena," *Phys. Rev. Lett.* **105**, 168103 (2010) (cit. on p. 51).

- <sup>129</sup>A. Peshkov, S. Ngo, E. Bertin, H. Chaté, and F. Ginelli, “Continuous theory of active matter systems with metric-free interactions,” *Phys. Rev. Lett.* **109**, 098101 (2012) (cit. on p. 51).
- <sup>130</sup>A. P. Solon and J. Tailleur, “Revisiting the flocking transition using active spins,” *Phys. Rev. Lett.* **111**, 078101 (2013) (cit. on pp. 59, 66).
- <sup>131</sup>A. P. Solon, J.-B. Caussin, D. Bartolo, H. Chaté, and J. Tailleur, “Pattern formation in flocking models: a hydrodynamic description,” *Phys. Rev. E* **92**, 062111 (2015) (cit. on pp. 59, 66).
- <sup>132</sup>G. Grégoire and H. Chaté, “Onset of collective and cohesive motion,” *Phys. Rev. Lett.* **92**, 025702 (2004) (cit. on p. 59).
- <sup>133</sup>D. Das, D. Das, and A. Prasad, “Giant number fluctuations in microbial ecologies,” *Journal of Theoretical Biology* **308**, 96–104 (2012) (cit. on p. 59).
- <sup>134</sup>M. Romensky, V. Lobaskin, and T. Ihle, “Tricritical points in a vicsek model of self-propelled particles with bounded confidence,” *Phys. Rev. E* **90**, 063315 (2014) (cit. on pp. 67, 88).
- <sup>135</sup>D Yllanes, M Leoni, and M. C. Marchetti, “How many dissenters does it take to disorder a flock?” *New Journal of Physics* **19**, 103026 (2017) (cit. on p. 68).
- <sup>136</sup>Maciej Lisicki et al. “Swimming eukaryotic microorganisms exhibit a universal speed distribution,” ArXiv e-prints (2019), [arXiv:arXiv:1907.00906v1 \[cond-mat.soft\]](https://arxiv.org/abs/1907.00906v1) (cit. on pp. 76, 89).
- <sup>137</sup>J. W. Cahn and J. E. Hilliard, “Free energy of a nonuniform system. i. interfacial free energy,” *The Journal of Chemical Physics* **28**, 258–267 (1958), eprint: <https://doi.org/10.1063/1.1744102> (cit. on p. 77).